SPR and AFM Experiments on Biological Monolayers

Charles E. H. Berger

SPR AND AFM EXPERIMENTS

ON BIOLOGICAL MONOLAYERS

The work described in this thesis was mainly supported by the Dutch organization: "Fundamenteel Onderzoek der Materie (FOM)"

ISBN 90-3650864-9

SPR AND AFM EXPERIMENTS

ON BIOLOGICAL MONOLAYERS

PROEFSCHRIFT

ter verkrijging van
de graad van doctor aan de Universiteit Twente,
op gezag van de rector magnificus,
Prof. dr. Th.J.A. Popma,
volgens besluit van het openbaar College voor Promoties
in het openbaar te verdedigen
op vrijdag 25 oktober 1996 te 15:00 uur.

door

Charles Emile Hubert Berger
geboren op 7 maart 1968
te Utrecht

Dit proefschrift is goedgekeurd door

de promotor:	Prof. dr. J. Greve
de assistent-promotor:	Dr. R.P.H. Kooyman

CONTENTS

INTRODUCTION

The aim of the research project described in this thesis was the study of surface plasmon microscopy (SPM) and the application of this method to biological monolayers. The emphasis was more on the development of methods than on the study of the samples themselves.

Two types of biological monolayers have been studied. The first one is a protein monolayer, and more specifically; layers of antibodies and antigens. Improving the knowledge about detection of the immune reactions that can take place between these compounds is important for the development of diagnostic assays, biomaterials, and protein purification methods. We will study this interaction using surface plasmon resonance (SPR) sensor methods.

The second type is a lipid monolayer, which has been used as a model system for a biological cell membrane. Lipid monolayers can be spread and studied at the air-water interface, but can also be transferred to a solid substrate. This is necessary for the two techniques that were applied to lipid monolayers in this work. Surface plasmon microscopy was applied to a phase-separated lipid monolayer that was deposited on a substrate using the Langmuir-Blodgett (LB) technique. The different phases could be microscopically observed since they coexist in separate domains and have different optical properties. To study these layers at a lateral scale smaller than possible with optical methods, a new atomic force microscopy (AFM) method was used. With this microscope the adhesive properties of the layer, which depend on the lipid phase, are used for imaging.

This thesis will start with a short overview of methods for the characterization of surface layers. After an introduction into Fresnel theory, we will discuss ellipsometry, Brewster angle microscopy (BAM) and surface plasmon resonance (SPR) methods. The Fresnel equations satisfactorily describe these methods at lateral scales much larger than the wavelength of the used light. This theory can therefore be used to determine system parameters by fitting the measurements.

In the second chapter we will see how SPR was used to develop an accurate, differential immunosensor, with a number of advantages over present SPR immunosensors. It will also be demonstrated that SPR is well suited for use in multichannel immunosensors. The first multi-

channel measurements will be presented with one as well as two-dimensional arrays of sensor surfaces.

Going towards higher lateral resolution, plasmon propagation effects will make the Fresnel theory invalid at the microscopic scale. We have developed a phenomenological model to describe the reflectance near index steps at the microscopic scale. All experimental parameters used for the calculations have been derived from the layer system under investigation (not from fitting). A systematical comparison of theoretical and experimental values was made for 11 wavelengths in the visible region and will be presented in the third chapter.

In the fourth chapter a surface plasmon microscopy (SPM) setup will be described. We will show that there is a trade-off relationship between thickness resolution (or contrast) and lateral resolution with respect to the choice of wavelength. We have chosen for a short wavelength and tackled the problem of an extremely low contrast by developing some image acquisition methods. In this way the maximum diffraction limited lateral resolution can be obtained.

A short introduction to Langmuir-Blodgett (LB) monolayers will be given in the fifth chapter. After that we will describe the application of the SPM to the imaging of these monolayers, using the techniques described in the previous chapter.

The sixth chapter will cover another new technique that was applied for the characterization of lipid LB monolayers: adhesion mode atomic force microscopy. It will be demonstrated that the orientation of molecules in the monolayer strongly influences the adhesion of the tip to the surface. This allows these monolayers to be imaged with super-resolution (20 nm) and high contrast. We will argue that this technique holds a promise for functional group identification.

The thesis will end with a general discussion of the results obtained in this work, and an appendix where a new surface plasmon microscope that was developed (just before completion of this project) is described.

The model presented in the third chapter, and the methods and results in the fourth and fifth chapter have been published in the *Review of Scientific Instruments* **1994**, *65*, 2829. The sixth chapter was published in *Langmuir*, **1995**, *11*, 4188. The results presented in the third chapter have been submitted to *Optics Communications*. The first part of the second chapter (the differential SPR sensor) has been submitted to *Sensors and Actuators B*; the second part (the multichannel SPR sensor) has been submitted to *Biosensors & Bioelectronics*.

CHAPTER ONE

INTRODUCTION TO SURFACE SPECIFIC METHODS

In this chapter we will very briefly go through the spectrum of techniques that are available for interface characterization. Then the Fresnel theory is given, describing reflectometrical interface characterization techniques like ellipsometry, Brewster angle reflectometry and surface plasmon resonance.

1.1 General introduction to surface characterization methods

There is a wealth of experimental techniques available for the investigation of surfaces or interfaces, adsorbates and thin layers.[1,2] They can be classified in structural imaging and spectroscopy methods, although some techniques combine these possibilities. A common feature is their surface sensitivity, which is very important since for any bulk object the number of bulk atoms exceeds the number of surface atoms by many orders of magnitude. However, they widely differ in surface sensitivity, lateral resolution, destructiveness, experimental conditions (e.g. UHV), and the kind of interface they can be used for.

1.1.1 Spectroscopy techniques

Most spectroscopy techniques[3,4] can be classified by the kind of excitation and the emitted particles. Excitation may take place through photons, electrons, ions, neutral particles, heat, and electric fields.[5,6] We will just briefly mention a number of these techniques.

X-ray photoelectron spectroscopy (XPS)[7] is based on the photoelectric effect and the dependence of the emitted photoelectrons on their binding energy. It gives information describing the chemical composition of a solid surface under high-vacuum conditions.

Similar information is obtained in Auger electron spectroscopy (AES)[8,9] where an electron beam is used for the excitation. The excited electrons have an energy characteristic of a certain core-level transition and are analyzed. As in XPS, the surface sensitivity of AES is determined by the escape depth of the electrons and typical probing depths are in the range of 1 to 3 nm.

In secondary ion mass spectroscopy (SIMS)[10,11] a surface under vacuum is bombarded with accelerated ions. Fragments of surface molecules are emitted and analyzed by measuring the intensity as a function of the mass-to-charge ratio. The chemical composition of the surface can be determined with a probing depth of about 1 nm.

Electron energy loss spectroscopy (EELS)[12] uses an electron beam incident on the sample at a certain angle. When the energy of the reflected electrons is analyzed at an angle slightly off specular reflection peaks of lower energy are measured due to inelastic scattering (the electrons can lose energy to the vibrational modes of molecules). The sensitivity is about 10^{-3} of a monolayer, which is very high.

Optical vibrational spectroscopy techniques include Raman spectroscopy and infrared spectroscopy. No vacuum is needed for these techniques rendering them useful for biological applications, but the

surface sensitivity is lower, especially for Raman scattering. Fourier transform infrared spectroscopy (FTIR)[13,14] can be used to characterize the surface chemical structure by using an attenuated total reflection (ATR) crystal or by using a metallic substrate. ATR can also improve the Raman signal as can surface enhanced Raman scattering (SERS)[4] which uses a roughened metal surface to enhance scattering efficiency of adsorbates. Waveguide Raman scattering is another way to increase surface sensitivity taking advantage of the relatively large part of the light that propagates through a layer on top of the waveguide.

1.1.2 Microscopy techniques

In the 1930's the transmission electron microscope (TEM)[15] was developed, surpassing the resolution of light microscopes by using electrons instead of photons, and suitably shaped magnetic fields as lenses. Drawbacks of this technique are that the sample needs to be thin enough to allow the transmission of sufficient electrons, and that selective heavy metal staining is needed to obtain a good contrast. In the scanning electron microscope (SEM)[1,15,16] the electrons reflected from the surface rather than those transmitted are producing an image of the surface topography. This technique together with countless staining and replicating techniques allows many more types of samples to be studied.

The field of scanning probe microscopy started with the invention of the scanning tunneling microscope (STM)[17] in 1982, where a conductive tip is scanned over a (semi)conductive sample while measuring the tunneling electrons between tip and sample. In this way atomic resolution imaging can be achieved while varying the bias voltage can give information about the electronic structure with the same resolution. Soon the atomic force microscope (AFM)[18,19] emerged, where the deflection of a cantilever on which a tip is mounted is caused by the force interaction between tip and sample. The deflection is measured while the tip is scanned over the sample in contact. While this technique can reach a similar resolution as STM it can be applied to many more types of samples, especially in the field of biology.

Scanning near field optical microscopy (SNOM)[20] is a scanning probe method that takes the lateral resolution of optical microscopy past the diffraction limit. A small (sub-wavelength sized) aperture is scanned over a transparent sample with an objective on the opposite side of the sample. Optical excitation is achieved via a light beam through the objective whereas the light is detected using the aperture; of course the roles of the objective and the aperture can be interchanged.

The surface sensitivity of normal light microscopy can be enhanced in several ways. When a monomolecular layer is studied, fluorescent labels that have a different solubility for different parts of the monolayer can be added to it. By exciting fluorescence the different parts of the layer can be imaged with this light, even at an air-water interface.[21,22] Another way is to make light reflect off the interface under investigation and, using that light, create an image with the microscope. The conditions for the reflection should be chosen such that the properties of the interface are represented in the intensity or polarization state of the reflected light. Reflectometrical methods will be discussed in the next sections after an introduction to the Fresnel theory.

1.1.3 Diffraction techniques

For the determination of lattice constants of crystals a number of diffraction techniques are available. X-rays, electrons, atoms, molecules, ions, neutrons, *etc.* can be used as probes, but because of the needed surface sensitivity only particles that do not penetrate too deep into the substrate can be used. The ideal probes for the interface are molecules, atoms, ions and low energy electrons. Electron diffraction can be used on solid surfaces only, and care must be taken that the electron dose does not disrupt the crystal lattice in the case of monolayers.[23,24] X-ray diffraction can be applied even on monolayers at air-water interfaces, but requires a special experimental arrangement, and high intensity synchotron X-ray sources.[25,26] Neutron reflectivity has been used for determination of the molecular order in films at the air-water interface as well.[27] Thermodynamic measurements such as the lateral pressure as a function of molecular area, and surface potential measurements which determine the average dipole moment of the molecules in the layer are other techniques for the characterization of monolayers at an air-water interface.[28]

The list of techniques in section 1.1 is far from complete, as there are innumerable surface analysis methods and variants of these methods. It is meant only to provide a background for the next sections. Optical immunosensors will be discussed in the next chapter.

1.2 Fresnel theory

Fresnel's theory[29] can be derived from the Maxwell equations and describes the reflection and transmission of a plane monochromatic light wave incident upon a layer system. To apply Fresnel's formulae the layer

system should consist of infinite, perfectly flat layers. In practice, this condition is fulfilled for studies at a lateral scale exceeding the wavelength by an order of magnitude. In that situation, Fresnel theory should describe reflectometrical measurements within the experimental accuracy. Therefore, this theory can be used to determine the parameters of the layer structure under investigation by analytical inversion, or by varying the parameters to fit the model to the measurements. We can also use it to investigate the sensitivity and accuracy of reflectometrical methods. For this thesis our main interest lies in reflectometrical methods that are suitable for measurements on biological monolayers.

1.2.1 Reflection at an interface

When a monochromatic plane wave impinges on an infinite interface between media 1 and 2, in general reflection and transmission will occur. These fields (indices respectively *i*, *r* and *t*) are described by

$$\vec{E}_i = \vec{E}_{ip} e^{i(\vec{\kappa}_i \cdot \vec{r} - \omega t)} \qquad \vec{E}_r = \vec{E}_{rp} e^{i(\vec{\kappa}_r \cdot \vec{r} - \omega t)} \qquad \vec{E}_t = \vec{E}_{tp} e^{i(\vec{\kappa}_t \cdot \vec{r} - \omega t)}, \qquad (1.1)$$

where *p* indicates the polarization of the wave. The light is decomposed into a *p* polarized component parallel to the plane of incidence (Fig. 1.1),

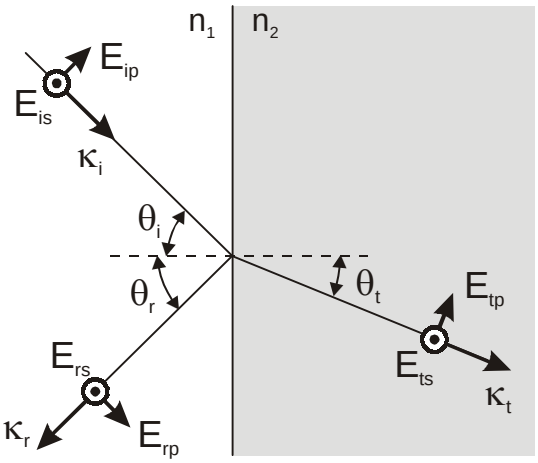

Fig. 1.1 Reflection and transmission of a plane wave incident on an interface between medium 1 and 2.

and an *s* polarized component (‘*senkrecht*’) perpendicular to this plane. The reflection and transmission formulae for an *s* polarized wave are identical to Eq. 1.1, with every *p* substituted by an *s*.

The length of the wave vectors is defined by

$$\kappa_i = \kappa_r = n_1 \frac{\omega}{c} \text{ and } \kappa_t = n_2 \frac{\omega}{c} \qquad (1.2)$$

where n_1 and n_2 are the refractive indices of the respective media. The angles the reflected and transmitted waves are making with the surface normal are given by

$$\theta_i = \theta_r \tag{1.3}$$

and by Snell's law:

$$n_1 \sin\theta_i = n_2 \sin\theta_t . \tag{1.4}$$

The Fresnel reflection coefficient for *p* polarized light is[29]

$$\frac{E_{rp}}{E_{ip}} = r_{12p} = \frac{n_2 \cos\theta_i - n_1 \cos\theta_t}{n_2 \cos\theta_i + n_1 \cos\theta_t}, \tag{1.5}$$

and for *s* polarized light

$$\frac{E_{rs}}{E_{is}} = r_{12s} = \frac{n_1 \cos\theta_i - n_2 \cos\theta_t}{n_1 \cos\theta_i + n_2 \cos\theta_t}. \tag{1.6}$$

Using Snell's law, these formulae can be written as

$$r_{12p} = \frac{\tan(\theta_i - \theta_t)}{\tan(\theta_i + \theta_t)} \tag{1.7}$$

and

$$r_{12s} = -\frac{\sin(\theta_i - \theta_t)}{\sin(\theta_i + \theta_t)} \tag{1.8}$$

The reflected intensity or reflectance for *p* and *s* polarized light is given by

$$R_p = \left| r_{12p} \right|^2 \text{ and } R_s = \left| r_{12s} \right|^2 . \tag{1.9}$$

1.2.2 Reflection at a layer

Suppose medium 2 is a layer in between medium 1 and medium 3. Regardless of the polarization, the reflection coefficient for the layer can be expressed in the reflection coefficients of the interfaces (see Fig 1.2), with the *z*-axis perpendicular to the interface:

$$\begin{aligned} r_{123} &= r_{12} + t_{12} r_{23} t_{21} e^{2i\kappa_{z_2} d_2} + t_{12} r_{23} r_{21} r_{23} t_{21} e^{4i\kappa_{z_2} d_2} + \cdots = \\ &= r_{12} + t_{12} r_{23} t_{21} e^{2i\kappa_{z_2} d_2} \left[\sum_{j=0}^{\infty} \left(r_{21} r_{23} e^{2i\kappa_{z_2} d_2} \right)^j \right] \end{aligned} \tag{1.10}$$

where

$$\kappa_{z_i} = \sqrt{\kappa_i^2 - \kappa_{x_1}^2} = \frac{\omega}{c}\sqrt{\varepsilon_i - \varepsilon_1 \sin^2\theta_1}\,, \tag{1.11}$$

with i the number of the medium, d_i the layer thickness, and $\varepsilon_i = n_i^2$.
Since for $0 < q < 1$

$$\sum_{j=0}^{\infty} q^j = \frac{1}{1-q}, \tag{1.12}$$

we find

$$r_{123} = r_{12} + \frac{t_{12}t_{21}r_{23}e^{2i\kappa_{z_2}d_2}}{1 - r_{21}r_{23}e^{2i\kappa_{z_2}d_2}} = \frac{r_{12} + r_{23}(t_{12}t_{21} - r_{12}r_{21})e^{2i\kappa_{z_2}d_2}}{1 - r_{21}r_{23}e^{2i\kappa_{z_2}d_2}}. \tag{1.13}$$

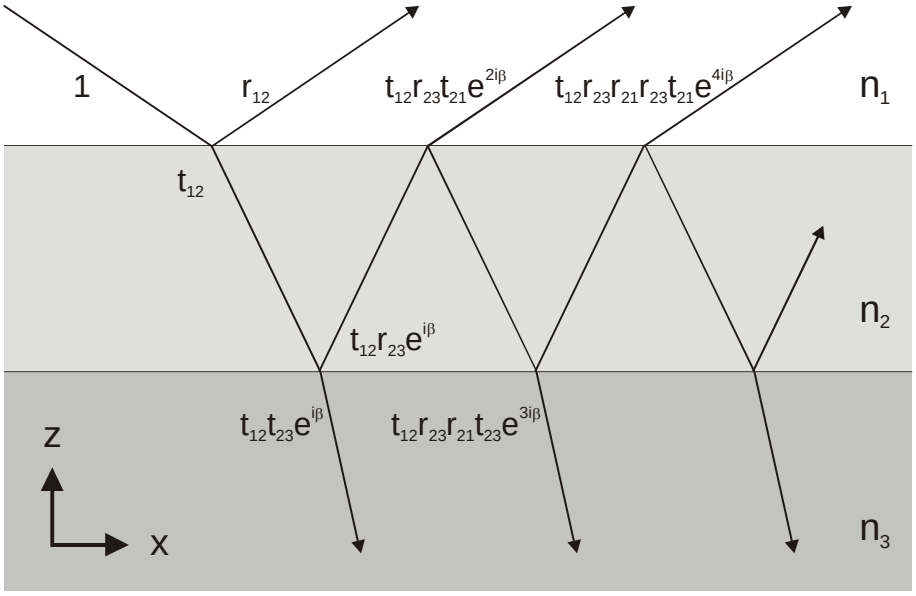

Fig. 1.2 Multiple reflection and transmission in a layer, with unit incident amplitude. The amplitudes are specified by the Fresnel coefficients of the interfaces and a phase retardation $\beta = \kappa_{z2}d_2$.

In the left of Fig. 1.3 we see the normal propagation of the light for reflection and refraction. On the basis of Fermat's principle the reversed propagation direction should also be physically possible (see middle). In this reversed situation we can imagine some extra transmitted and reflected beams (see right). By comparing the situation on the right to the situation on the left we find

$$t_{12}t_{21} + r_{12}r_{12} = 1 \tag{1.14a}$$

$$t_{12}r_{21} + r_{12}t_{12} = 0 \quad \Rightarrow \quad r_{21} = -r_{12}\,, \tag{1.14b}$$

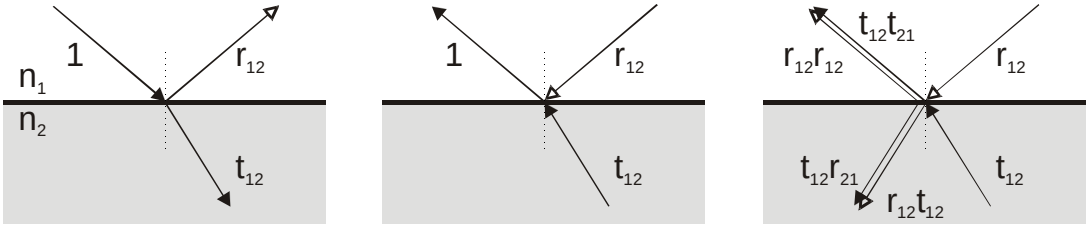

Fig. 1.3 Graphical illustration of the Stokes relations.

which are known as the Stokes relations. Substituting in Eq. (1.13) we obtain

$$r_{123} = \frac{r_{12} + r_{23} e^{2i\kappa_{z_2} d_2}}{1 + r_{12} r_{23} e^{2i\kappa_{z_2} d_2}}, \tag{1.15}$$

where the reflection coefficient of a layer is expressed in the reflection coefficients of the interfaces.

1.2.3 Reflection at multiple layers

The extension of the above formulae to a multiple layer system is straightforward. In the following, n is the number of layers. m=0 for the medium from which the light is incident, and m=n+1 for the semi-infinite medium at the other side of the layer structure.

Going through the layers one by one and writing R_m for the total reflection coefficient of all interfaces after medium m, we start with

$$R_n = r_{n,n+1}. \tag{1.16}$$

For m=n to 1:

$$R_{m-1} = \frac{r_{m-1,m} + R_m e^{2i\kappa_{z_m} d_m}}{1 + r_{m-1,m} R_m e^{2i\kappa_{z_m} d_m}} \tag{1.17}$$

a recurrent relation eventually yielding the total reflection coefficient R_0.

1.3 Reflectometric methods

In this section we will discuss ellipsometry, Brewster angle microscopy and surface plasmon resonance. These reflectometrical methods have a number of features in common. First, an angle of incidence, a polarization state and a wavelength can be chosen for the incident light beam. Second, there is a layer structure under study for which a suitable substrate and ambient medium can be chosen,

depending on the method used. Third, the intensity of the reflected light may be measured as a function of incident angle, polarization or wavelength.

These measurements can be related to the optical properties of the layer structure under investigation by the model described in the preceding section. A number of simplifying assumptions will be made: *(i)* the incident light can be approximated by a monochromatic plane wave; *(ii)* the incidence medium is transparent and optically isotropic; *(iii)* the sample surface is a plane boundary; *(iv)* the optical properties of the sample are laterally uniform over distances of the order of the wavelength; *(v)* the light-sample interaction is elastic, no frequency change occurs. Any changes in the optical properties of the sample in the direction of the surface normal can be accounted for by addition of more layers with the appropriate properties in the stratified-medium model (SMM). The dielectric functions of mixed phases can be calculated using effective medium theories (EMTs) on the basis of component volume fractions and microstructure.

1.3.1 Ellipsometry

In ellipsometry[30] the change in the state of the polarization of light upon reflection at interfaces and thin films is used to characterize these films. This characterization can be real-time and in-situ and is nonperturbing. The beam that is incident on the layer system is usually monochromatic, collimated and polarized. The ratio ρ of the complex reflection coefficients for *p* and *s* polarization is determined from the change in the polarization state:

$$\rho = \frac{r_p}{r_s}. \tag{1.18}$$

When r_p and r_s are written as

$$r_p = \left|r_p\right| e^{i\delta_p} \quad \text{and} \quad r_s = \left|r_s\right| e^{i\delta_s} \tag{1.19}$$

then

$$\rho = \tan\psi \; e^{i\Delta}, \tag{1.20}$$

with

$$\Delta = \delta_p - \delta_s \quad \text{and} \quad \tan\psi = \frac{\left|r_p\right|}{\left|r_s\right|}. \tag{1.21}$$

In ellipsometric measurements Δ and ψ are measured, ellipsometry therefore has the advantage of measuring only relative amplitudes and phases. For completely transparent layers, ρ becomes a periodic function of the layer thickness *d*. By performing measurements at more than one angle of incidence θ or wavelength λ the uncertainty of an integral multiple of the film thickness period can be resolved. The layer thickness *d* should of course be independent of λ or θ. In multiple-angle-of-incidence ellipsometry (MAIE) ρ is measured as a function of θ, while in spectroscopic ellipsometry (SE) it is measured as a function of λ. In variable-angle spectroscopic ellipsometry (VASE) ρ is determined varying both θ and λ.

Other, but less generally applicable ways to obtain more ellipsometric measurements to separate layer parameters include: *(i)* measuring several unknown thicknesses with the same dielectric constant; *(ii)* measuring the same film with different surrounding media; *(iii)* measuring the same film on different substrates; *(iv)* measuring in transmission as well as in reflection.[31] Clearly it is also possible to measure the thickness with another method such as AFM.[32]

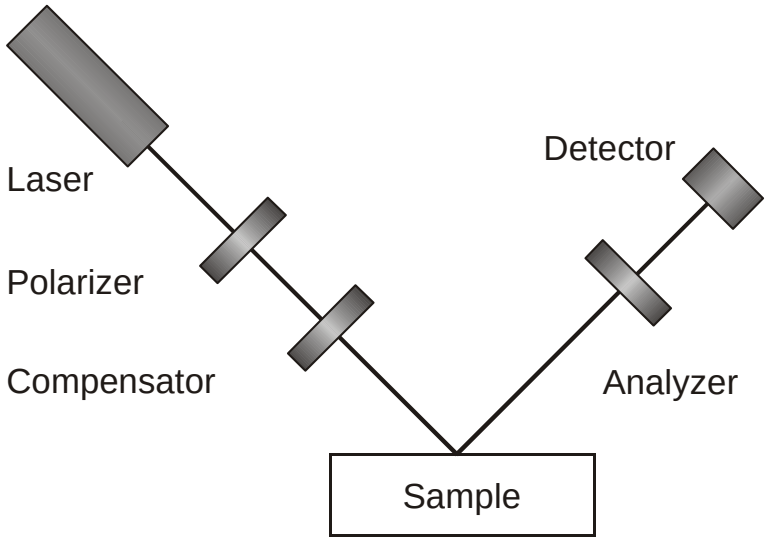

Fig. 1.4 Polarizer-compensator-sample-analyzer (PCSA) ellipsometer arrangement.

The inverse problem of determining the optical properties from the measurements can be solved by searching those model parameters that best match theoretical and experimental values of the ellipsometric function. Except for the simple cases that can be solved analytically with just one or two interfaces, this usually requires using linear regression analysis, to minimize an error function

$$f = \sum_{i=1}^{N} \left[\left(\psi_{im} - \psi_{ic} \right)^2 + \left(\Delta_{im} - \Delta_{ic} \right)^2 \right] \tag{1.22}$$

where ψ_{im}, ψ_{ic} and Δ_{im}, Δ_{ic} denote the i^{th} measured and calculated values of the N independent ellipsometric measurements.

Ellipsometry can be performed with many different experimental configurations. The most common polarizer-compensator-sample-analyzer (PCSA) ellipsometer arrangement is shown in Figure 1.4. A monochromatic collimated beam (unpolarized, or circularly polarized) is linearly polarized by polarizer P, after which the compensator C (a quarter-wave retarder) generally renders the polarization elliptic. By adjusting the polarizer angle P such that the light is linearly polarized after reflection, the output of the photo detector can be reduced to zero by adjusting the analyzer angle A.

The compensator angle C is usually chosen equal to $\pm\pi/4$ with respect to the plane of incidence. Two independent nulls can be reached for each compensator setting, therefore these nulls define four zones. Δ and ψ can now be determined directly from P and A; *e.g.* when C=-π/4 then:

$$\Delta = 2P + \pi/2 \quad \text{and} \quad \psi = A. \tag{1.23}$$

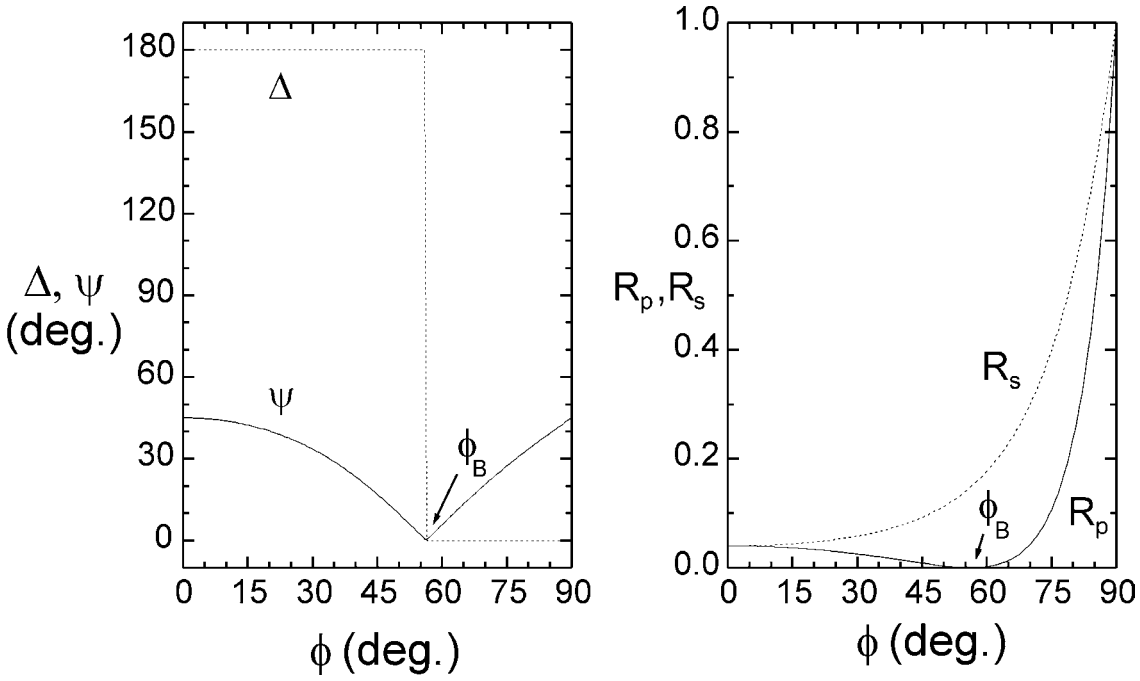

Fig. 1.5 The ellipsometric parameters Δ and ψ and the reflectances R_p and R_s for *p* and *s* polarized light as a function of the incident angle ϕ. The values were calculated for an air-glass interface (n_{glass}=1.5) at wavelength λ=546 nm.

In Fig. 1.5, Δ and ψ are plotted as a function of the angle of incidence. Note that not the intensities but the angles for which the intensity vanishes determine the ellipsometric parameters, which adds to the precision of the method. In an ideal ellipsometer measuring one null is sufficient to determine ρ, but by measuring multiple nulls the experimental error can be decreased by averaging.

The null ellipsometer can be automated by rotating the polarizer and analyzer with stepping motors, using feedback control. To increase the speed and avoid the use of rotating parts Faraday cells can be inserted after the polarizer and before the analyzer to produce magneto-optical rotations. In the rotating analyzer ellipsometer (RAE) the polarization state of the reflected light is analyzed by rotating the analyzer and performing a Fourier analysis of the output signal. For fast measurements without moving parts a photo-elastic modulator (PEM) can be used in place of the compensator.

Various experimental schemes have been applied to allow for fast (millisecond time scale) spectroscopic ellipsometry on semiconductor materials mainly. Layer thicknesses and dielectric functions were measured real time and *in situ* during layer growth or etching.[33-36] Ellipsometry has also been applied succesfully to surfactant mono-molecular layers at the water-air interface.[37-39]

1.3.2 Brewster angle microscopy

A form of reflectometry which was derived from ellipsometry is Brewster angle microscopy (BAM)[40-46] which is mostly applied to monolayers at an air-water interface. Consider a *p* polarized beam which is incident from medium 1 on a plane interface with medium 2 (*i.e.* the five requirements mentioned at the start of section 1.3 are met). At Brewster's angle, the reflectance vanishes if both n_1 and n_2 are real (as can be seen in Figure 1.5). Brewster's angle θ_B is defined as:

$$\theta_B + \theta_t = \frac{\pi}{2}, \tag{1.24}$$

for which r_{12p} becomes zero (see Eq. 1.7). Using Snell's law again we find

$$n_1 \sin\theta_B = n_2 \sin\left(\pi/2 - \theta_B\right) = n_2 \cos\theta_B, \tag{1.25}$$

and thus

$$\tan\theta_B = \frac{n_2}{n_1}. \tag{1.26}$$

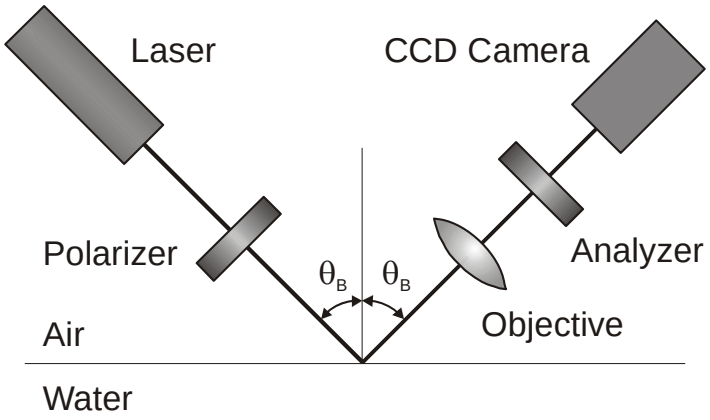

Fig. 1.6 Schematic diagram of a Brewster angle microscope (BAM).

For a real interface however, the reflectance does not vanish, but has a minimum at Brewster's angle. In the case of a monolayer at the air-water interface the depth of this minimum is determined by: *(i)* The presence of the monolayer at the interface, which has a refractive index different from n_1 and n_2. *(ii)* The roughness of the water surface caused by thermal fluctuations (about 0.3 nm).[42] *(iii)* The optical anisotropy of ordered monolayers stemming from the anisotropic polarizability of hydrocarbon chains of monolayer molecules. Therefore, monolayer parts with the same molecular tilt angle (with respect to the surface normal) but different molecular azimuthal angles (direction in the surface plane), give rise to different reflectivities.

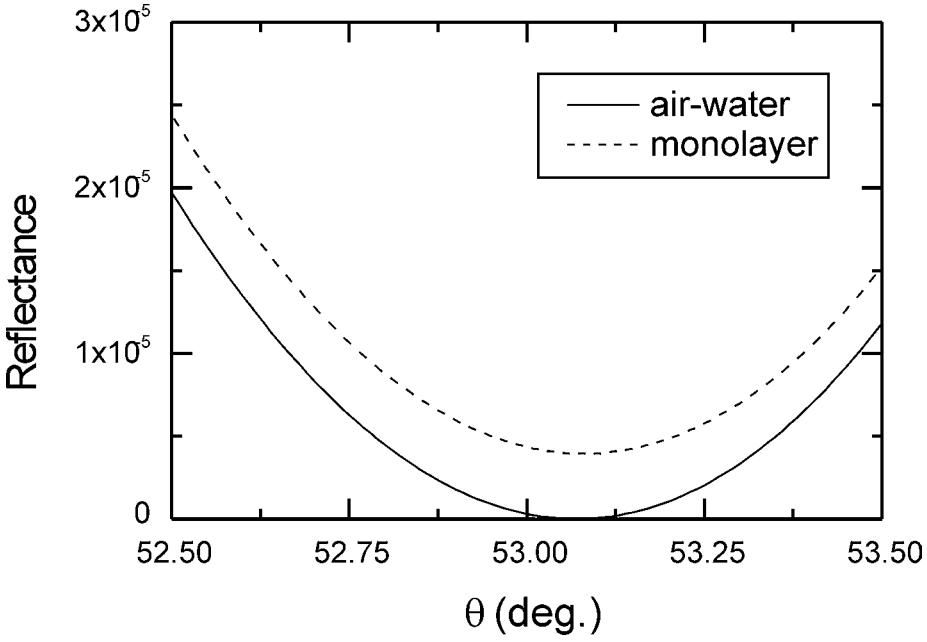

Fig. 1.7 Reflectance around Brewster's angle for an air-water interface (n_{water}=1.33; λ=633 nm) with and without a monolayer (d=2.5 nm; n=1.5). Note the reflectance scale.

By simply imaging the reflected *p* polarized light with an objective on a camera (see Fig. 1.6), monolayers at the air-water interface can be observed *in situ* in real time. The lateral resolution of this method is in the micrometer range (diffraction limited), while the thickness sensitivity is about 0.2 nm.[40] Because of the small difference in the reflection coefficient (see Fig. 1.7) for the interface with or without the monolayer, a high polarization ratio and considerable laser power are needed to obtain a sufficient intensity and contrast (typically 100 mW).

BAM can be used to directly observe the anisotropy in monolayers, if areas with different reflectance (having the same molecular tilt angle but with different orientations in the monolayer plane) exceed the resolution of the BAM. It also allows for a quantitative study of the molecular tilt,[41] for example as a function of the mean molecular area. When an analyzer is introduced in front of the camera, due to the anisotropy the contrast can be adjusted because the reflected light is only *p* polarized if chains are tilted parallel or anti-parallel to the plane of incidence. Therefore, the azimuthal chain orientation can be deduced from the reflectance at different analyzer positions.

1.3.3 Surface plasmon resonance

In the case of internal reflection in a prism (n_p) at the interface with a sample medium (n_s), with $n_p > n_s$, then $\theta_t > \theta_i$ because of Snell's law:

$$\sin\theta_i = \frac{n_s}{n_p}\sin\theta_t . \tag{1.27}$$

Thus, as θ_i increases the transmitted ray gradually approaches grazing incidence, and an increasing amount of energy is reflected. The angle of incidence for which $\theta_t = \pi/2$ is known as the critical angle θ_c, and

$$\sin\theta_c = \frac{n_s}{n_p} . \tag{1.28}$$

For angles of incidence greater than or equal to θ_c all of the incident energy is reflected from the interface, a process which is known as total internal reflection (TIR). The reflectance as a function of the internal angle of incidence is plotted in Fig. 1.8*(a)*, where the internal and external angles of incidence are defined as well.

The transmitted electric field can be written as

$$\vec{E}_t = \vec{E}_{0t} e^{i(\vec{\kappa}_t \cdot \vec{r} - \omega t)}, \tag{1.29}$$

where

$$\kappa_{tx} = \kappa_t \sin\theta_t \quad \text{and} \quad \kappa_{tz} = \kappa_t \cos\theta_t \tag{1.30}$$

and there is no *y*-component of $\vec{\kappa}$, as the plane of incidence is in the *x*-*z* plane and the interface is in the *x*-*y* plane. Using Snell's law again we find

$$\kappa_t \cos\theta_t = \pm\kappa_t \left(1 - \frac{n_p^2}{n_s^2}\sin^2\theta_i\right)^{\frac{1}{2}} \tag{1.31}$$

and since in the case of TIR $\sin\theta_i > n_s/n_p$,

$$\kappa_{tz} = \pm i\kappa_t \left(\frac{n_p^2}{n_s^2}\sin^2\theta_i - 1\right)^{\frac{1}{2}} \equiv \pm i\beta \ . \tag{1.32}$$

Therefore,

$$\vec{E}_t = \vec{E}_{0t} e^{\mp\beta z} e^{i(\kappa_{tx}x - \omega t)} . \tag{1.33}$$

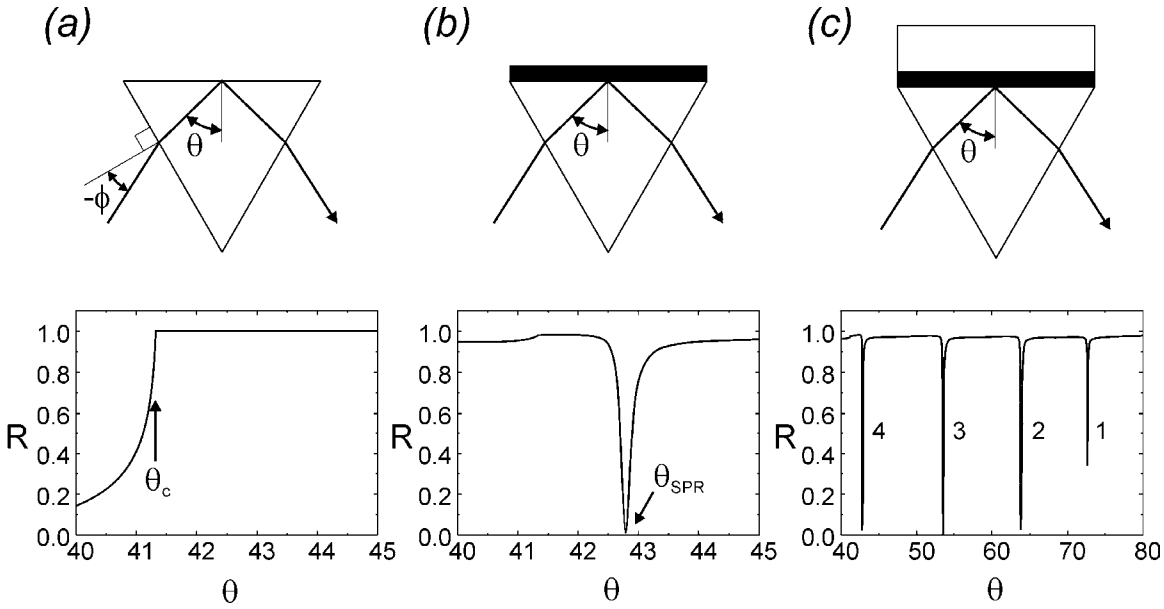

Fig. 1.8 Several configurations which can be used for evanescent wave optics, with the corresponding reflectances as a function of the internal incident angle θ (λ=633 nm). ***(a)*** Total internal reflection at a glass prism base (ε_{glass}=2.3), and definitions of the internal and external angles of incidence θ and ϕ, respectively. ***(b)*** SP excitation in the Kretschmann geometry with a 53 nm silver layer (ε_{silver}=-18.35+*i*0.55), seen as a dip in the reflectance. ***(c)*** Excitation of guided modes after addition of a 1.2 μm polymetylmethacrylate (PMMA) layer (ε_{PMMA}=2.18).

Because the positive exponential is physically untenable, we have a wave with an amplitude that decreases exponentially as it penetrates the less dense medium. The penetration depth d_p as defined by the 1/*e* decrease in amplitude is

$$d_p = \frac{\lambda}{2\pi}\left(\frac{n_p^2}{n_s^2}\sin^2\theta_i - 1\right)^{-\frac{1}{2}}. \qquad (1.34)$$

The field propagates along the interface in the *x*-direction as a so-called *surface* or *evanescent wave*. Because of the presence of the evanescent field at the interface, the reflected light is sensitive to optical changes within a distance of the order of the wavelength from the interface.[47]

By enhancement of the evanescent field, the system becomes even more sensitive to the optical parameters near the interface. This enhancement (by more than a factor of 10) can be obtained by surface plasmon (SP)[48-50] excitation. In the so-called Kretschmann configuration[51] a thin metal layer is introduced on top of the prism base, with light internally reflecting (see Fig. 1.8 *(b)*). Free electrons in the metal can

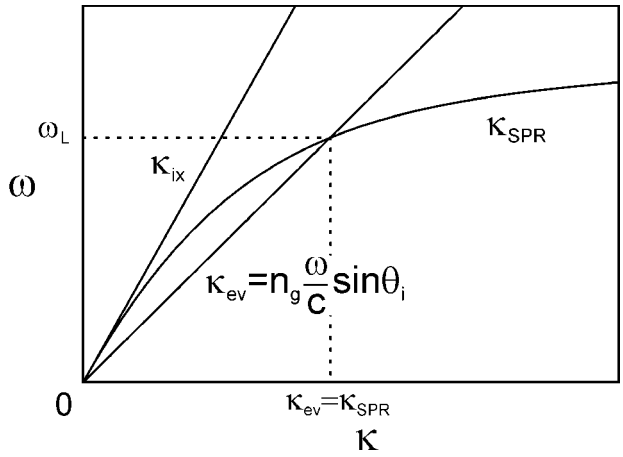

Fig. 1.9 Dispersion of: incident light in the sample medium κ_{ix}; the evanescent wave κ_{ev} (or light internally incident); and the surface plasmon κ_{SPR}.

be made to oscillate harmonically and coherently when excited by the evanescent wave along the interface if the incident light is *p* polarized, that is, if its *E* field has a component perpendicular to the interface. For a certain angle of incidence θ_{SPR}, the component parallel to the interface of the wave vector of the incident light matches that of the electron oscillations or surface plasmons:

$$n_p \frac{\omega}{c}\sin\theta_{SPR} = \kappa_{ev} = \kappa_{SPR}, \qquad (1.35)$$

with n_p as the refractive index of the prism. In this case surface plasmon resonance (SPR) occurs. The wave vector κ_{SPR} on the interface between the metal layer (ε_m), and the sample medium (ε_s) is approximated by[52]

$$\kappa_{SPR} = \frac{\omega}{c}\left(\frac{\varepsilon_m \varepsilon_s}{\varepsilon_m + \varepsilon_s}\right)^{\frac{1}{2}}. \tag{1.36}$$

Fig. 1.9 illustrates that light in the sample medium could not naturally excite SPs because

$$\kappa_s = n_s \frac{\omega}{c} < \kappa_{SPR} \tag{1.37}$$

for all ω. The propagation length L_x of the surface plasmon along the interface, is defined by the $1/e$ attenuation of the SP field in the propagation direction:

$$L_x = \frac{1}{2 \cdot \mathrm{Im}(\kappa_x)} \tag{1.38}$$

As can be seen in Fig. 1.8 *(b)* the reflectance as a function of the incident angle shows a pronounced dip indicating the resonant excitation of surface plasmons. Because θ_{SPR} is past the critical angle θ_c, this excitation method is known as an attenuated total reflection (ATR)[51,53] method. The Fresnel theory can still be used to accurately describe the system. In Figure 1.10 the increase of the reflectance at the original θ_{SPR}, and the

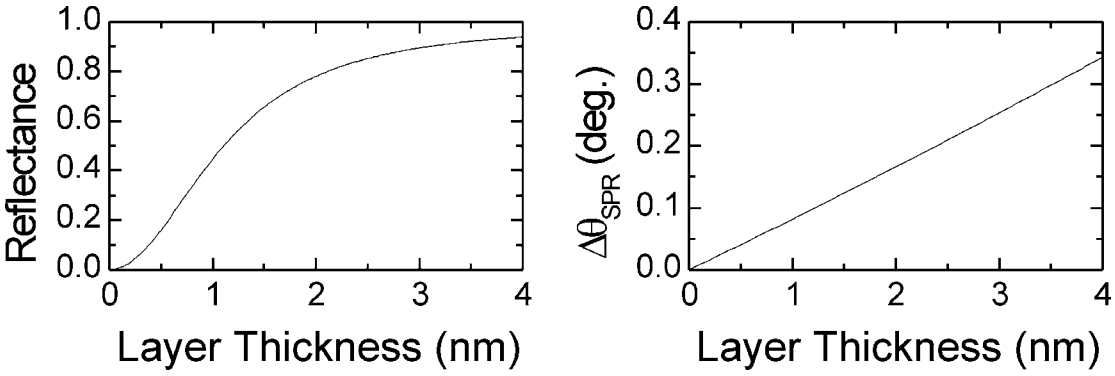

Fig. 1.10 The increase of the reflectance at the original SPR angle θ_{SPR} *(d=0)*, and the shift of θ_{SPR} as a function of the thickness of a cover layer on top of the metal layer (calculated with same parameters as for Fig. 1.8; n_{cover}=1.5).

shift of θ_{SPR} as a function of the thickness of a cover layer on top of the metal layer are given to indicate the surface sensitivity of the method. Analytical or numerical inversion enables one to determine the optical

thickness, that is, the product of the layer refractive index and thickness from the resonance angle shift $\Delta\theta_{SPR}$,

$$\Delta\theta_{SPR} \propto d \cdot n, \tag{1.39}$$

with coverlayer refractive index n, and thickness d. Using Fresnel theory we can calculate the d,n combinations that yield the same $\Delta\theta_{SPR}$ (see Fig. 1.11). The differences in the rest of the reflectance curves that can be calculated for these d,n combinations are extremely small. Therefore, measuring $R(\theta)$ is not an accurate way to separate d and n when this is needed. The same is true for measurements of the wavelength dependent reflectance. Measurements on the same layer in different media do offer a possibility,[54] but can hardly said to be a generally applicable method, especially for biological monolayers. In most cases we will use literature values for n to obtain quantitative d measurements, or be satisfied with qualitative measurements.

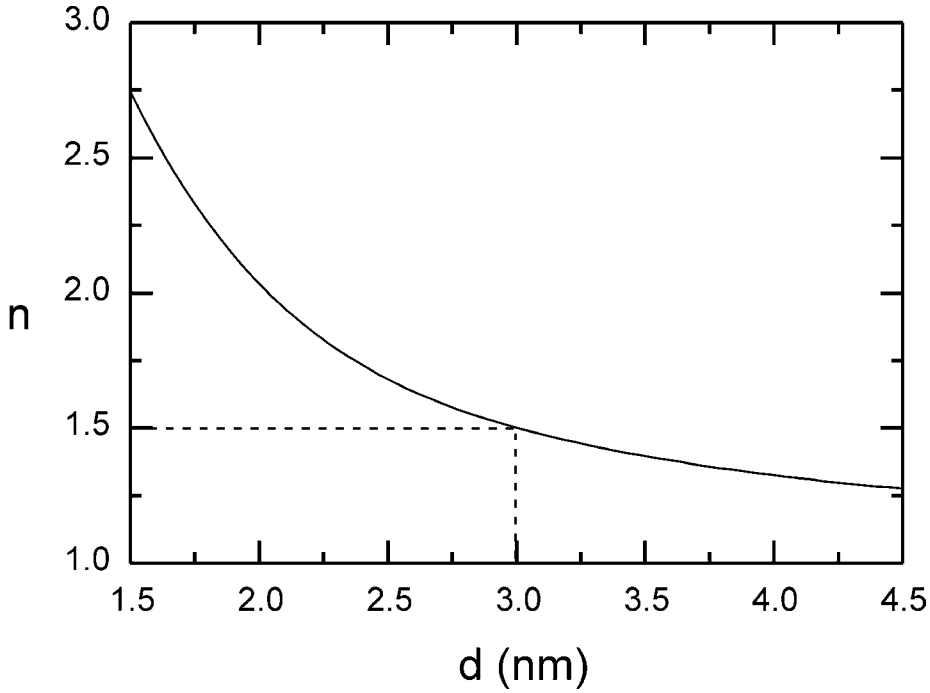

Fig. 1.11 Calculation of the d,n combinations that yield the same $\Delta\theta_{SPR}$ as d=3 nm and n=1.5.

SPR has been used in different sensor systems (see next chapter), but can also be used for imaging in a surface plasmon microscope (SPM).[47] In this case the reflected light is imaged by an objective on a camera. Areas at resonance will appear dark, while areas where the resonance condition is not fulfilled will appear bright. Pioneering work in this field was done by Yeatman *et al.*,[55,56] and Rothenhäusler *et al.*[57-59] in 1987 and 1988. Yeatman's work was aimed at developing an SPM based on a scanning focused beam[55] (lateral resolution 25 μm). The

straightforward approach with the imaged parallel beam however, proved to be much faster and instrumentationally much simpler, while the sensitivity and lateral resolution is comparable or better[58]. The lateral resolution of SPM is determined by the dissipative and radiative losses that lead to a strong damping of the surface plasmons along the wave propagation direction. An appropriate choice of the metal layer and wavelength makes a lateral resolution in the range of a few micrometers possible (see Chapter 4).

While SPM was first applied to test patterns evaporated onto the metal layer,[55-57] it was soon applied to laterally phase-separated lipid monolayers,[58,60-62] and monolayers patterned using photodesorption as a dry etching technique.[61,63] Other applications include the imaging of potential waves in electrochemical systems[64] and spatial light modulation.[65] SPM will be discussed in more detail in chapter 4 and 5.

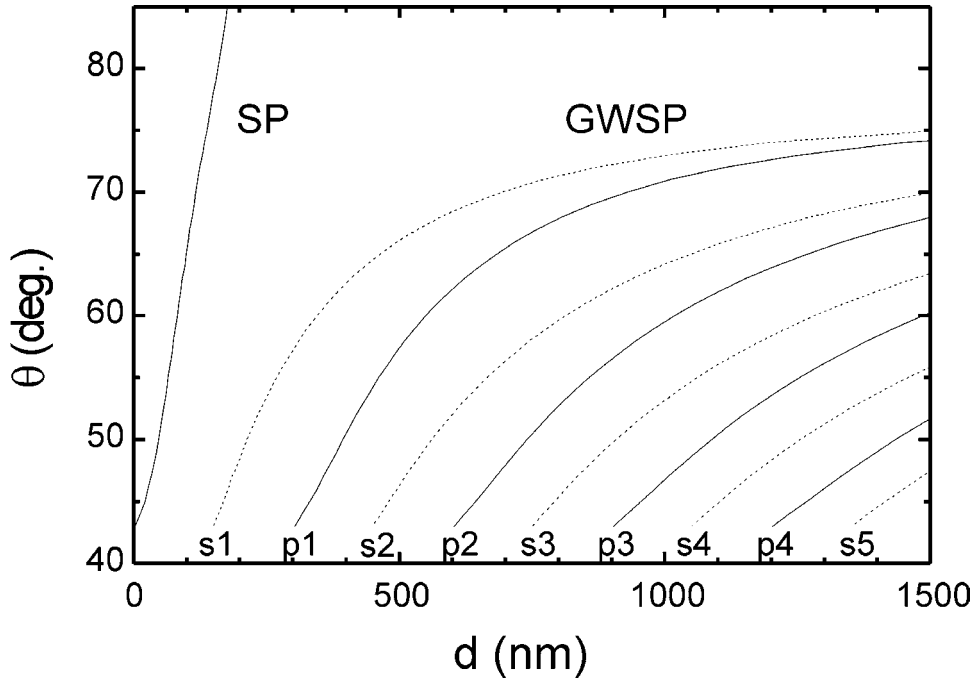

Fig. 1.12 The resonance angles of the SPs and GWSPs as a function of the waveguiding cover layer thickness (PMMA). Mode index and polarization are indicated for the first GWSPs (calculated with same parameters as for Fig. 1.8).

For sufficiently thick cover layers more than one minimum can be observed in the reflectance curve (see Fig. 1.8 *(c)*). In this case so-called guided wave surface polaritons (GWSPs)[47,50,66] are excited, with the cover layer acting as a waveguide. The light traveling through the waveguiding coverlayer is totally reflected at both interfaces with the surrounding media and fulfills the mode equation:[47]

$$\kappa_m d + \beta_0 + \beta_1 = m\pi \qquad (1.40)$$

where κ_m is the wave vector of the mode of order *m*, *d* the thickness of the waveguide, and $2\beta_i=\mathrm{Im}(r_i)/\mathrm{Re}(r_i)$ with r_i as the complex reflection coefficient at the interface between waveguide and metal r_0, and waveguide and ambient medium r_i, respectively. Fig. 1.12 displays the results of Fresnel calculations of the number and positions of the reflectance minima as a function of the waveguide thickness. For the thinnest layers (d < 200 nm) we only have the reflectance minimum due to the resonant excitation of surface plasmons, while for higher thicknesses an increasing number of guided modes is found. These GWSPs can be excited with *p* as well as *s* polarized light, and can be used in sensor measurements just like the SPR modes. The first guided modes offer a sensitivity comparable to that of the SPs but the sensitivity decreases with increasing mode index.[66,67] An advantage is that measurements for *p* and *s* polarized light can be used to separate *d* and *n* for a layer on top of the waveguiding layer.[68]

Similar considerations are valid for the microscopy variant of this technique, called optical waveguide microscopy (OWM)[69,47] using a configuration similar to that of an SPM. The fact that both *p* and *s* polarized guided modes can be used has been said to be advantageous for the study of anisotropic films.[69] It is however virtually impossible to obtain a thick waveguiding layer that is homogeneous on the nanometer scale, which complicates the study of layers on top of the waveguide, and limits it mostly to the waveguide itself.

Scanning plasmon near field microscopy (SPNM)[70] was introduced in 1992 as a new type of scanning near field optical microscope. The SPNM is essentially an SPM with a sharp STM tip probing the evanescent field of the resonantly excited surface plasmons. The scanned area is imaged via a pinhole onto a detector. The increased reflectance signal resulting from the tip disturbing the attenuated total reflection is measured when the tip is scanned a few nm above the sample. This makes essentially non-perturbative measurements possible with a lateral resolution of several nm.[70,71] The high lateral resolution of the SPNM images (showing optical structures different from topography with the tip at an average 20 nm distance[71]) is surprising in view of the propagative character of surface plasmons. A similar approach with the STM tip exchanged for an AFM tip has also been used,[72] but as the measurements were done with the tip in contact with the sample it is not really possible to separate topographical from optical contrast. In a photon scanning tunneling microscope (PSTM)[73] a sharpened fiber tip is scanned through an evanescent field, converting it into progressive waves propagating through the fiber towards a detector. This approach has been used to study the surface plasmon evanescent field at silver and gold layers.[74-76]

1.4 References

(1) Lüth, H. *Surfaces and interfaces of solid materials*, 3rd ed.; Springer: Berlin, 1995.

(2) *Surface Analysis Methods in Materials Science*; O'Connor, D. J.; Sexton, B. A.; Smart, R. St. C., Eds.; Springer Ser. Mat. Sci.; Springer: Berlin, 1992; Vol. 23.

(3) Bölger, B. In *Surface studies with lasers*; Ausenegg, F. R.; Leitner, A.; Lippitsch, M. E., Eds.; Springer Ser. Chem. Phys.; Springer: Berlin, 1983; Vol. 33, pp 2.

(4) *Spectroscopy of Surfaces*; Clark, R. J. H.; Hester, R. E., Eds.; Advances in Spectrocopy; Wiley: Chichester, 1988; Vol. 16.

(5) *Introduction to Surface Physical Chemistry*; Christmann, K., Ed.; Topics in Phys. Chem.; Springer: New York, 1991; Vol. 1.

(6) *Methods of Surface Analysis*; Czanderna, A. W., Ed.; Methods and Phenomena; Elsevier: Amsterdam, 1975; Vol. 1, pp 39.

(7) Hüfner, S. *Photoemission Spectroscopy, Principle and Applications*; Springer Ser. Solid-State Sci.; Springer: Berlin, 1995; Vol. 82.

(8) Agarwal, B. K. *X-Ray Spectroscopy*, 2nd ed.; Springer Ser. Opt. Sci.; Springer: Berlin, 1991; Vol. 15.

(9) Davis, L. E.; McDonald, N. C.; Palmberg, P. W.; Riach, G. E.; Weber, R. E. *Handbook of Auger Electron Spectroscopy*; Physical Electronics Industries: Eden.

(10) Werner, H. W. In *Electron and Ion Spectroscopy of Solids*, Fiermans, L.; Vennik, J.; Dekeyser, W., Ed.; Plenum Press: New York, 1977; pp 342.

(11) Benninghoven, A.; Rüdenauer, F. G.; Werner, H. W. *Secondary Ion Mass Spectroscopy*; Wiley: New York, 1987.

(12) Ibach, H.; Mills, D. L. *Electron Energy Loss Spectroscopy and Surface Vibrations*; Academic Press: New York, 1982.

(13) Theophanides, T. *Fourier Transform Infrared Spectroscopy*, Theophanides, T., Ed.; Reidl: Dordrecht, 1984.

(14) Griffiths, P. R.; Haseth, J. A. *Fourier Transform Infrared Spectroscopy*; Wiley: New York, 1986.

(15) Rochow, T.G.; Tucker, P.A. *Introduction to microscopy by means of light, electrons, X rays, or acoustics*, 2nd ed.; Plenum Press: New York, 1994.

(16) Reimer, L. *Scanning Electron Microscopy*; Springer Ser. Opt. Sci.; Springer: Berlin, 1985; Vol. 45.

(17) Binnig, G.; Rohrer, H.; Gerber, Ch.; Weibel, E. *Appl. Phys. Lett.* **1982**, *40*, 178.

(18) Binnig, G.; Quate, C. F.; Gerber, Ch. *Phys. Rev. Lett.* **1986**, *56*, 930.

(19) Rugar, D.; Hansma, P. K. *Phys. Today* **1990**, *43*, 23.

(20) Betzig, E.; Trautman, J. K.; Harris, T. D.; Weiner, J. S.; Kostelak, R. L. *Science* **1991**, *251*, 1468.

(21) von Tscharner, V.; McConnell, H. M. *Biophys. J.* **1981**, *36*, 409.

(22) Weis, R. M. *Chemistry and Physics of Lipids* **1991**, *57*, 227.

(23) Duschl, C.; Frey, W.; Knoll, W. *Thin Solid Films* **1988**, *160*, 251.

(24) Fischer, A.; Sackmann, E. *J. Colloid Interface Sci.* **1986**, *112*, 1.

(25) Kjær, K.; Als-Nielsen, J.; Helm, C. A.; Laxhuber, L. A.; Möhwald, H. *Phys. Rev. Lett.* **1987**, *58*, 2224.

(26) Kjær, K.; Als-Nielsen, J.; Helm, C. A.; Tippmann-Krayer, P.; Möhwald, H. *Thin Solid Films* **1988**, *159*, 17.

(27) Lee, L. T.; Langevin, D.; Mann, E. K.; Farnoux, B. *Physica B* **1994**, *198*, 83.
(28) Möhwald, H. *Rep. Prog. Phys.* **1993**, *56*, 653.
(29) Reitz, J. R.; Milford, F. J.; Christy, R. W. *Foundations of Electromagnetic Theory*, 3rd ed.; Addison-Wesley: Amsterdam, 1979.
(30) Azzam, R. M. A.; Bashara, N. M. *Ellipsometry and Polarized Light*; North-Holland: Amsterdam, 1987.
(31) Lekner, J. *J. Opt. Soc. Am. A* **1994**, *11*, 2156.
(32) Wall, J. F.; Brumfield, J. C.; Murray, R. W.; Irene, E. A. *J. Electrochem. Soc.* **1994**, *141*, 306.
(33) Duncan, W. M.; Henck, S. A. *Appl. Surf. Sci.* **1993**, *63*, 9.
(34) Kildemo, M.; Drévillon, B. *Appl. Phys. Lett.* **1995**, *67*, 918.
(35) Henck, S. A. *J. Vac. Sci. Technol. A* **1992**, *10*, 934.
(36) An, I.; Li, Y. M.; Nguyen, H. V.; Collins, R. W. *Rev. Sci. Instrum.* **1992**, *63*, 3842.
(37) Rasing, Th.; Hsiung, H.; Shen, Y. R.; Kim, M. W. *Phys. Rev. A* **1988**, *37*, 2732.
(38) Ducharme, D.; Salesse, C.; Leblanc, R. M. *Thin Solid Films* **1985**, *132*, 83.
(39) Xue, J.-Z.; Jung, C. S.; Kim, M. W. *Phys. Rev. Lett.* **1992**, *69*, 474.
(40) Hénon, S.; Meunier, J. *Rev. Sci. Instrum.* **1991**, *62*, 936.
(41) Hosoi, K.; Ishikawa, T.; Tomioka, A.; Miyano, K. *Jpn. J. Appl. Phys.* **1993**, *32*, L135.
(42) Hénon, S.; Meunier, J. *Thin Solid Films* **1993**, *234*, 471.
(43) Overbeck, G. A.; Hönig, D.; Möbius, D. *Langmuir* **1993**, *9*, 555.
(44) Tsao, M.-W.; Fischer, T. M.; Knobler, C. M. *Langmuir* **1995**, *11*, 3184.
(45) Weidemann, G.; Gehlert, U.; Vollhardt, D. *Langmuir* **1995**, *11*, 864.
(46) Weidemann, G.; Vollhardt, D. *Thin Solid Films* **1995**, *264*, 94.
(47) Knoll, W. *MRS Bulletin* **1991**, *16*, 29.
(48) Raether, H. In *Physics of Thin Films*; Hass, G.; Francombe, M.; Hoffman, R., Eds.; Academic: New York, 1977; Vol. 9, pp 145.
(49) Raether, H. *Surface Plasmons on Smooth and Rough Surfaces and on Gratings*; Springer Tracts in Mod. Phys.; Springer: Berlin, 1988; Vol. 111.
(50) Welford, K. *Opt. Quantum Electron.* **1991**, *23*, 1.
(51) Kretschmann, E.; Raether, H. *Z. Naturf.* **1968**, *230*, 2135.
(52) Jungk, G. *Phil. Mag. B* **1994**, *70*, 493.
(53) Turbadar, T. *Proc. Phys. Soc. (London)* **1959**, *73*, 40.
(54) de Bruijn, H. E.; Altenburg, B. S. F.; Kooyman, R. P. H.; Greve, J. *Opt. Comm.* **1991**, *82*, 425.
(55) Yeatman, E. M.; Ash, E. A. *Electron. Lett.* **1987**, *23*, 1091.
(56) Yeatman, E. M.; Ash, E. A. In *Proc. SPIE Vol. 897 Scanning Microscopy Technologies and Applications* **1988**, 100.
(57) Rothenhäusler, B.; Duschl, C.; Knoll, W. *Thin Solid Films* **1988**, *159*, 323.
(58) Hickel, W.; Kamp, D.; Knoll, W. *Nature* **1989**, *339*, 186.
(59) Rothenhäusler, B.; Knoll, W. *Nature* **1988**, *332*, 615.
(60) Hickel, W.; Knoll, W. *J. Appl. Phys.* **1990**, *67*, 3572.
(61) Hickel, W.; Knoll, W. *Thin Solid Films* **1990**,*187*, 349.
(62) Kooyman, R. P. H.; Krull, U. J. *Langmuir* **1991**, *7*, 1506.
(63) Sawodny, M.; Stumpe, J.; Knoll, W. *J. Appl. Phys.* **1991**, *69*, 1927.
(64) Flätgen, G; Krischer, K.; Pettinger, B.; Doblhofer, K.; Junkes, H.; Ertl, G. *Science* **1995**, *269*, 668.
(65) Yeatman, E. M.; Caldwell, M. E. *Appl. Phys. Lett.* **1989**, *55*,613.

(66) Herminghaus, S.; Leiderer, P. *Appl. Phys. Lett.* **1989**, *54*, 99.
(67) de Bruijn, H. E.; Lenferink, A. T. M.; Kooyman, R. P. H.; Greve, J. *Opt. Comm.* **1991**, *86*, 444.
(68) Lukosz, W.; Clerc, D.; Nellen, Ph. M.; Stamm, Ch. In *Eurosensors IV, book of abstracts*; Karlsruhe, 1990; pp B.7.2.
(69) Hickel, W.; Knoll, W. *Appl. Phys. Lett.* **1990**, *57*, 1286.
(70) Specht, M.; Pedarnig, J. D.; Heckl, W. M.; Hänsch, T. W. *Phys. Rev. Lett.* **1992**, *68*, 476.
(71) Pedarnig, J. D.; Specht, M.; Heckl, W. M.; Hänsch, T. W. *Appl. Phys. A* **1992**, *55*, 476.
(72) de Hollander, R. B. G.; van Hulst, N. F.; Kooyman, R. P. H. *Ultramicroscopy* **1995**, *57*, 263.
(73) Reddick, R. C.; Warmack, R. J.; Ferrell, T. L. *Phys. Rev. B* **1989**, *39*, 767.
(74) Adam, P. M.; Salomon, L.; de Fornel, F.; Goudonnet, J. P. *Phys. Rev. B* **1993**, *48*, 2680.
(75) Marti, O.; Bielefeldt, H.; Hecht, B.; Herminghaus, S.; Leiderer, P.; Mlynek, J. *Opt. Comm.* **1993**, *96*, 225.
(76) Bozhevolnyi, S. I.; Smolyaninov, I. I.; Zayats, A. V. *Phys. Rev. B* **1995**, *51*, 17916.

CHAPTER TWO

SPR SENSING

This chapter will start with a short introduction into immune reactions. Then optical evanescent field immunosensors will be discussed and we will demonstrate an SPR immuno-sensor, based on a differential detection of the SPR angle. We will also show how SPR can be used for multichannel detection of layer growth on one and two-dimensional arrays of sensor surfaces.

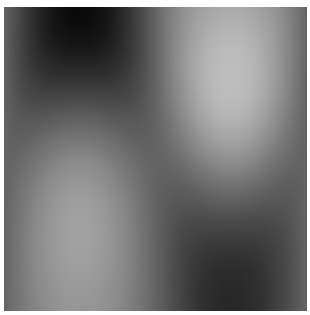

2.1 Introduction

Many studies have been devoted to the adsorption of proteins onto solid surfaces and the immunological reaction between antibody and antigen. Such studies are needed for the development of diagnostic assays, biomaterials and purification methods for proteins.

The presence of certain substances in blood or urine can be detected using diagnostic assays, based on the very specific immune reaction between antigen and antibody. These assays can be manufactured by first adsorbing a layer of antibodies on a solid phase. When a blood or urine sample, containing the antigen against which the antibody is directed, is brought in contact with the coated solid phase, the specific immune reaction occurs and the antigen will bind to the antibody. This binding, resulting in a layer growth, can be detected directly by optical methods, or indirectly by adding a labeled antibody that will bind to the antigens bound to the first layer of antibodies.

In the development of biomaterials to be used for implants one frequently aims at the precaution of blood clotting and protein adsorption on the surface of those materials. The assay technique may then be used to study which proteins adsorb onto such surfaces.

For protein purification purposes, a ligand can be bound covalently to a hydrophilic surface. The binding of specific proteins to this ligand should then be reversible, and leave the protein intact also upon release from the ligand.

2.1.1 Immune reactions

Cells of a host animal will start to produce antibodies when a compound foreign to the body (an antigen) is introduced. These antibodies will react specifically with the introduced antigen, eventually destroying it. The parts of the antigens that evoke this immune response are known as antigenic determinants. After some time, a heterogeneous population of antibodies will be created, each of which will only recognize one specific antigenic determinant. However, the different antibodies (polyclonal antibodies) are specific for different sites at the antigen, and many antigenic determinants will be recognized. Monoclonal antibodies (all specific to the same antigenic determinant) can be produced by selecting and cloning individual antibody cells. This makes it possible to produce antibodies with a constant quality, and to improve their specificity in diagnostic assays.

A frequently applied method to immobilize proteins at a solid surface is physical adsorption. The increase in entropy by the release of

ordered water molecules at the surface of the protein and substrate make adsorption energetically favorable. Most proteins adsorb very rapidly onto hydrophobic surfaces and almost no desorption occurs when the surface is washed with a buffer solution. Another immobilization method is the formation of covalent bonds between the protein and the surface. For this work however, only physical adsorption was used for the immobilization of proteins.

Proteins have compact, tightly folded structures, made up out of one or more polypeptide chains. Under physiological conditions, globular proteins spontaneously adopt their native conformation. Because many proteins have an elliptical shape their orientation at the interface is important as well. It determines the thickness of the monolayer and whether the binding sites for the antigens are exposed to the aqueous medium.

The reversible reaction between an antigen binding site at the antibody (*Ab*) and a certain site at the antigen (*Ag*), can be described by

$$Ab + Ag \underset{k_d}{\overset{k_a}{\rightleftarrows}} AbAg\,, \tag{2.1}$$

with k_a and k_d as the association and dissociation rate constants, and *AbAg* indicating the antibody-antigen complex. The affinity constant K_a (l/mol) is defined by

$$K_a = \frac{k_a}{k_d} = \frac{[AbAg]}{[Ab]\cdot[Ag]}. \tag{2.2}$$

The nature of the formation of the immune complex obviously depends on whether the antibodies are monoclonal or polyclonal. In the former case, only one antigen can react with every antibody, while in the latter more antigens can bind to one antibody.

For diagnostic assays either the antibody or the antigen is immobilized on the solid phase, and therefore a number of factors influence the formation of the immune complex: *(i)* Diffusion of the immune compound in the solution can limit the reaction, especially at low concentrations. *(ii)* The immune reactivity of the adsorbed protein might be affected by conformational changes that can take place during the immobilization. *(iii)* The orientation of the protein molecule after immobilization might make the binding sites inaccessible. *(iv)* If the surface concentration of the immobilized protein is too high, the binding sites might not always be accessible for the complementary immune compound, because of steric hindrance.

2.2 Immunosensors

In immunosensing the formation of the immune complex is detected via an appropriate transduction event. Transducing systems for direct detection of antibody-antigen interactions include gravimetric, potentiometric, acoustic and optical devices.[1,2]

Sensitivity is obviously an important requirement for these sensors, but also speed, the ability to do measurements on low volume samples, and the possibility to regenerate the sensor after use are important. Preferably it should be possible to measure in more than one channel for reference, difference or multiparameter measurements. For successful commercialization the instrument should also be small, cheap and easy to use.

2.2.1 Optical evanescent field immunosensors

In the last years, progress has been made particularly in the field of optical evanescent field immunosensors. With these sensors, biomolecular interactions within the evanescent field are detected via a change in the refractive index or layer thickness at the sensor surface, and labeling of antigens is not required. A number of different configurations has been used.

In grating coupler waveguide sensors[3] the effective refractive index of a guided mode is changed by the adsorption of molecules at the waveguide surface. The change is detected as a shift of the incoupling angle for the excitation of the guided mode. For an optimal excitation the output at the end face of the waveguide is maximized.

The refractive index changes within the evanescent field of waveguides can also be detected interferometrically. In the Mach-Zehnder waveguide interferometer[4] a light beam is split and made to propagate through the waveguide in a reference arm and a signal arm. After that, the light is recombined and the interference signal results.

In the waveguide SPR sensor[5] instead of a prism, coupling between a dielectric monomode waveguide and a metal cover layer is used. This makes the design of integrated sensors easier.

The resonant mirror (RM)[6,7] is aimed at combining the enhanced sensitivity of the waveguiding devices (due to the longer interaction length as compared to SPR sensors) with the ease of construction and operation of SPR sensors. In a configuration similar to that of Kretschmann, the metal layer is replaced by a dielectric layer structure. The waveguide is interrogated by a combination of *p* and *s* polarized light. If *p* and *s* polarized light excite corresponding modes in the

waveguide, the phase difference between the reflected *p* and *s* beams is π,[6] which can be easily measured by using an appropriately placed polarizer in the reflected beam. A sharp peak is thus observed in the reflectance as a function of the angle of incidence. The position of this peak is sensitive to changes at the sensing interface.

Because in waveguides in most cases *p* and *s* polarized modes can be excited, more information can be obtained and the values for layer thickness and refractive index of the adsorbed layer can be separately determined, unlike with common SPR systems.[8] Waveguide sensors in general also have the advantage of a higher sensitivity due to a propagation length which is much longer than in SPR sensors.[8] The interaction length in SPR devices can, however, be adjusted by choosing an appropriate wavelength and metal layer. By doing this, the interaction length (~ propagation length of the SPs) can be varied from less than 1 μm in the UV to several mm in the IR.[9] Moreover, SPR sensors are more surface specific, because their evanescent field is confined to a smaller distance from the interface. The much shorter propagation length makes SPs less sensitive than guided modes,[8] but at the same time this makes SPR a better option for 2D array multisensors. The smaller sensitive area also implies that smaller sample volumes are needed for the same surface density. Finally, high light intensities can easily be coupled in, and increase the signal to noise ratio.

SPR sensors have also been used as gas sensors for halothane,[10,11] ammonia[12] and NO_2,[13] after coating the metal layer with an appropriate chemical sensing layer, and even as a temperature sensor.[14] Most often however, they are used as immunosensors for the label-free detection of biomolecular interactions in real time.[15,16] Applications for immunosensors can be found in medical science (diagnostic assays, drug monitoring), environmental monitoring (pesticide detection) and industrial processes (concentration determination, in-line process monitoring). The biomolecular interactions that have been studied include the kinetics of association and dissociation of antigens and antibodies, the activity of enzymes and hormone-receptor interactions. SPR sensors have also been used to assay for specific nucleic acid sequences.[17]

Although evanescent field optical sensors have a high sensitivity, their specificity as biosensors has to be provided by biochemistry. When molecules are studied that are not directly detectable (*i.e.* the refractive index or thickness change is too small), the small molecules can be immobilized and detected using biomolecular recognition by larger molecules. The sandwich assay is another method that can be used when a layer growth is too small to be detected directly. In this case the antigens are ‘labeled’ with a secondary antibody, before or after binding

to the first antibody at the surface. Other possibilities include displacement assays, replacement assays and inhibition assays.[18] Very often however, direct monitoring of the binding of the antibodies to the antigens immobilized on the sensor surface is possible.

2.2.2 SPR detection

Different detection principles have been used to detect the resonant excitation of surface plasmons and the shift in the condition for this excitation caused by refractive index changes within the evanescent field. The most straightforward method is probably to keep the incident angle fixed at a value for which the reflectance is half way down its minimum and monitor changes in the reflectance.[9,10,13,16,19] However, the linear region is rather small and the incline (or width) of the resonance curve might change appreciably during the monitored process. Angular scans using a rotation table offer the possibility of using Fresnel theory to obtain the layer parameters from a fit of the reflected intensity as a function of the angle of incidence over a large range of angles. A single scan however usually takes several minutes, and thus even slow changes cannot be monitored in real time.[14,20-22] Angular scans can be speeded up by using a scanning mirror.[23]

It is also possible to measure the reflectance curve fast by using a convergent light beam covering a suitable interval of incidence angles reflected at the prism base and imaged onto a photodiode array. The resonance angle can then be determined from the position of the minimum on the detector array (using a fitting algorithm).[24] Using the second dimension of a CCD detector a one-dimensional array of sensing areas could in principle be used simultaneously.[20,25-28] This however, has not yet been demonstrated in a sensor measurement.

Another possibility is to use the wavelength dependence of SPR. The angle of incidence is kept fixed and a broadband lightsource is used. Only one wavelength will couple to the SP, and a spectral analysis of the reflected light will show an absorption dip at this wavelength.[29] This detection principle has also been used to detect SPR in a miniaturized setup where the plasmons are excited in the metal-cladded tip of a multimode fiber. At the fiber end face the light is reflected by a mirror and half of the light is guided back to a spectrometer where the resonance wavelength is measured.[30]

Using an acousto-optic tunable filter (AOTF) the differential reflectivity as a function of the wavelength has been measured. To do this, a frequency modulation is added to the drive signal of the AOTF to modulate the wavelength of the output. The wavelength modulated

reflectance is measured by a lock-in amplifier which results in a signal which is proportional to the differential of the reflectance with respect to the wavelength.[31]

With an acousto-optic deflector (AOD) the differential reflectance with respect to the incident angle has been measured as well. This has been published as a patent only.[32] We will use a smaller, cheaper and simpler way to modulate the incident angle and present results of immunosensor measurements using this system.

2.3 Differential SPR sensing

We will use a beam with a modulated angle of incidence in a SPR sensor device. Thereby, only angle dependent signals are measured, using a lock-in amplifier. Apart from the advantage for the signal to noise ratio this also implies that we can measure the first derivative of the dip in the SPR curve. This makes feedback to the incident angle possible, keeping it at the SPR angle (null detection), and results in a measurement with a very high dynamic range. With a device (see Fig. 2.1) that can be very small the SPR angle can be measured as a function of time, monitoring an adsorption or an immunoreaction, as will be demonstrated. The angular measurement can be made into an absolute one, if the critical angle is included in a scan.

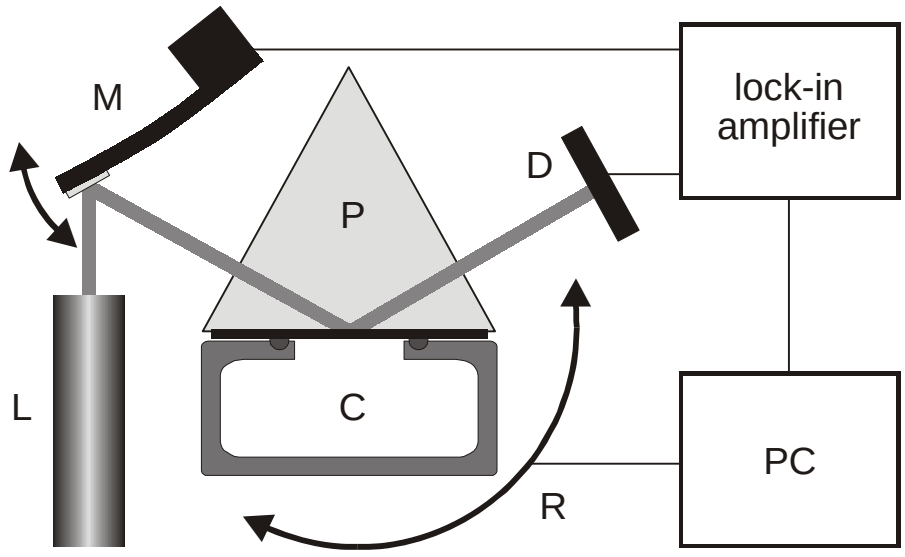

Fig. 2.1 Differential SPR sensor setup. L: HeNe laser; M: piezoelectric modulator with mirror; P: prism; C: cuvet; D: photodiode; R: rotation table. The lock-in amplifier provides the modulation voltage, and is connected to a PC. For measurements with feedback the PC can control the rotation table.

By measuring the DC reflectance as well as the AC component and second harmonic, the three main features of the SPR reflectance curve can be measured simultaneously: dip depth, position and width. In general, changes in the refractive index profile in the evanescent field will result in a change of any of these three parameters of the SPR reflectance

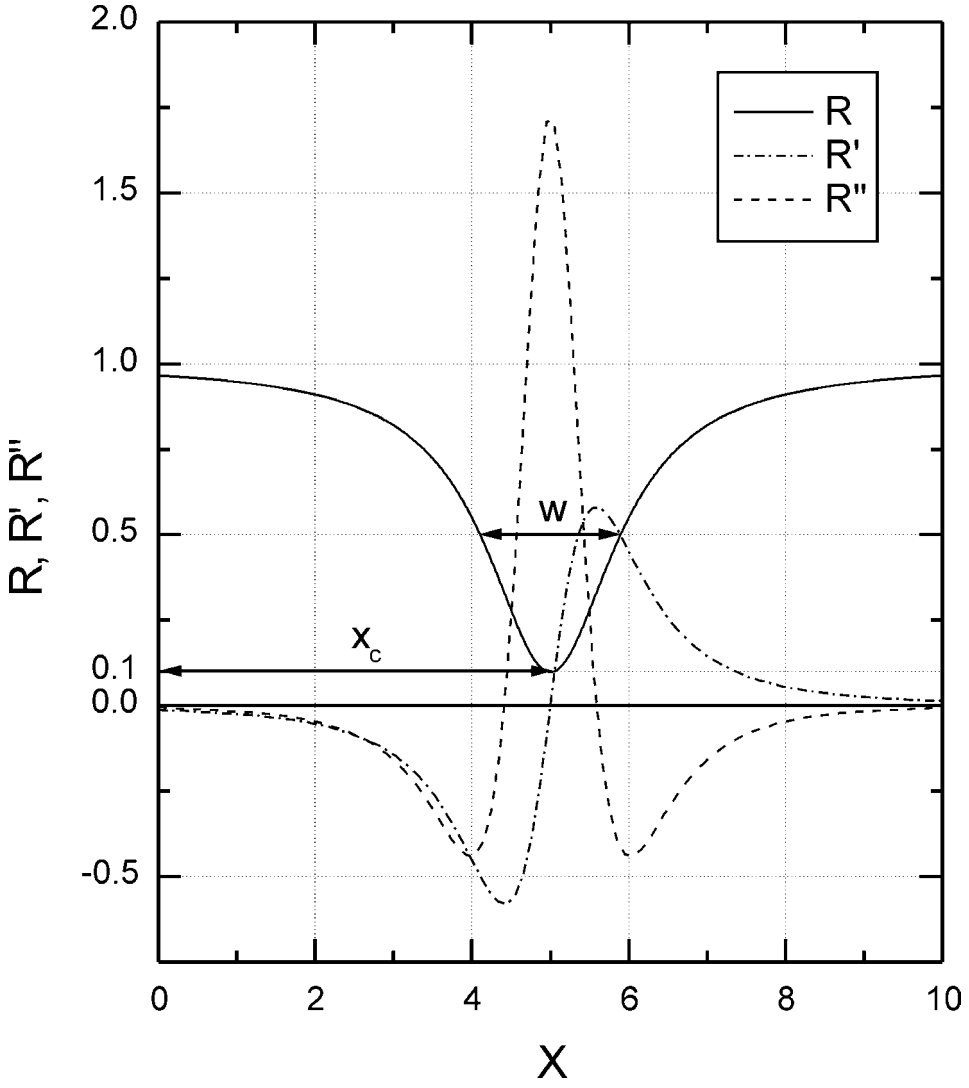

Fig. 2.2 A Lorentz curve according to Eq. 2.3 which approximates the shape of an SPR reflectance curve around the minimum. Its first and second derivative are plotted as well. These curves were calculated for w=2, x_c=5 and d=0.1 (see Eq. 2.3).

minimum. These values can give a quick Lorentz approximation of the SPR reflectance curve around the SPR minimum (see Fig. 2.2):

$$R(x) = 1 - \frac{\left(w - dw/2\right)^2}{w^2 + 4\left(x - x_c\right)^2}, \qquad (2.3)$$

with x_c and d as the position and depth, and w as a measure for the width. The second derivative in the minimum is directly related to the width:

$$R''(x_c) = \frac{2(d-2)^2}{w^2}, \tag{2.4}$$

or for $d \ll w$:

$$R''(x_c) = \frac{8}{w^2}. \tag{2.5}$$

In the case of a bare metal layer the position, depth and width values could even be used to directly calculate approximate values for the complex refractive index and the thickness of the metal layer.[33]

A spread in the thickness of a measured layer (due to roughness) is known to change the shape of the resonance minimum.[21] An antibody-antigen / aqueous interface is an example of such a rough surface. Theoretically and experimentally this leads to an increase in the width of the resonance curve as compared to the case of a smooth layer with the same average thickness. The position of the resonance angle however, is not influenced.[14] Therefore, the measurement of resonance depth and width will give more information than a measurement of the dip position only.

If feedback on the incident angle with the rotation table is not used, the sensor output is still linear around the resonance minimum. The shape of the reflectance curve around the resonance minimum is similar to a parabola and therefore, the first derivative is almost linear. With a high frequency, low amplitude modulation of the incident beam the SPR measurement is fast and the beam probes one fixed spot on the surface. This makes this detection method a very good option for scanning a two-dimensional array of sensor surfaces. In this case the second derivative would give the (change of the) sensitivity during a measurement; something that normal fixed angle measurements cannot do.

2.3.1 Experimental section

A standard HeNe-laser (2 mW) was used as a light source. The angle of incidence was modulated by placing a piezo-electric strip with a small mirror in the light path. By applying a sine voltage (255 Hz) to the piezo actuator the strip will bend slightly and the angle of incidence will be modulated in an approximately sinusoidal way (typical amplitude: <0.1 deg.). The modulated lightbeam is used to excite surface plasmons in the Kretschmann configuration (Fig. 2.1). A simple cuvet is pressed against the 46 nm gold layer evaporated (1 nm/s at 10^{-6} mbar) on the

surface of a 60° prism (BK7 glass), allowing measurements to be made in liquid media. The prism / cuvet combination can be rotated with a rotation table (MicroControle Systems; accuracy: 1 mdeg.), to feedback the AC signal to the angle of incidence or to make an angular scan. A photodiode connected to a preamplifier and a lock-in amplifier (Stanford Systems Inc.) is used to detect the modulated reflectance (DC, AC and second harmonic).

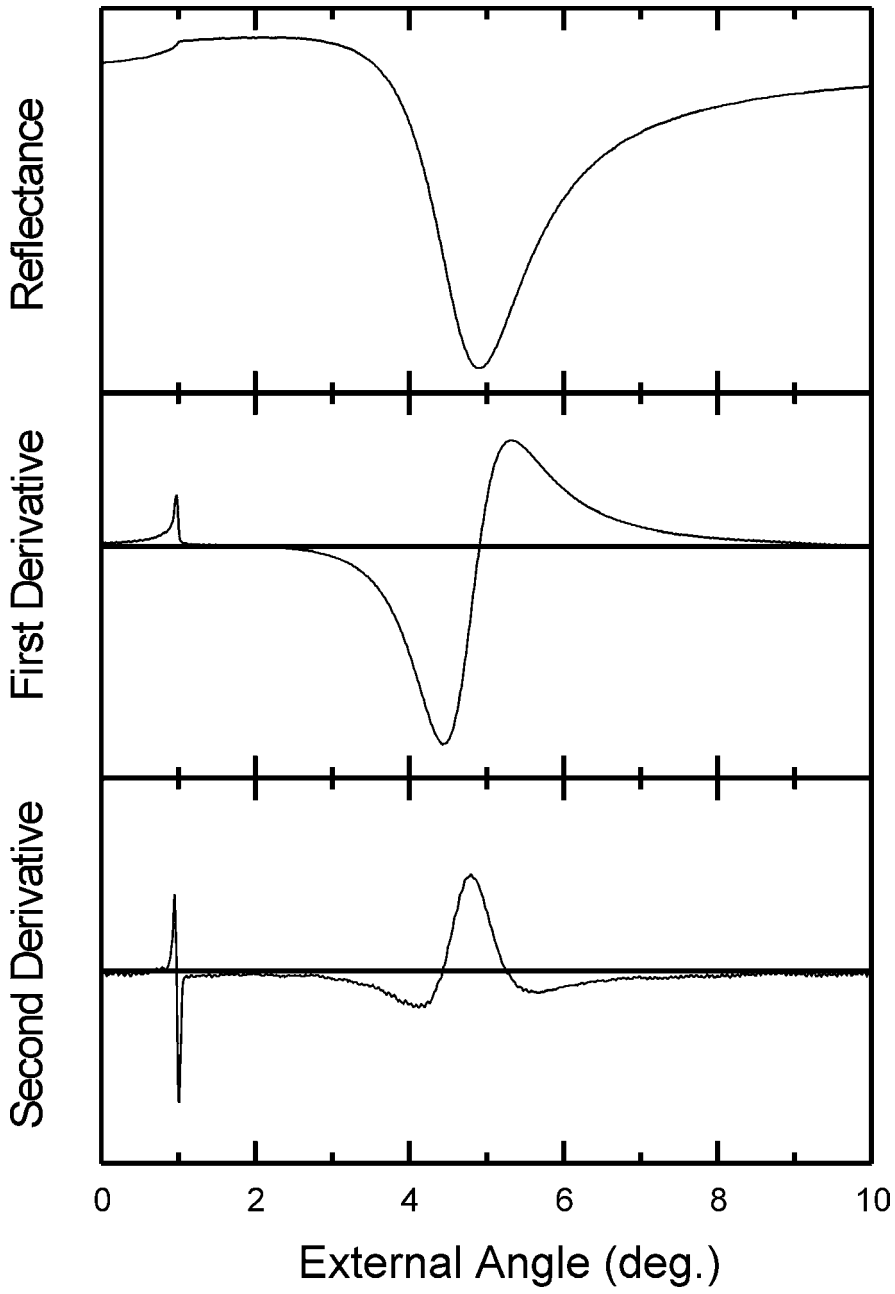

Fig. 2.3 The reflectance curve for a bare gold layer in air as well as its first and second derivative, measured simultaneously as a function of the relative angle of incidence. The angle of incidence is always measured externally in this chapter (for definition, see Fig. 1.8).

To render the gold layer hydrophobic, a thiol layer (mercapto-pentadecane) was deposited on top of it by self-assembly from a solution in ethanol. Proteins were obtained from Sigma (St. Louis, USA) and used without further purification. All solutions were made using phosphate buffered saline (PBS pH 7.3).

2.3.2 Results and discussion

Figure 2.3 shows the result of an angular reflectance curve measurement for the bare gold layer in air. Using the setup described the reflectance can be measured as a DC, AC and second harmonic signal with the lock-in amplifier. These signals correspond to the reflectance and its first and second derivative with respect to the angle of incidence. In the first derivative we can see a peak caused by the sudden change of the slope of the reflectance curve at the critical angle. Since the critical angle only depends on the media on either side of the layer system, it can be used as a reference to turn the relative angular measurement into an absolute one. At the SPR angle we have a zero crossing for the first derivative. In a sensor measurement we can use the AC signal as a feedback to follow the SPR resonance angle. By interpolation, using the error signal, the angular resolution can be further improved, not limited by the angular resolution of the rotation table but by the signal to noise ratio (see Fig. 2.4*(a)*).

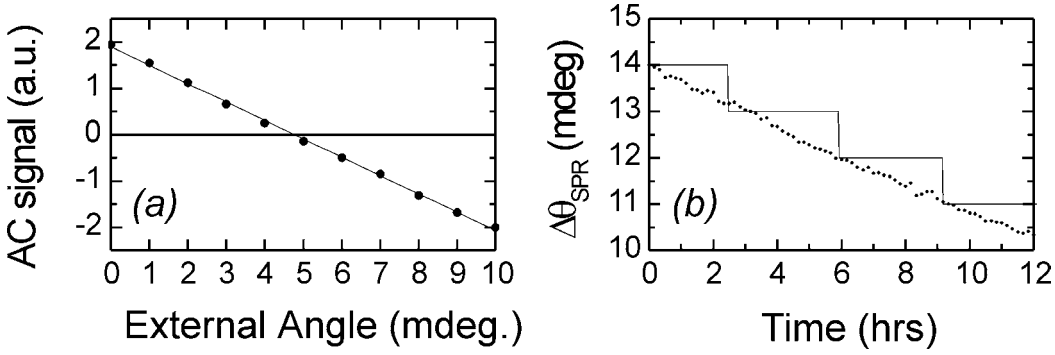

Fig. 2.4 ***(a)*** Scan of the AC signal around θ_{SPR} in air (without feedback); the line is a linear fit. ***(b)*** Stability measurement in air, demonstrating the drift in the sensor measurement when chemical causes are excluded. The line represents the position of the rotation table; the points represent the values corrected with the feedback signal.

To get an idea of the physical stability, a 12 hour sensor measurement with feedback was performed in air, in which case no significant shift of the SPR angle is expected (see Fig. 2.4*(b)*). The slope of the zero crossing was used to estimate an appropriate threshold value

that the feedback signal should exceed before the incident angle was incremented by 1 mdeg. using the rotation table.

Using Fresnel theory we can calculate the sensitivity of the SPR angle to a protein layer growth (approximate refractive index: 1.5) in an aqueous medium (refractive index: 1.33). This results in an almost linear relation with a slope of about 0.26 deg/nm, which means that an angular shift of 1 mdeg. (externally measured) corresponds to a layer growth of about 4 pm. Using literature values for the refractive index of water as a

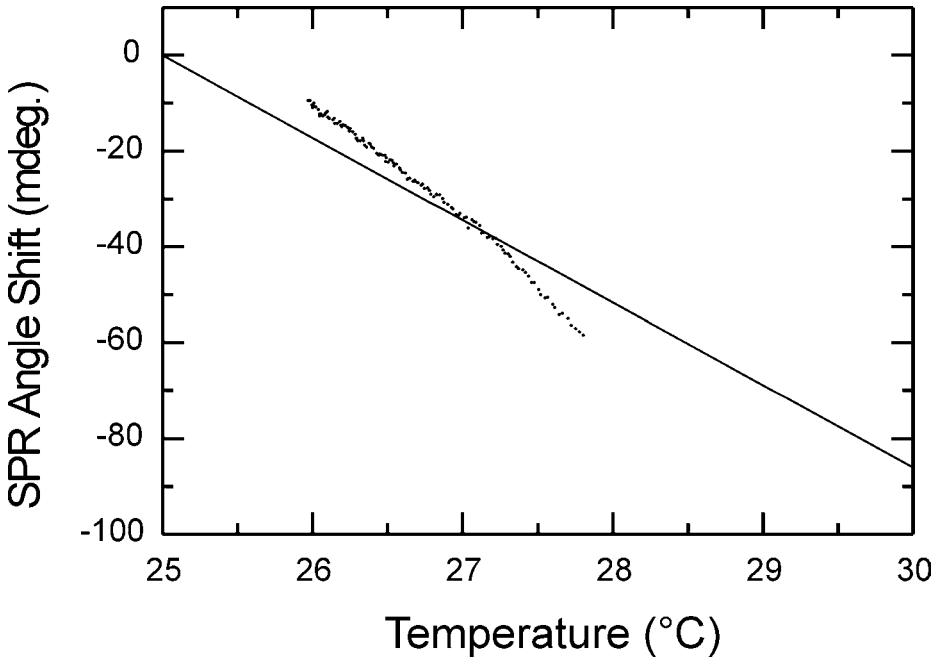

Fig. 2.5 SPR angular shift as function of temperature, measured in PBS. The temperature was measured in contact with the metal cuvet.

function of temperature,[34] the dependence of the resonance angle on the temperature of the aqueous bulk medium can be determined using Fresnel theory as well. Experimentally the influence of the temperature is higher than expected theoretically (see Fig. 2.5). Most probably this means that the temperature influences the dielectric constant of the metal layer and maybe also that the temperature of the water near the interface is higher (the slope of the experimental curve in Fig. 2.5 is comparable to the theoretical slope around 50°C).

Figure 2.6 shows the result of an experiment where an immunoreaction was monitored with the setup. The hydrophobized gold layer was first coated with human serum albumin ($2 \cdot 10^{-6}$ M hSA). After a washing step the content of the cuvet was exchanged for $2 \cdot 10^{-7}$ M αhTRF (anti human transferrin) to test for specificity. No growth was observed

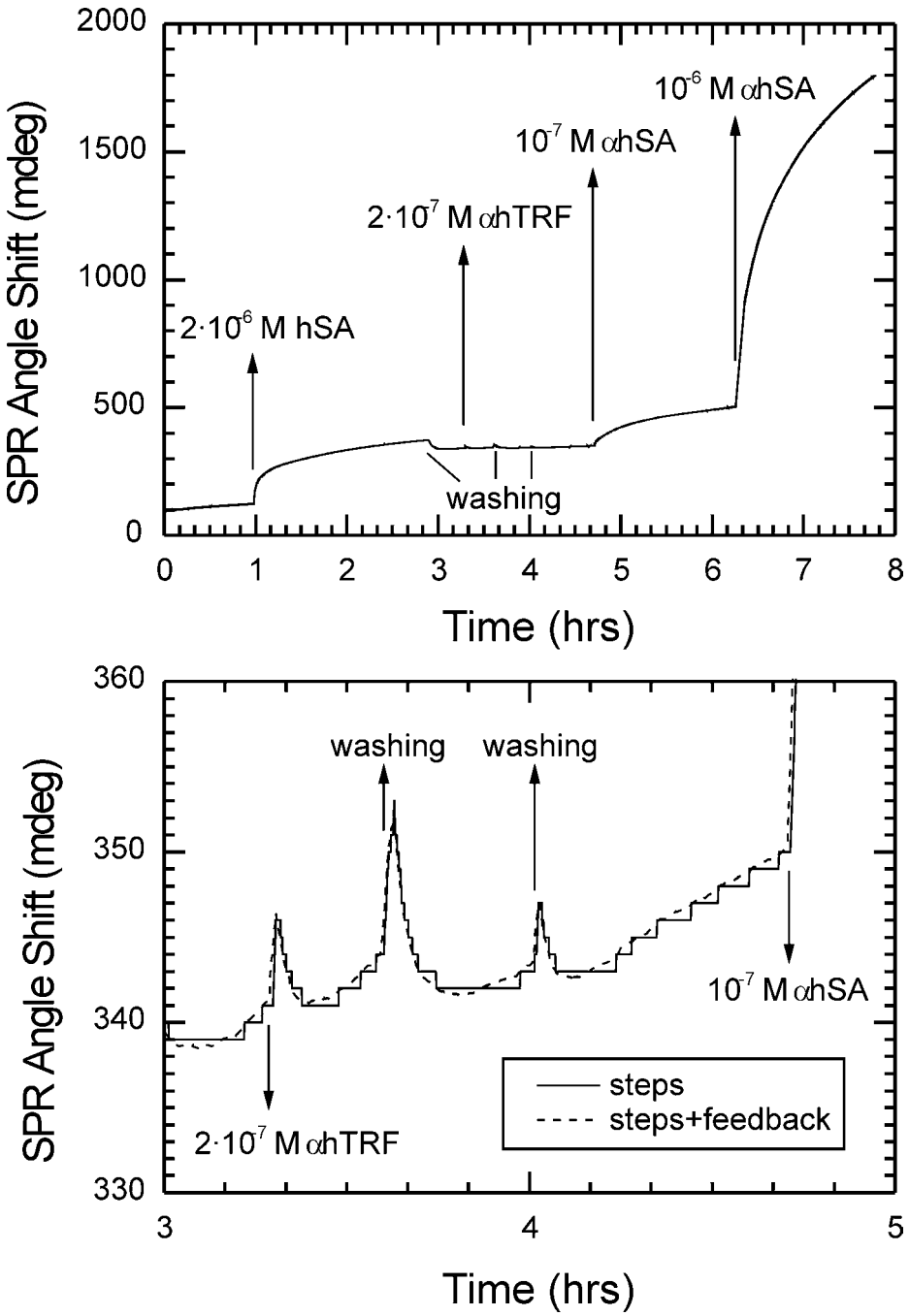

Fig. 2.6 ***(a)*** Example of an immune reaction monitored with the differential SPR sensor using feedback. ***(b)*** Close-up of the same measurement demonstrating the sub-mdeg. resolution.

until (after several washing steps) 10^{-7} M αhSA was used. As can be seen in Figure 2.6*(b)* the accuracy of the angular measurement is better than 1 mdeg. The slight increase in the signal after the washing steps can probably be explained by temperature changes. The use of a flow cell would reduce the measuring time greatly, thereby reducing drift problems. When a flow cell is used one can also completely exchange one

solution for another, which is not possible with a static cuvet, without drying the interface.

The result of measuring DC, AC and second harmonic reflectance signals during an immunoreaction is presented in Figure 2.7. The position of the SPR dip shifts as it did in the last experiment, the dip depth

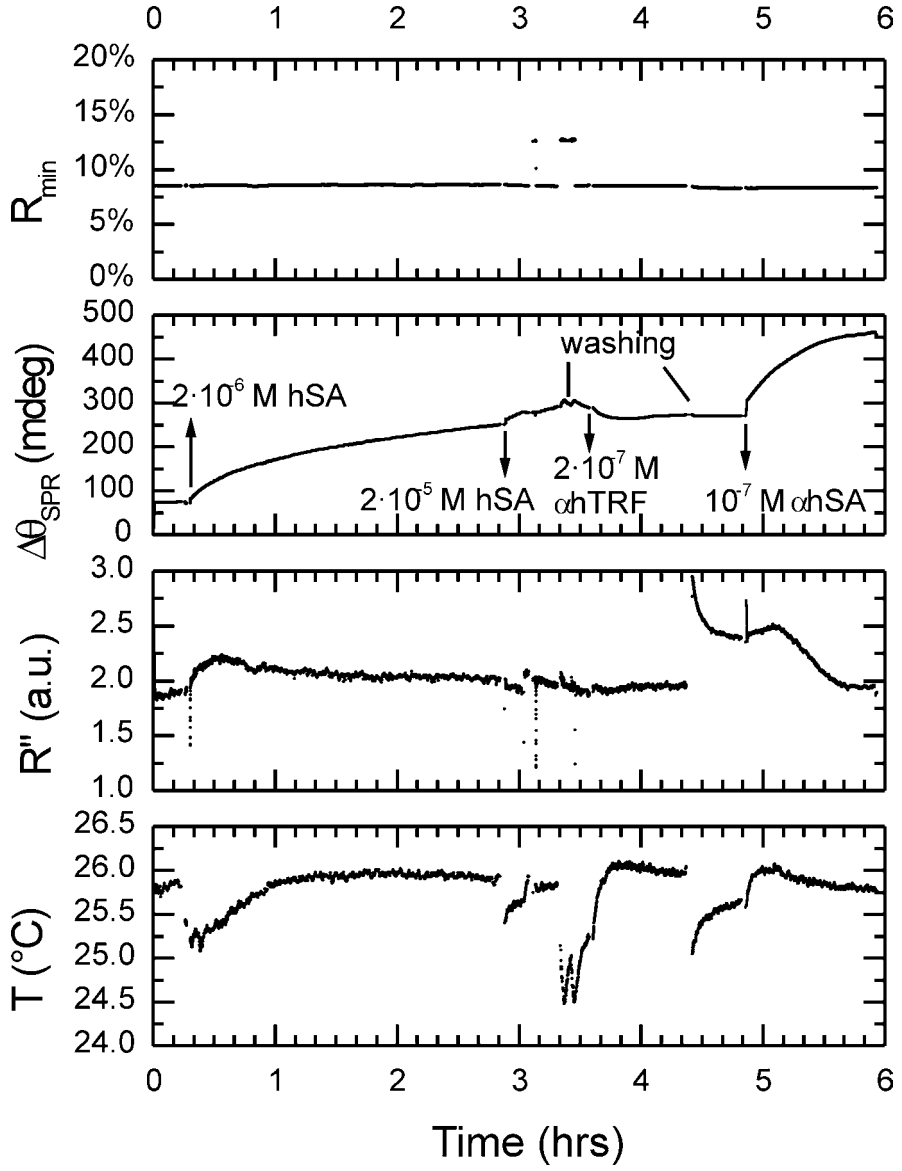

Fig. 2.7 Measurement of immobilization of hSA antigens and subsequent steps: blocking with hSA, washing, testing for specificity with αhTRF and the specific immune reaction with αhSA. Reflectance (DC), resonance angle shift and second derivative of the reflectance were measured, as well as the temperature.

however hardly changes. The second derivative of the reflectance at the resonance angle depends on temperature (measured in contact with the metal cuvet) as well as surface structure, in a way that is not clear from

this experiment alone. The resonance width is expected to decrease with an increase of temperature (a lower refractive index leads to a lower SP damping), and increase with increasing surface roughness (the roughness leads to a higher damping).

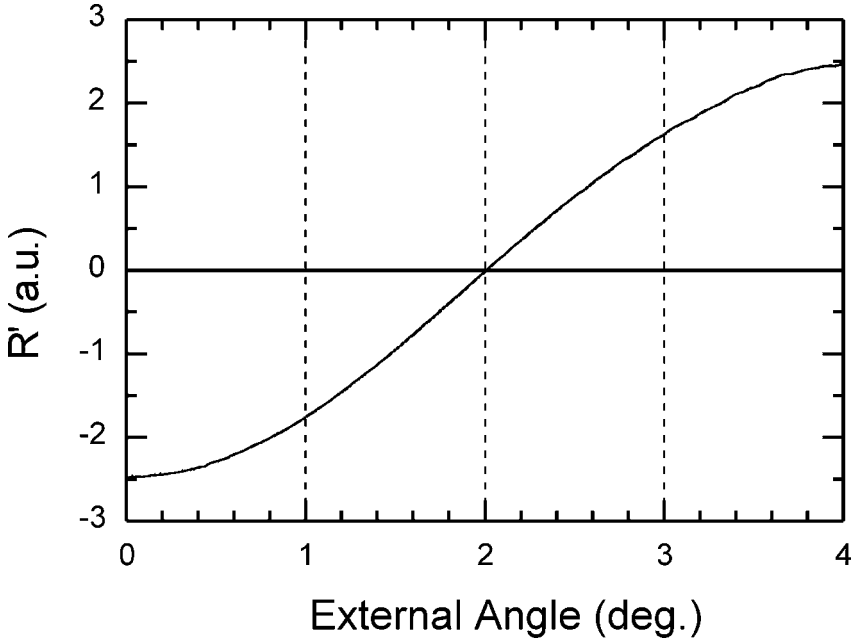

Fig. 2.8 Scan of the AC signal around θ_{SPR} in PBS, demonstrating the linear range (2 deg. externally or about 8 nm of protein layer growth) when feedback is not used.

The linear range of the differential measurement without feedback is about 2 deg. as can be seen in Figure 2.8. This range is generally sufficient for immunosensor measurements. It simplifies the setup, and makes fast multichannel measurements possible, by scanning the modulated laser beam over a number of sensing areas on one sensor surface. Because the modulation amplitude is small, the movement of the spot is much smaller than the spot itself, which therefore is essentially stationary on one sensing area. Using a glass cube rotated by a stepping motor the beam with a fixed angle of incidence (except for the modulation) was scanned past three sensing areas, without feedback. A multichannel flow cell was used to lead different solutions past the sensing areas. The result of this experiment is shown in Figure 2.9. By rotating the glass cube around another axis two-dimensional arrays could be scanned as well.

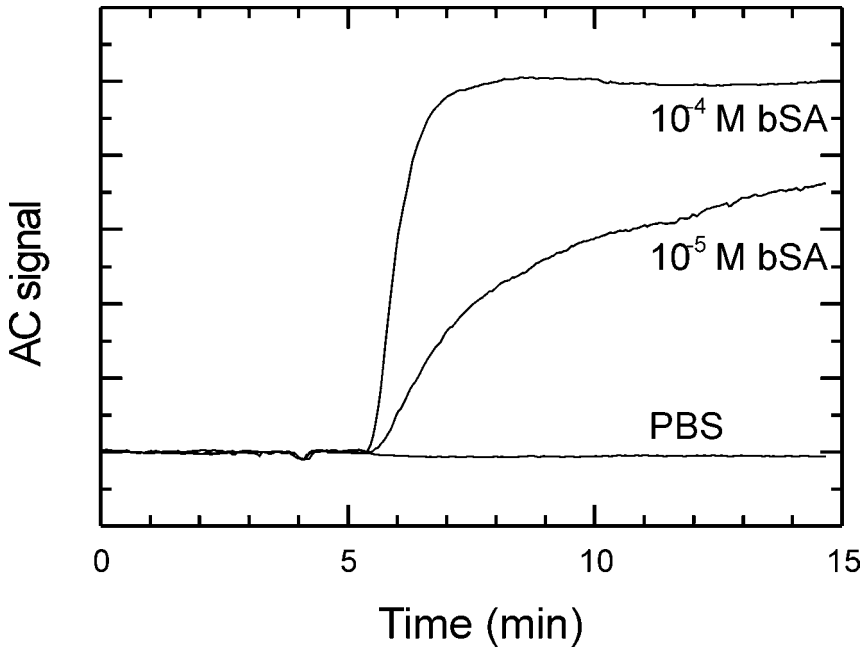

Fig. 2.9 Multichannel differential measurement of bovine serum albumin (bSA) adsorbing to the gold surface. The small dip before the increase of the signal arises from local heating of the buffer solution when the pump is stopped to exchange the buffer solution for a bSA solution.

2.3.3 Conclusion

The SPR angle could be measured accurately (resolution better than 1 mdeg.) and fast (several ms) using a differential measuring technique where the angle of incidence was modulated. Using a lock-in amplifier gave the usual advantages of an improved signal to noise ratio and the elimination of the influence of ambient light (the measurement can continue during sample manipulation). A rotation table was used to do measurements with feedback and a high dynamic range. When the rotation table is left out, the dynamic range is still sufficient for immunosensing. This allows the modulated beam to be scanned over an array of sensing areas without feedback, as was demonstrated. The light spot is stationary and the measurement is fast; these are essential advantages for this option. The fact that almost no moving parts are used add to the simplicity and the mechanical stability of the setup.

2.4 SPR multisensing

In this section we will demonstrate how SPR can be used for multichannel immunosensing measurements. For the first time, four separate immunoreactions have been monitored simultaneously in real time. To do this, a plasmon carrying gold layer against which a four channel flowcell was pressed, was imaged at a fixed angle of incidence. Taking the method a step further we have first coated the four channels with antibodies then turned the flowcell by 90° in such a way that the flow channels overlapped the areas coated in the first step. In a second step antigens were applied to the different antibodies on the surface. Thus all antibody-antigen combinations can be measured in a two-dimensional array of sensor surfaces in real time.

2.4.1 Introduction

There are a number of reasons why multisensing is desirable: *(i)* simultaneous measurements save time; *(ii)* leading a solution past a number of sensor surfaces is preferred when only a low sample volume is available; *(iii)* multi-analyte mixtures can be measured; *(iv)* reference and duplo measurements can easily be included.

Because SPs have a short propagation length (for gold and in the visible part of the spectrum typically in the μm range), they are particularly well suited for imaging a two-dimensional array of small sensing areas. All sensing areas can be present at the same sensor surface, and the imaging system allows measurements to be made on different spots of the sample simultaneously and independently. The fact that the sensor surfaces are visually observed in real time (and thus problems such as passing air bubbles can be detected) is a practical advantage of this method. By recording the images on video tape the size and position of the sensor surfaces can also be chosen after the measurements. Other advantages are the inherent sensitivity of surface plasmons and the instrumentational simplicity. Finally, because small sensor surfaces can be defined relatively few molecules are needed to obtain a certain surface density.

2.4.2 Experimental section

The experimental setup is shown in Fig. 2.10. The sample delivery system consisted of a four channel flowcell and peristaltic pump. The flowrate used was 4.9 ml/hr. Layers of 2 nm Ti and 47.8 nm Au were evaporated on a glass slide which was brought in contact with a prism

(BK7 glass; n=1.515) using a suitable matching oil. A light beam from a 2 mW HeNe laser (λ=632.8 nm) was expanded to a 2 cm diameter and attenuated by a factor of 300. The angle of incidence was chosen slightly to the left (see Fig. 1.8) of the minimum in the reflectance curve, therefore the increase in reflectance will be approximately linear with the increase in layer thickness. After internal reflection in the prism the light was imaged by a large diameter lens (f=90 mm) on a CCD video camera with a linear response (VCM 3250; Philips). Images were recorded on videotape for later analysis. A video digitizer (VisionPlus AT OFG; Imaging Technology, Inc., Woburn, MA) was used to calculate the

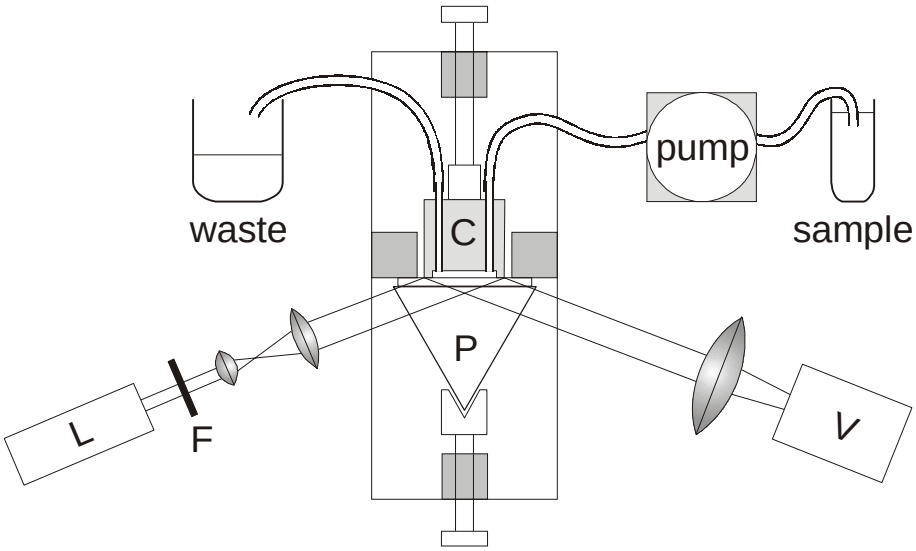

Fig. 2.10 Schematic representation of the setup used for the multichannel measurements. L: HeNe laser; F: gray filter; P: prism; C: multichannel flowcell; V: video camera.

average intensity of the defined sensor areas in the image as a function of time when the tape was played back. All chemicals were kindly provided by Organon Teknika (Boxtel, The Netherlands). Solutions were prepared in PBS (pH=7.3). Human chorionic gonadotrophin (hCG) and luteinizing hormone (LH) were used as antigens. Three different monoclonals of the αhCG antibody ([1C],[7B],[3A]) were used as well as an αLH antibody. Bovine serum albumin (bSA) was used to block unoccupied sites after the initial adsorption of antibodies to avoid unspecific adsorption of antigens.

2.4.3 Results and discussion

One-dimensional array of sensor surfaces

As an initial experiment the adsorption of bSA was measured with three different concentrations and a reference channel without bSA. Fig. 2.11 shows the result of this experiment which agrees with the expectation that for a lower concentration the adsorption will proceed slower.

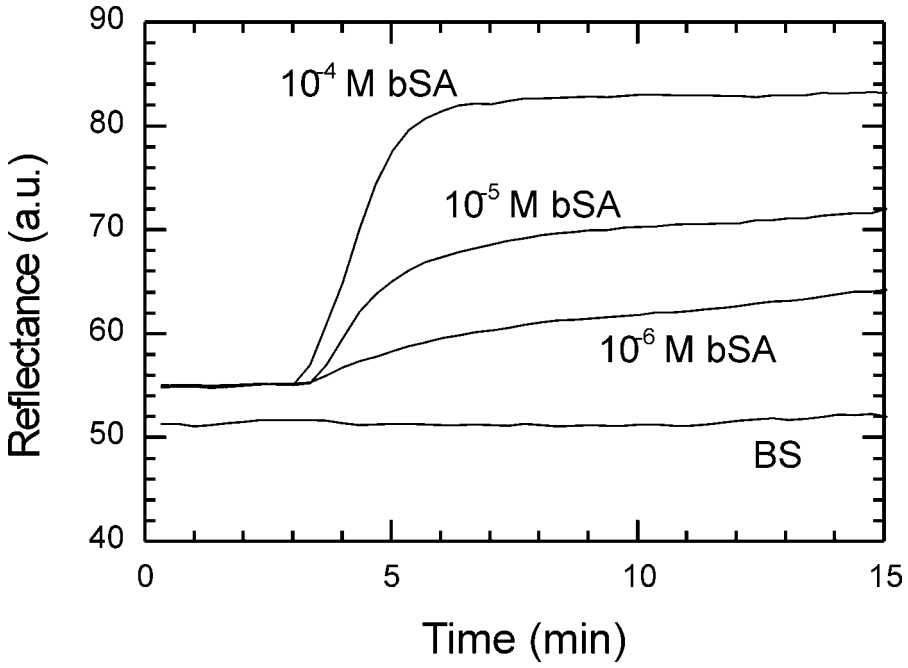

Fig. 2.11 Four channel adsorption experiment with bSA. The fourth channel was used as a reference channel.

Having demonstrated the feasibility of a multichannel sensor based on SPR, we proceeded with real immunosensor measurements. First, the four channels were coated with 10^{-6} M αhCG [7B] by adsorption to the gold surface (see Fig. 2.12). To avoid non-specific binding of the corresponding antigen to unoccupied sites at the surface, these were blocked by bSA (10^{-5} M). Three different concentrations of hCG were used for the immunoreaction ($2\cdot10^{-7}$ M, $4\cdot10^{-8}$ M and $8\cdot10^{-9}$ M). In the fourth channel $8\cdot10^{-9}$ M LH was added, which is known to have a high crossreactivity with αhCG because of its structural similarity with hCG. In the right part of Fig. 2.12 we see that the occurrence of the immunoreaction can be measured very well. The influence of the concentration on the kinetics of the immunoreaction is also apparent. The LH molecules indeed show a very high crossreactivity with the αhCG,

but the measurement also shows that a part of them are washed away when the solution is exchanged for the buffer solution.

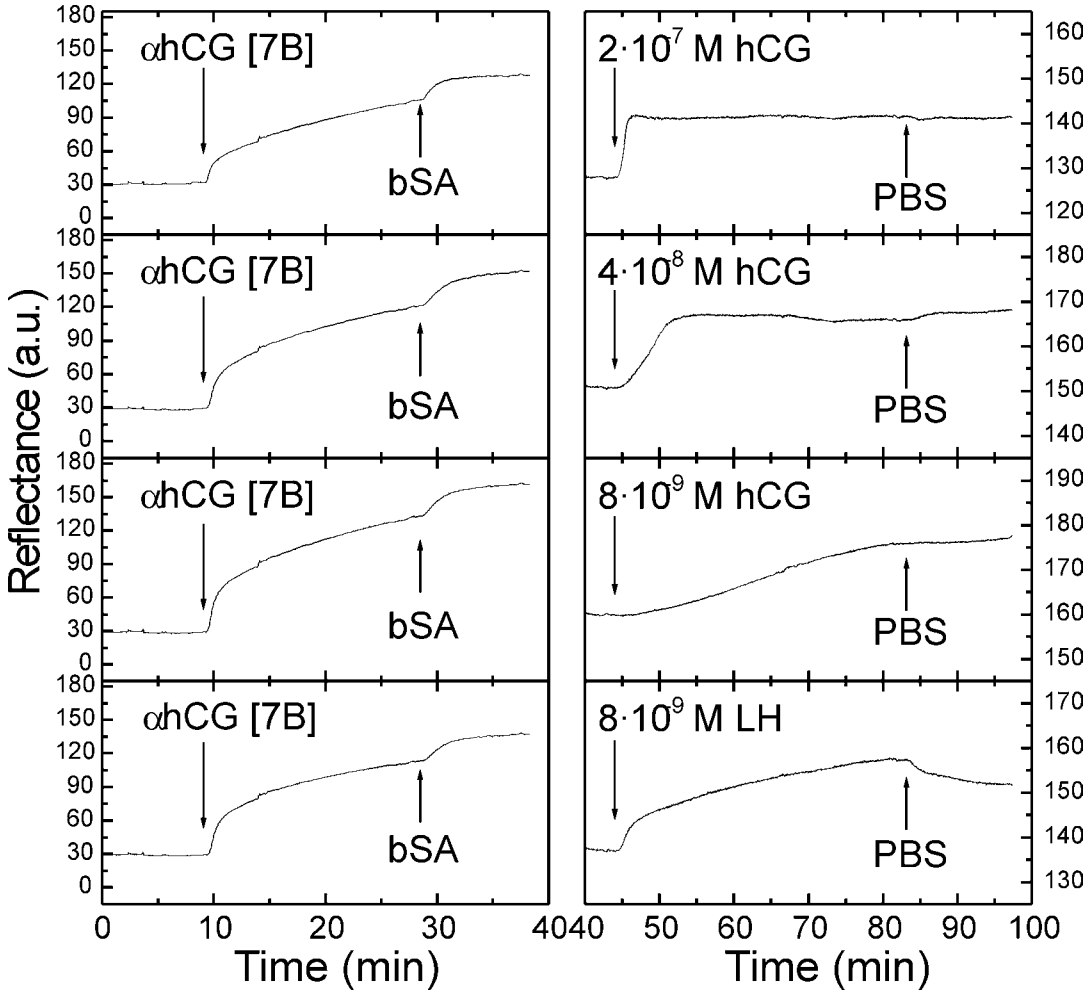

Fig. 2.12 Four channel immunoreaction experiment with the αhCG [7B] ($3 \cdot 10^{-7}$ M) in all channels. Immunoreactions were measured with three hCG concentrations and LH.

Two-dimensional array of sensor surfaces

Even more measurements can be performed simultaneously if a two-dimensional array of sensor surfaces is used for measurements. Figure 2.13 explains the approach that was chosen. In a first step the channels are coated with antibodies A,B,C,D. Then the multichannel flowcell is removed from the surface, turned 90° and pressed to the surface again. In a second step the antigens 1,2,3,4 are applied, flowing past the sensor areas with the different coatings. In this way all specific and crossreactivities can be measured simultaneously. Of course it is also possible to include duplo and reference measurements.

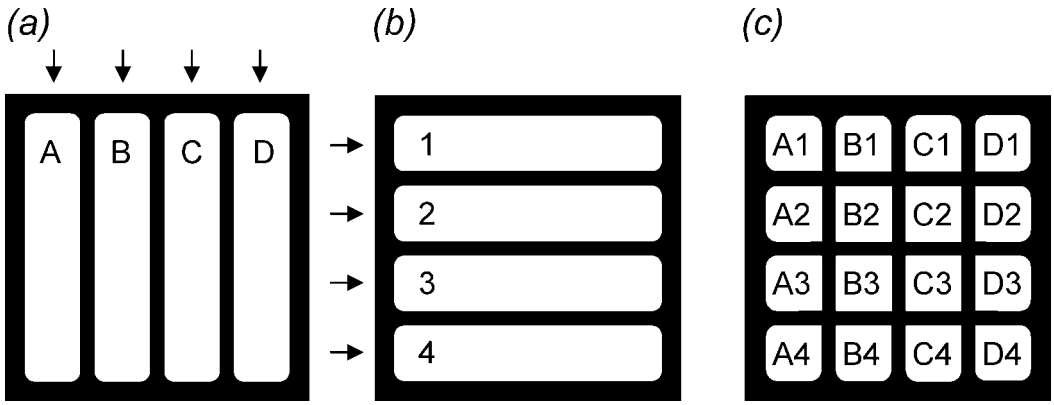

Fig. 2.13 Schematic explanation of how to use a four channel flowcell for sixteen independent measurements in a two-dimensional array.

Figure 2.14 shows the result of a two-dimensional multichannel measurement. The four channels were coated with $3 \cdot 10^{-7}$ M solutions of the αhCG monoclonals ([1C],[7B],[3A]) and αLH. After the blocking step with bSA the flowcell was turned 90°. In the second step the first two channels were used for a duplo measurement with $2 \cdot 10^{-7}$ M hCG. In the third channel 10^{-8} M LH was used, while the fourth channel was used as a reference channel. The A4 area was used to correct for disturbances due to ambient light *etc*. Rows 1 and 2 show similar results, except for the A1 area. The results in column B are very similar to those in Fig. 2.12. The sensor areas for the 2D measurement were four times smaller (about 1 mm^2) than those used during the immobilization of the antibodies, explaining the difference in the noise level. The drift in the measurements is probably mainly of a chemical nature, because mechanical drift would have the same effect on all sensor surfaces.

2.4.4 Conclusion

The feasibility of one and two-dimensional multichannel immuno-sensing was demonstrated. The problem of immobilization of a number of different analytes on the multisensor surface was tackled by using a multichannel flowcell. In Ref. 35 it was demonstrated that small quantities can also be deposited in specific locations on a sensor surface by using an ink jet nozzle. In our experiments the immobilization by adsorption as well as the immunoreaction were measured.

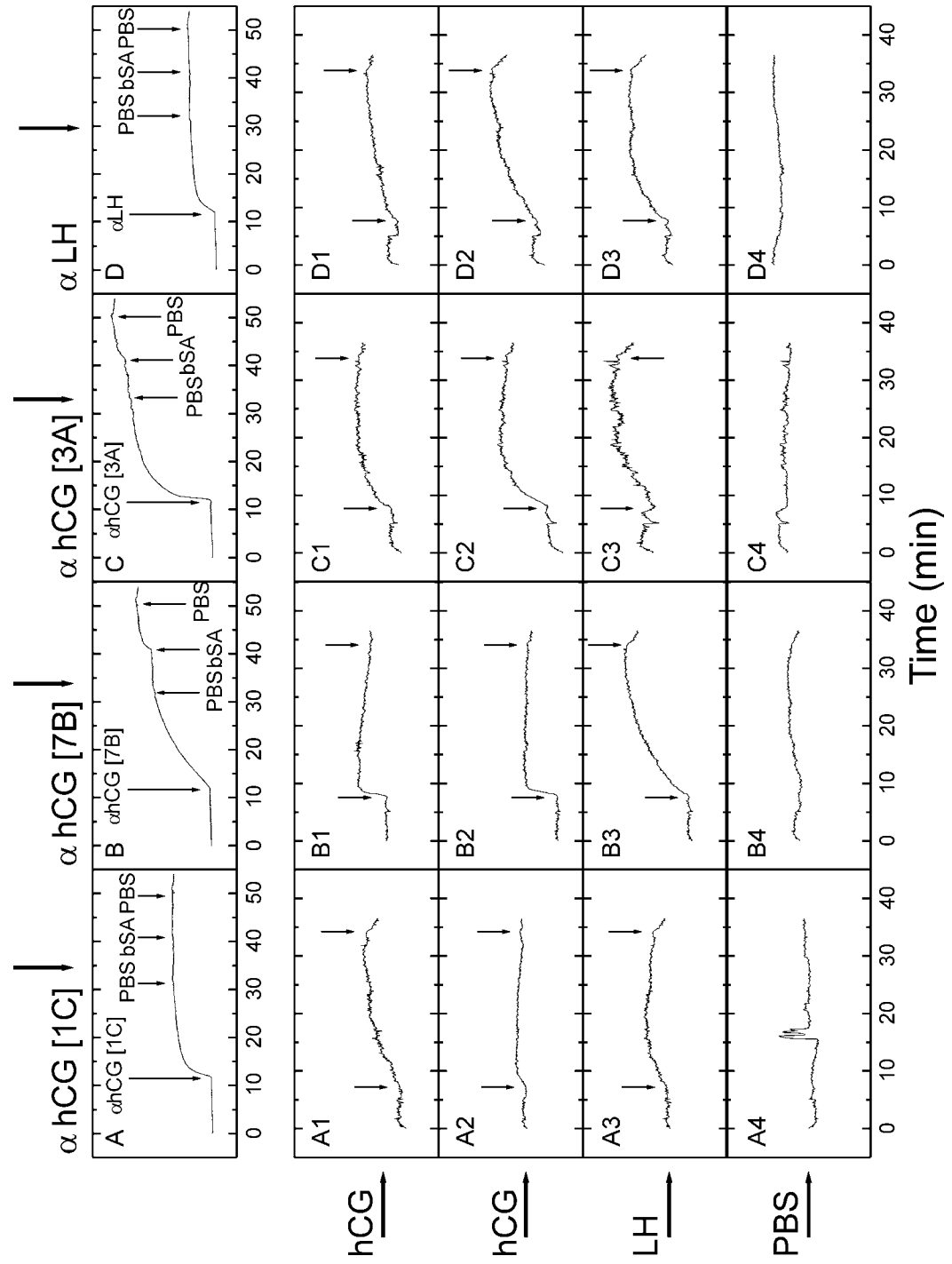

Fig. 2.14 Two-dimensional multichannel measurement. The antibody concentrations were $3 \cdot 10^{-7}$ M, and the concentrations of the antigens were $2 \cdot 10^{-7}$ M for the hCG, and 10^{-8} M for the LH.

2.5 References

(1) Lowe, C. R. *Phil. Trans. R. Soc. London* **1989**, B324, 487.
(2) Thompson, M.; Krull, U. J. *Anal. Chem.* **1991**, 63, 393.
(3) Tiefenthaler, K. *Biosensors Bioelectron*. **1993**, 8, xxxv.
(4) Heideman, R. G.; Kooyman, R. P. H.; Greve, J. *Sensors and Actuators B* **1993**, *10*, 209.
(5) Harris, R. D.; Wilkinson, J. S. *Sensors and Actuators B* **1995**, 29, 261.
(6) Cush, R.; Cronin, J. M.; Stewart, W. J.; Maule, C. H.; Molloy, J.; Goddard, N. J. *Biosensors Bioelectron*. **1993**, 8, 347.
(7) Buckle, P. E.; Davies, R. J.; Kinning, T.; Yeung, D.; Edwards, P. R.; Pollard-Knight, D.; Lowe, C. R. *Biosensors Bioelectron*. **1993**, 8, 355.
(8) Lukosz, W. *Biosensors Bioelectron*. **1991**, 6, 215.
(9) Knoll, W. *MRS Bulletin* **1991**, 16, 29.
(10) Liedberg, B.; Nylander, C.; Lundström, I. *Sensors and Actuators* **1983**, 4, 299.
(11) Nylander, C.; Liedberg, B.; Lind, T. *Sensors and Actuators* **1982/83**, 3, 79.
(12) Van Gent, J.; Lambeck, P. V.; Bakker, R. J.; Popma, Th. J. A.; Südholter, E. J. R; Reinhoudt, D. N. *Sensors and Actuators A* **1991**, 25-27, 449.
(13) Jory, M. J.; Cann, P. S.; Sambles, J. R. *J. Phys. D: Appl. Phys*. **1994**, 27, 169.
(14) Chadwick, B.; Gal, M. *Jpn. J. Appl. Phys*. **1993**, 32, 2716.
(15) Flanagan, M. T.; Pantell, R. H. *Electron. Lett*. **1984**, 20, 968.
(16) Daniels, P. B.; Deacon, J. K.; Eddowes, M. J.; Pedley, D. G. *Sensors and Actuators* **1988**, 15, 11.
(17) Pollard-Knight, D.; Hawkins, E.; Yeung, D.; Pashby, D. P.; Simpson, M.; McDougall, A.; Buckle, P.; Charles, S. A. *Ann. Biol. Clin*. **1990**, 48, 642.
(18) *Biosensors*; Cass, A. E. G., Ed.; The Practical Approach Series; Oxford University Press: Oxford, 1990.
(19) Severs, A. H.; Schasfoort, R. B. M. *Biosensors Bioelectron*. **1993**, 8, 365.
(20) Hickel, W.; Knoll, W. *Thin Solid Films* **1991**, 199, 367.
(21) Pollard, J. D.; Sambles J. R. *Optics Comm*. **1987**, 64, 529.
(22) Brink, G.; Sigl, H.; Sackmann, E. *Sensors and Actuators B* **1995**, 24-25, 756.
(23) Lenferink, A. T. M.; Kooyman, R. P. H.; Greve, J. *Sensors and Actuators B* **1991**, 3, 261.
(24) Ivarsson, B.; Jönsson, U.; Karlsson, R.; Liedberg, B.; Renck, B.; Roos, H.; Sjödin, H.; Stenberg, E.; Ståhlberg, R.; Urbaniczky, C.; Lundström, I. In *Proc. 3rd Int. Meet. on Chemical Sensors, Sept. 24-26*, 1990, pp 157.
(25) Jorgenson, R. C.; Jung, C.; Yee, S. S.; Burgess, L. W. *Sensors and Actuators B* **1993**, 13-14, 721.
(26) Dougherty, G. *Meas. Sci. Technol*. **1993**, 4, 697.
(27) Matsubara, K.; Kawata, S.; Minami, S. *Appl. Opt*. **1988**, 27, 1160.
(28) Löfås, S.; Malmqvist, M.; Rönnberg, I.; Stenberg, E.; Liedberg, B.; Lundström, I. *Sensors and Actuators B* **1991**, 5, 79.
(29) Zhang, L.-M.; Uttamchandani, D. *Electron. Lett.* **1988**, 24, 1469.
(30) Katerkamp, A.; Bolsmann, P.; Niggemann, M.; Pellmann, M.; Cammann, K. *Mikrochim. Acta* **1995**, 119, 63.
(31) Jory, M. J.; Bradberry, G. W.; Cann, P. S.; Sambles, J. R. *Meas. Sci. Technol.* **1995**, 6, 1193.

(32) Gass, P. A.; Sambles, J. R. **1992** *Methods of and apparatus for measuring using acousto-optic devices*, UK patent GB2254693B.
(33) de Bruijn, H. E.; Kooyman, R. P. H.; Greve, J. *Appl. Opt.* **1990**, 29, 1974.
(34) Weast, R. C., Ed.; *Handbook of Chemistry and Physics*, 56th ed.; CRC Press: Cleveland, 1975.
(35) Kimura, J.; Kawana, Y.; Kuriyama, T. *Biosensors* **1988**, 4, 41.

CHAPTER THREE

SURFACE PLASMON PROPAGATION NEAR AN INDEX STEP

Generally, the application of Fresnel theory to the description of reflectometric measurements is straightforward and gives accurate results when the conditions mentioned in the first chapter are satisfied. In this chapter we will study propagation effects of surface plasmons on the SPM image of an area around the edge of a cover layer. Far from this index step Fresnel theory still applies, but at distances smaller than the propagation length of SPs (typically micrometers) it cannot be used anymore. Because Fresnel theory assumes that the layer system consists of infinite layers it can only provide the reflectance far from the step as a boundary condition. We will present a phenomenological model (based on that presented in Refs. 1,2) that describes the effect of plasmon propagation on the observed reflectance near an index step, and study this effect as a function of the wavelength. Silver layers were first characterized by fitting experimental SPR angular reflectance curves. Then the model was used to predict the resulting reflectance profile when an index step on the metal layer was imaged with a surface plasmon microscope. Measurements and calculations were performed for wavelengths ranging from 560 to 660 nm for a 50 nm silver layer with 30 nm thick SiO_2 pattern on top. Theoretical and experimental results will be compared.

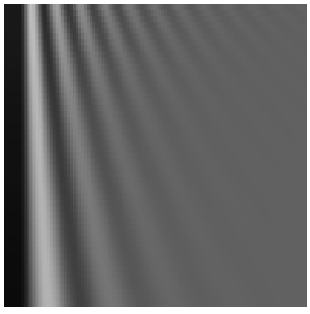

3.1 Theory

In the following, κ is the *x*-component of the wave vector, and may be complex ($\kappa = \kappa' + i\kappa''$). When a resonant plasmon with wave vector κ_0 propagates along *x* from an uncovered area into a covered area, a decaying plasmon (containing an imaginary component) with wave vector κ_1 results (see Fig. 3.1).[3] Here κ_1 is the wave vector for resonant excitation of the covered area. Furthermore, the external light source with wave vector κ_0 excites a non-resonant surface plasmon with wave vector κ_0, if κ_0 is within the resonance width of the SPR curve in the covered area. The change of the surface plasmon electric field amplitude is

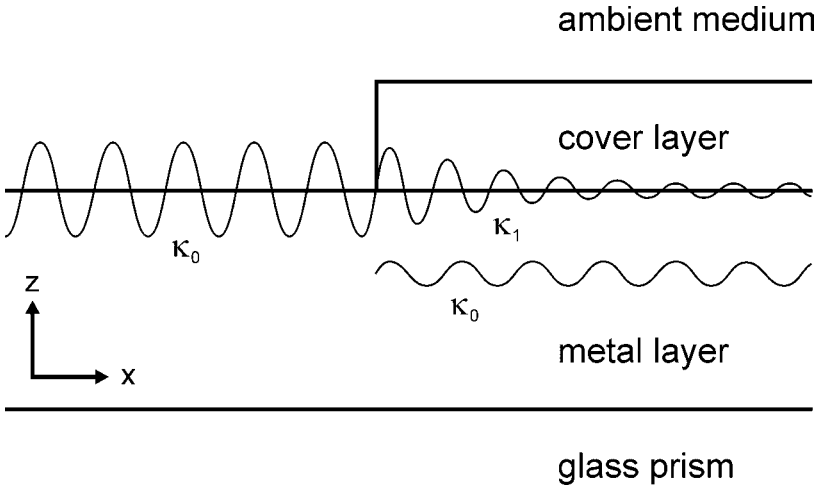

Fig. 3.1 Schematic representation of a surface plasmon with wave vector κ_0 propagating along a metal-air interface into a cover layer, where an exponentially decaying κ_1 plasmon results. The non-resonantly excited surface plasmon with wave vector κ_0 is indicated separately.

governed by the imaginary part of its wave vector. The constants E_1 and E_2 are the resonant and the non-resonant plasmon amplitude, respectively. Leaving out the time dependence, the plasmon electric field at the interface is[1,2]

$$E_{pl}(x) = (E_1 - E_2)e^{i(\kappa_1' + i\kappa_1'')x} + E_2 e^{i\kappa_0' x}, \qquad (3.1)$$

for $x \geq 0$, with $x=0$ at the index step. We improved this model to predict the reflectance near the indexstep. Far from the index step, the assumptions of plane waves and infinite layers are valid, and if the boundary conditions are to be fulfilled the reflectance at a large distance from the step should coincide with Fresnel values. By imposing these conditions all parameters of the model are fixed.

In Refs. 1 and 2 it is assumed that the non-resonant contribution to E_{pl} is constant and starting at x=0. What is missing in this model is the fact that the plasmon electric field interferes with the incoming field from the light source. Because of this omission the model can give incorrect results, with a higher reflectance at resonance than off resonance. Therefore, for the total electric field reaching the detector an extra term should be introduced to account for the low reflectance resulting from resonant plasmon excitation, due to destructive interference:[4]

$$E_{tot}(x) = (E_1 - E_2)e^{i(\kappa_1' + i\kappa_1'')x} + E_2 e^{i\kappa_0' x} - E_3 e^{i\kappa_0' x}, \qquad (3.2)$$

where E_3 is the amplitude of the incoming field. With A=E_1-E_2 and B=E_2-E_3, the resulting intensity can be written as

$$I_{tot}(x) = \left|E_{tot}(x)\right|^2 = B^2 + A^2 e^{-2\kappa_1'' x} + 2ABe^{-\kappa_1'' x}\cos(\kappa_1' - \kappa_0')x \qquad (3.3)$$

For x=-∞ (or x≤0) and x=+∞, the intensity equals $(E_1$-$E_3)^2$ and $(E_2$-$E_3)^2$, respectively. We can solve these constants putting E_3 equal to 1 (E_3>E_1>E_2>0), because then I_{tot}(-∞) and I_{tot}(+∞) equal the macroscopic reflectance for uncovered and covered areas that can be calculated with Fresnel theory. Note that there are no free parameters to fit measurements.

When a non-resonant plasmon exits a covered area and becomes resonant the total electric field and intensity may be written in a similar way:

$$E_{tot}(x) = E_2 e^{i\kappa_0' x} + (E_1 - E_2)(1 - e^{-\kappa_0'' x})e^{i\kappa_0' x} - E_3 e^{i\kappa_0' x}, \qquad (3.4)$$

and

$$I_{tot}(x) = \left[B + A(1 - e^{-\kappa_0'' x}) \right]^2, \qquad (3.5)$$

where the same definitions are used for the constants. The plasmon wave vectors were calculated using the second-order theoretical approximation of the dispersion relation of surface plasmons given by Pockrand[5] and depend on the properties of the metal layer and the cover layer.

3.2 Experimental section

3.2.1 Setup

Two cavity-dumped dye lasers (3.8 MHz, Coherent 700) synchronously pumped by a mode-locked Nd:YLF laser (Antares 76-YLF, Coherent) served as a light source covering the wavelength range

from 560 to 660 nm. The polarization could be modulated between *p* and *s* polarization electronically, using a Pockels cell (PC 100/4; Electro Optic Developments, Ltd., Basildon, England). A rotation table (MicroControle UR80PP; angular increments: 1 mdeg.) was used for computer controlled reflectance scans that were measured with a photodiode.

The experimental setup for the surface-plasmon microscope will be described in detail in the next chapter. It images the attenuated total reflectance in the Kretschmann configuration, and uses *p* and *s* polarized light to correct for inhomogeneities in the expanded incoming laser beam. A 7× (NA 0.19) objective was used to image the light on a video camera (VCM 3250; Philips) which has an output that is linear in light intensity.

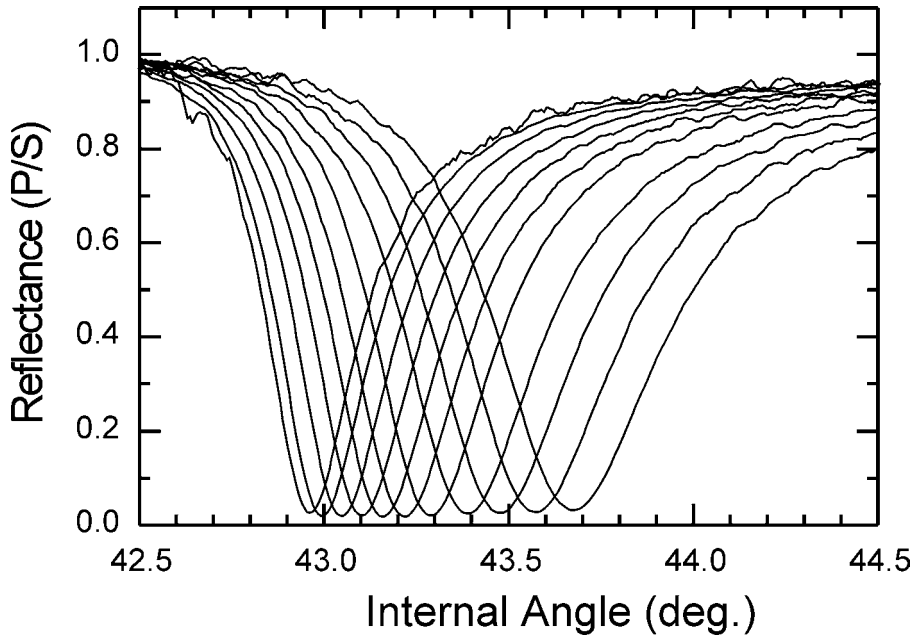

Fig. 3.2 Ratio of the reflectance for *p* and *s* polarized light as a function of the internal incident angle and wavelength (560-660 nm) for a silver layer. Table 3.I shows the results from fitting these measurements.

3.2.2 Sample preparation

Microscope glass slides were used as substrates on which a 50 nm silver layer was evaporated (1 nm/s at 10^{-6} mbar). After the evaporation, a photoresist layer was spun on the substrate and a pattern was made photolithographically. A 30 nm thick SiO_2 layer was sputtered (0.1 nm/s at 10^{-2} mbar Ar) over the bare and covered areas of the silver layer. After the removal of the photoresist using an ultrasonic acetone bath, a SiO_2 pattern on the silver resulted. Substrates were stored in a nitrogen

atmosphere. They were attached to the prism (BK7 glass, 45 deg.) using a matching oil.

3.3 Results and discussion

3.3.1 Substrate characterization

All measurements were carried out for wavelengths ranging from 560 to 660 nm in steps of 10 nm. First the SPR reflectance of the bare silver layer was measured as a function of the angle of incidence. The low frequency part of the laser noise was effectively suppressed by measuring

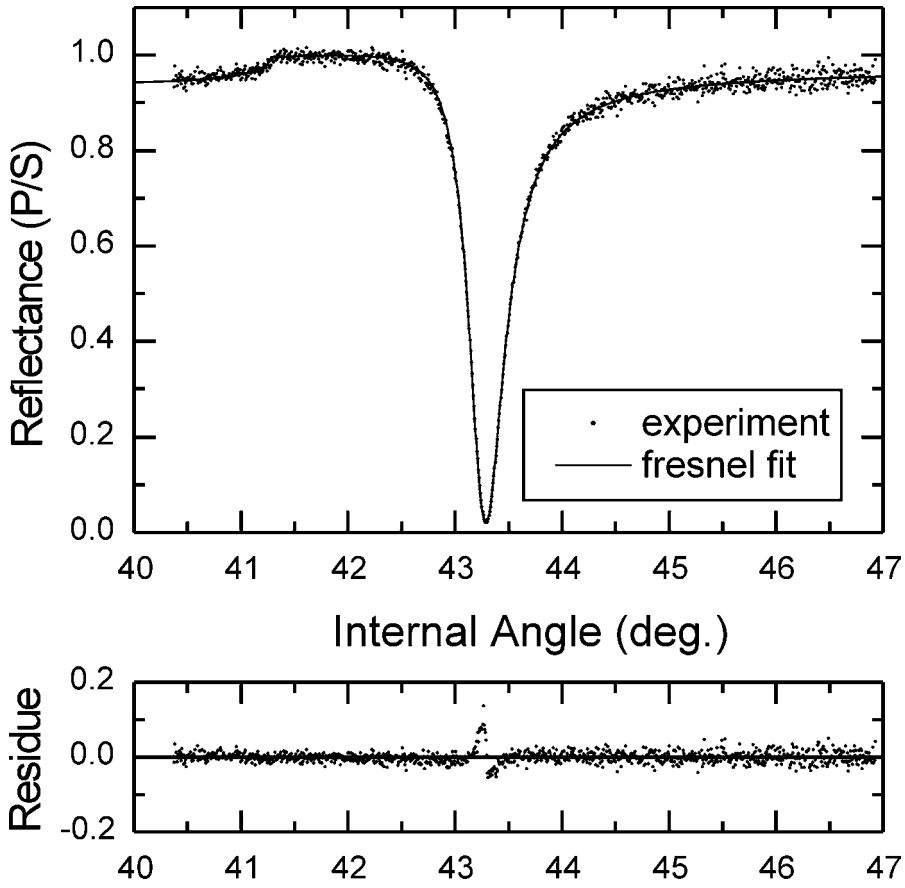

Fig. 3.3 Ratio of the reflectance for *p* and *s* polarized light as a function of the internal incident angle for wavelength λ=600 nm, together with Fresnel fit (ε=-13.95+*i*0.554 and *d*=50.2 nm). The residue was calculated as the relative difference of theoretical and experimental values.

the reflectance switching the polarization between *p* and *s*, while integrating both signals. The ratio of the *p* and *s* reflectance as a function of the angle of incidence and the wavelength is displayed in Fig. 3.2.

These normalized values can be directly compared to Fresnel calculations, taking into account the different transmission of the prism entrance and exit surfaces for different polarizations. The ratio of the transmissions of the prism for *p* and *s* polarized light is given by

$$\frac{T_p}{T_s} = \left(\frac{n_1 \cos\theta_1 + n_2 \cos\theta_2}{n_1 \cos\theta_2 + n_2 \cos\theta_1} \right)^4 , \qquad (3.6)$$

where θ_1 and θ_2 are the external and internal angles of the propagating light beam with respect to the normal of the entrance and exit surface, and n_1 and n_2 are the refractive index of the ambient medium and the prism, respectively. Fresnel formulae were used to fit the measured reflectance curves by varying the real and imaginary part of the dielectric constant ε and the thickness *d* of the silver layer. It has been demonstrated before,[5-7] that the reflectance curves depend on these three parameters in such a way that they can be determined separately. A computer program that was written (based on differential correction and the least squares criterion) needed less than 10 iterations to converge to the values presented in Table 3.I.

Table 3.I. Dielectric constant and thickness of the silver layer as a function of wavelength.

λ (nm)	ε_r	ε_i	*d* (nm)
560	-11.43	0.480	50.36
570	-11.97	0.502	50.41
580	-12.52	0.519	50.42
590	-13.08	0.536	50.49
600	-13.95	0.554	50.21
610	-14.53	0.578	50.23
620	-15.06	0.594	50.34
630	-15.62	0.602	50.30
640	-16.19	0.614	50.35
650	-16.80	0.629	50.22
660	-17.15	0.608	50.27

Of course *d* should not depend on the wavelength and indeed, for the independent measurements at different wavelengths the same value for the layer thickness was found with a high accuracy (50.3±0.1 nm). The excellent agreement of Fresnel calculation and experimental data can also be seen in Fig. 3.3, where one of the measurements is shown together with the calculated values as an example

The thickness of the SiO_2 pattern on top of the silver layer was checked with a surface profiler (Dektak) and was indeed about 30 nm (See Fig. 3.4). The steepness of the edge was obscured by the tip convolution, but with the lift-off method (as described in Section 3.2.2) the edge is expected to be narrower than one micron, which is sufficient for this study.

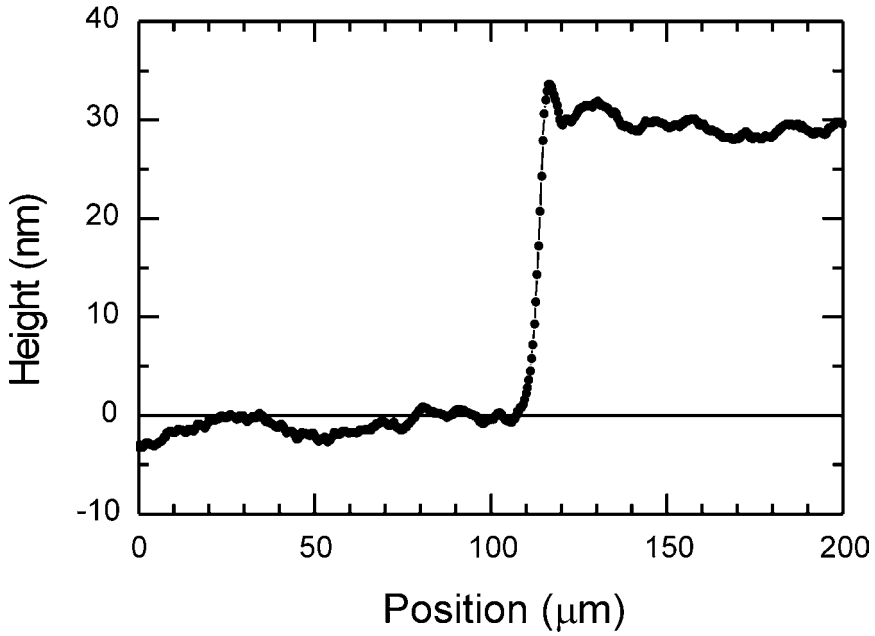

Fig. 3.4 Profile of the SiO_2 index step, measured with a surface profiler.

3.3.2 Reflectance near the index step

With the silver layer parameters (ε_r,ε_i,*d*) known, the reflectance profile near the index step can be calculated using the model that was presented in Section 3.1. The parameters in Eq. 3.3 can be derived from Fresnel calculations using ε and *d*. The constants *A* and *B* follow from the boundary condition that the reflectance far from the index step [$I_{tot}(-\infty)$ and $I_{tot}(+\infty)$] should equal that given by Fresnel theory. The real part of the wave vectors κ_1 and κ_0 (corresponding to resonant SP excitation of covered and uncovered areas respectively) can be determined from the position of the minimum in calculated angular reflectance curves. Finally,

the imaginary part of the wave vectors κ_1 and κ_0 can be determined from the width of the SPR dip or from Pockrand's second order approximation.[5]

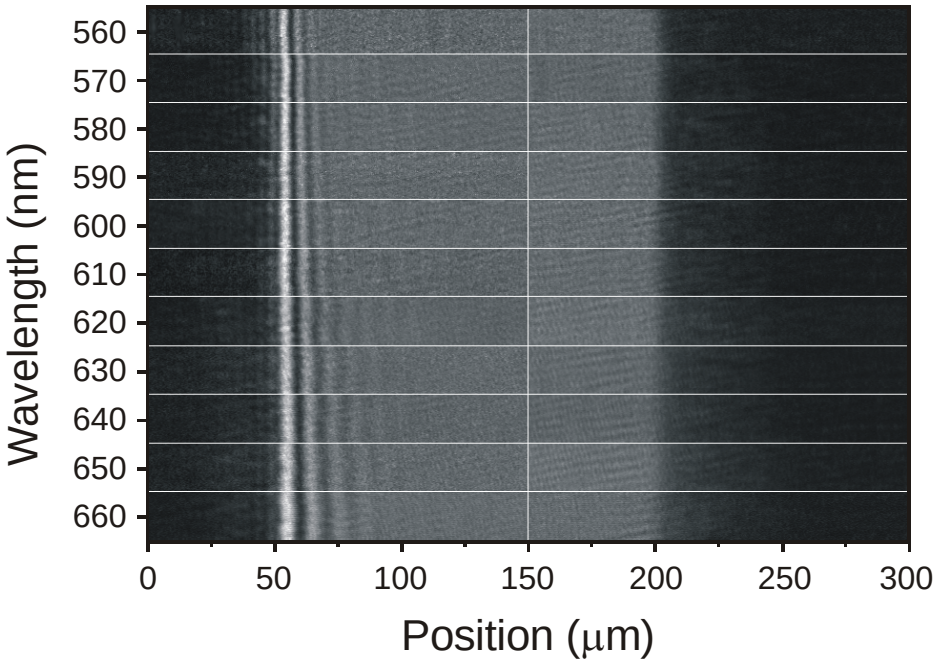

Fig. 3.5 Composition of all SPM images of the index step, with the resonant plasmon entering (left, at 50 μm) and leaving the cover layer (right, at 200 μm).

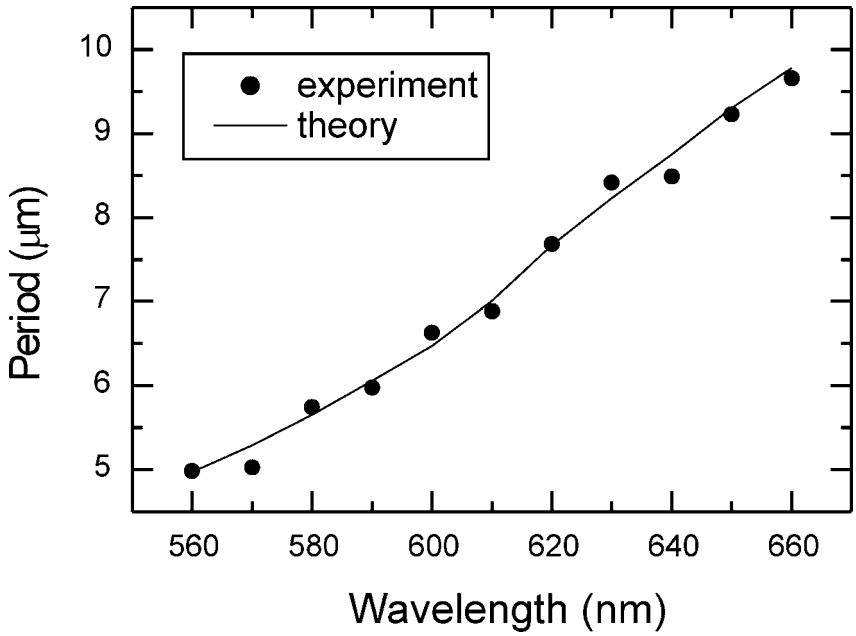

Fig. 3.6 Periodicity *p* of the profiles of the images in Fig. 3.4 as a function of wavelength together with the calculated values for *d*=27.9 nm and *n* equal to that of BK7 glass.

Experimentally, the reflectance profiles were determined from surface plasmon microscopy images of the index step. The index step was imaged with both *p* and *s* polarized light to correct for inhomogeneities in the incoming beam by dividing the images obtained with the different polarizations. In Fig. 3.5 the images resulting from resonant plasmons entering the SiO_2 covered area and leaving it again are shown for 11 different wavelengths, with the SPs propagating from left to right. Squares of known size (50 μm) were imaged as well (results not shown), to determine the lateral scale of the images. The reflectance profiles in the direction perpendicular to the index step were determined from the digitized SPM images averaging along the index step.

From these profiles, the periodicity was determined as a function of the wavelength. Equation 3.3 shows that this periodicity *p* is given by

$$p = \frac{2\pi}{\kappa_1' - \kappa_0'}. \tag{3.7}$$

In Fig. 3.6 these values are displayed together with theoretical values for a 27.9 nm SiO_2 layer with the refractive index assumed to be equal to that of BK7 glass. As this value for *d* is more accurate than the one determined with the surface profiler (and lies within the experimental error of that value) it was used for the calculation of the reflectance profiles.

These are given in Fig. 3.7, together with the experimental values. The measured and calculated profiles were normalized by putting the macroscopic values for the reflectance far from the index step to either zero (at resonance) or one (off resonance). The correspondence between experiment and theory is quite good, qualitatively as well as quantitatively. Some fringes to the left of the index step seem to be caused by a reflection that is not accounted for by the model. Their dependence on the wavelength is different from that of the fringes on the right of the index step.

3.3.3 Conclusion

We have developed a model that describes the reflectance profile near an index step. A silver layer was characterized by fitting measured SPR reflectance curves, and the thickness of the cover layer was measured with a surface profiler. Experimental and theoretical values for the reflectance profile as a function of the wavelength were compared and found to agree quite well. In the next chapter this model will be used to determine which wavelength and metal layer are most suitable for surface plasmon microscopy with a high lateral and thickness resolution.

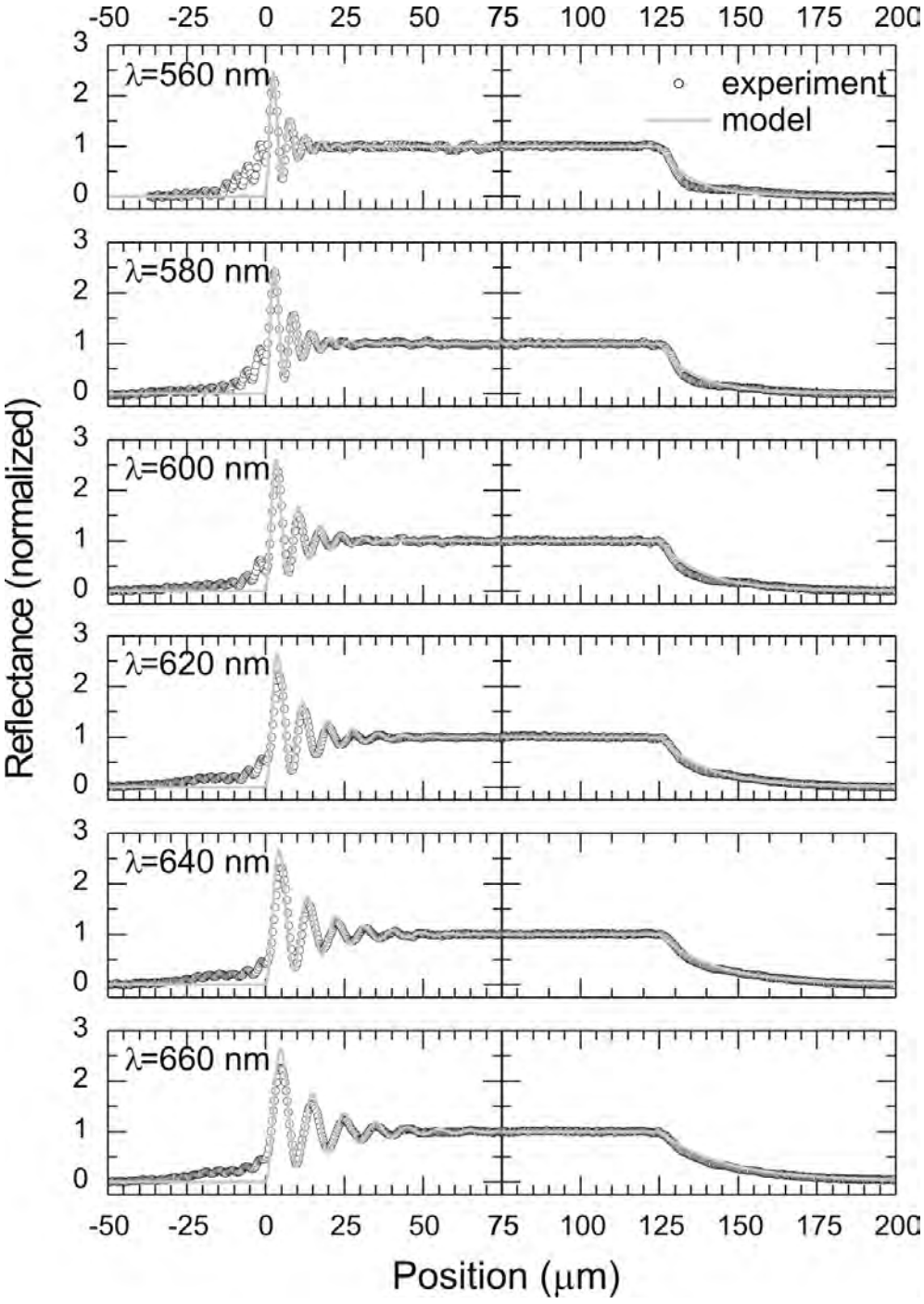

Fig. 3.7 Calculated and measured reflectance profiles as determined from the images in Fig. 3.4. The reflectance values at resonance and off resonance were normalized to zero and one, respectively.

3.4 References

(1) Rothenhäusler, B.; Knoll, W. *J. Opt. Soc. Am. B* **1988**, *5*, 1401.
(2) Rothenhäusler, B.; Knoll, W. *Appl. Phys. Lett.* **1988**, *52*, 1554.
(3) Leskova, T. A.; Gapotchenko, N. I. *Solid State Commun.* **1985**, *53*, 351.
(4) Raether, H. *Surface Plasmons on Smooth and Rough Surfaces and on Gratings*; Springer: Berlin, 1988.
(5) Pockrand, I. *Surf. Sci.* **1978**, *72*, 577.
(6) Chen, W. P.; Chen, J. M. *J. Opt. Soc. Am.* **1981**, *71*, 189.
(7) Watson, T. J.; Sambles, J. R. *Philosophical Magazine B* **1992**, *65*, 1141.

CHAPTER FOUR

SPM SETUP AND METHODS

In this chapter we demonstrate how to obtain the ultimate lateral resolution in surface plasmon microscopy (SPM) (diffraction limited by the objective). Surface plasmon decay lengths are determined theoretically and experimentally, for wavelengths ranging from 531 to 676 nm, and are in good agreement. Using these values we can determine for each particular situation which wavelength should be used to obtain an optimal lateral resolution, *i.e.*, where the plasmon decay length does not limit the resolution anymore. However, there is a trade-off between thickness resolution and lateral resolution in SPM. Because of the non-optimal thickness resolution, we use several techniques to enhance the image acquisition and processing. Without these techniques the use of short wavelengths results in images where the contrast is very low. In an example given, structures in a 2.5 nm SiO_2 layer on a gold layer could be imaged with a lateral resolution of 2 μm, and local reflectance curves were measured to determine the layer thickness with a resolution better than 0.1 nm (based on the angular shift of the curve). The SPM image is compared with an atomic force microscopy image of the same object.

4.1 Introduction: Lateral and thickness resolution in SPM

It has previously been shown that with SPM a thickness resolution down to a few tenths of a nanometer can be obtained.[1,2] However, the lateral resolution is limited by the decay length L_x of surface plasmons. This quantity is defined as the distance along the surface for which the attenuation of the plasmon field intensity is $1/e$ (see Chapter 1, Eq. 1.38). Here we will be concerned with the problem of how to obtain optimum lateral resolution while retaining sufficient thickness resolution. Although it was mentioned in the literature that it should be possible to improve the lateral resolution by choosing an appropriate wavelength and metal layer,[2] to our knowledge no detailed study of this problem has been conducted previously.

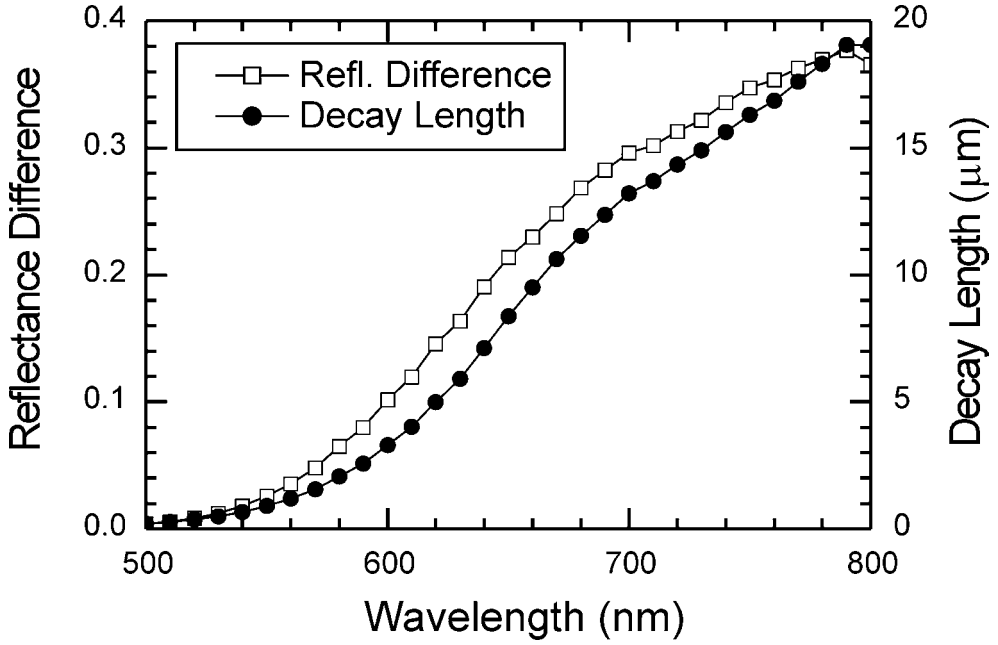

Fig. 4.1 Reflectance difference for gold covered with 2.5 nm SiO_2 and bare gold for the resonance angle of the bare gold (circles), and surface plasmon decay lengths for gold (squares) as a function of wavelength. Dielectric data were obtained from Ref. 6.

The problem can be illustrated by regarding a situation where a 2.5 nm SiO_2 layer partly covers a 45 nm gold layer, and where the angle of incidence is chosen such that surface plasmons in the bare gold are resonantly excited. When the contrast, defined as the difference in reflectance of both regions, is calculated as a function of wavelength, a relation as depicted in Fig. 4.1 is found. In the same figure the wavelength dependent L_x values are given, using Eq. 1.38 and the second-

order approximation for Im(κ_x) by Pockrand.[3] It is seen that a smaller decay length is accompanied by a smaller reflectance difference. From the figure it can be determined how high the lateral resolution will be if the accompanying reflectance difference is sufficient for SPM imaging.

The resonance halfwidth for silver is appreciably smaller than that for gold. This leads to a higher dependence of the reflectance on the thickness, and thus a higher contrast and thickness resolution. However, the wavelength-dependent decay lengths are significantly larger than those in gold, due to the relatively low surface plasmon damping. Therefore, in view of the larger losses in gold, this material seems preferable for high-resolution SPM, and in the following we will restrict ourselves to this metal.

Now, if we can realize and observe decay lengths near the diffraction limit of the objectives used, a wavelength can be chosen for a SPM experiment in which the plasmon decay length will be just below the resolution of the microscope objective. The problem of how to obtain a *higher lateral resolution* is then converted to how to make sure that the *lower contrast* is sufficient for imaging.

In the next sections, a plasmon-carrying 45 nm gold layer is characterized by SPR measurements. From the data the expected plasmon propagation is calculated for various wavelengths. To verify these values, decay lengths that are much smaller than in experiments conducted previously[4] are observed microscopically. The optimal wavelength for imaging with a high lateral resolution is chosen, depending on the microscope objective and the imaged cover layer. Several techniques to improve the image acquisition and processing are applied to compensate for the loss in contrast and to correct for other image degrading effects. SPM images of a 2.5 nm SiO_2 layer are compared with an atomic force microscopy (AFM) image of this layer.

4.2 Experimental section

4.2.1 Setup

The SPM setup used is essentially the Kretschmann (ATR) configuration, and is schematically drawn in Fig. 4.2. A rotation table was used for easy and accurate angular adjustment (angular increments: 0.01°). Electronic switching between *p* and *s* polarization was done with a Pockels cell (PC 100/4; Electro Optic Developments Ltd., Basildon, England). The Pockels cell was used for normalization and correction of background effects. A HeNe laser and an Ar/Kr laser, which allows

illumination with a number of lines in the visible spectrum (Innova 70; Coherent Inc., Palo Alto, CA), serve as light sources. Wavelengths ranging from 531 nm to 676 nm were used. The intensity profile of the reflected light beam was recorded with a microscope consisting of an objective and a charge-coupled device (CCD) camera (VCM 3250; Philips). The output of the camera is linear in light intensity. Depending on the light intensity and magnification needed, a 40× [extra long working distance; numerical aperture (NA) 0.49] or a 7× (NA 0.19) objective was used.

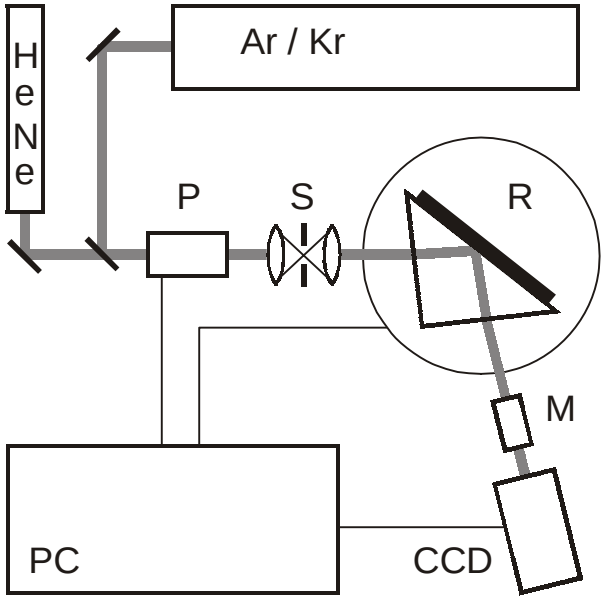

Fig. 4.2 Schematic representation of the setup used for the microscopical measurements. The Pockels cell, rotation table, and camera are interfaced to a computer; manual control is also possible. P: Pockels cell; S: spatial filter; R: rotation table; M: microscope objective.

Pockels cell, rotation table, and CCD videocamera can be controlled both manually and by computer. Video images (512×512 picture elements) are processed and stored in a computer (486 PC) using a frame grabber card (VisionPlus AT OFG; Imaging Technology, Inc., Woburn, MA). The computer-controlled features make the setup particularly well suited for the experimental methods described in the next sections.

4.2.2 Improvement of the image quality

There are a number of factors that determine the eventual quality of an SPM image apart from the diffraction limit of the microscope objective:

(i) Plasmon decay length. We have seen that this influence can be avoided almost completely by using an appropriate wavelength, which, however, results in a lower contrast.

(iii) Quantization during image acquisition. To improve the image acquisition we implemented an option to add a number of images using a dynamic range of 2^{16}. The large dynamic range is important, because with a low contrast one of the first steps is to increase the contrast digitally. With the normal dynamic range of 2^8 of the separate images, quantization levels become visible upon high amplification. The dynamic range of the eventually presented image is 2^8.

(iii) Noise caused by low light levels. Integrating n images also means averaging, and the signal to noise ratio consequently improves with a factor $n^{½}$. Although a maximum number of 256 images can be integrated, choosing n=50 proved to be more than sufficient to remove any visible noise due to low light levels in all cases mentioned in this chapter. Increasing the laser power is another possibility but this option is of limited use in view of the resulting destructive effects on the sample. After integration, the noise due to the CCD camera can be neglected.

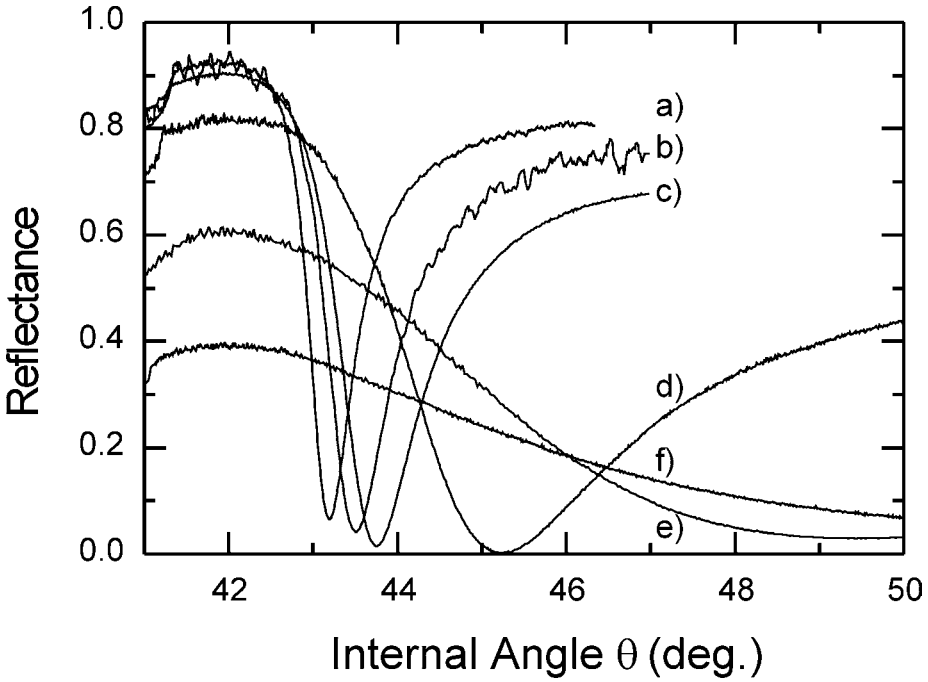

Fig. 4.3 Reflectance curves for a bare gold layer, measured with different wavelengths: (a) 676.4 nm; (b) 647.1 nm; (c) 632.8 nm; (d) 568.2 nm; (e) 514.5 nm; (f) 488.0 nm.

(iv) Lateral inhomogeneities in the incoming laser beam intensity profile. At the moment, this is usually the limiting factor for the lateral resolution of our SPM images. We have two ways of suppressing this 'noise.' The first is using a spatial filter to create a more homogeneous

incoming laser beam. This, however, does not work for inhomogeneities created by unwanted reflections at prism and objective surfaces. Therefore, another technique is used involving digital image processing. Using the Pockels cell, two images are acquired using *p* and *s* polarized light, respectively. The image with *p* polarization contains the SPM image together with the contrast generated by spatial fluctuations, while the image obtained with *s* polarized light only contains the same unwanted fluctuations. Because the camera output is linear in light intensity, the two images can be divided (after a suitable linear transformation) to suppress the errors in the image.

An important point to be made is that when contrast is increased digitally, it should be a linear operation. This means that all resulting gray values should be within the range of the displayed image. If this condition is not satisfied, a lot of pixels will be set to black or white, and while a higher resolution is suggested, in fact information is lost.

4.2.3 Sample preparation

The substrates used are small microscope cover slips that were attached to the prism (BK7 glass) using a matching oil. A 45 nm gold layer was evaporated on top of this substrate (1 nm/s at 10^{-6} mbar). After the evaporation, a SiO_2 layer with a thickness of a few nanometers was sputtered on top of the gold (0.1 nm/s at 10^{-2} mbar Ar). Photolithography and wet etching techniques were used to make a high-resolution test pattern with sharp edges (transition region < 1 μm) in this SiO_2 layer.

4.3 Results

4.3.1 Characterization of the gold layer

The plasmon decay length is very dependent on the imaginary part of the dielectric function of the gold, which depends on the manufacturing process and surface roughness as well. Therefore, we have experimentally determined the dielectric function instead of using literature values. To characterize the metal layer on our substrate, the SPR reflectance as a function of the angle of incidence in an ATR experiment was measured and fitted for a number of wavelengths in the visible range. The measured reflectance curves for a bare gold layer of 44 nm are displayed in Fig. 4.3.

When the critical angles were calculated for the different wavelengths and compared to the experimental values, a systematic shift of

0.08° in the angular measurements was found. The critical angle is dependent on the prism refractive index only and can easily be included in an angular scan. Therefore, it seems to be better to use this angle as a reference angle instead of the angle found using perpendicular reflection, which by definition is the zero external angle. Four parameters were fitted: the layer thickness *d*, the real and imaginary part of the dielectric constant ε, and a normalization constant relating the measured reflectance to the absolute reflection coefficient. Fresnel theory was used for the fitting, which resulted in excellent fits. Dispersions of the different media and the reflection losses at the prism sides were included in the calculations. As an example one of these fits is given in Fig. 4.4.

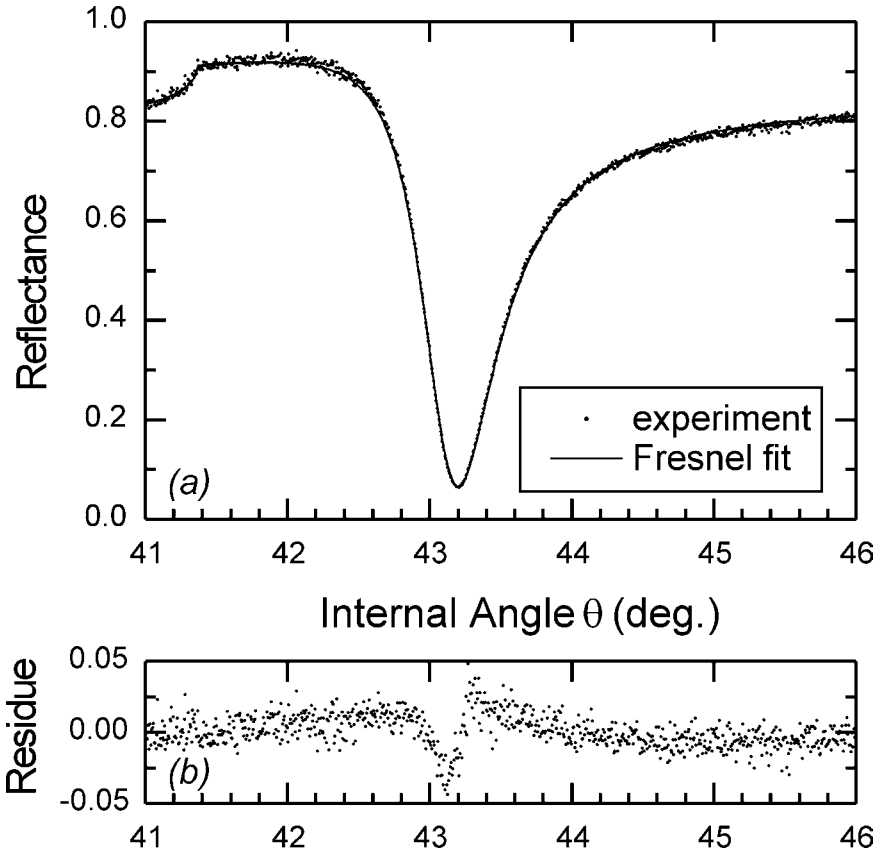

Fig. 4.4 ***(a)*** Fitted plasmon reflectance curve for a 44 nm gold layer at λ=676.4 nm. The points result from the reflectance scan, the solid line represents the fitted values using Fresnel theory. ***(b)*** The relative difference between measurement and fit.

The thickness of the gold layer that resulted from the fitting was 43.6 nm. The accuracy for the fitted thickness, as determined by the spread in independent measurements, was rather high: for the three longest wavelengths, the thickness values found reproduced within 0.1 nm. For the shortest wavelengths the spread in the determined thickness values was

about 1 nm, which can be explained by the less pronounced dip in the reflectance curves. From the residue it is seen that there exists a small systematic error. This is hardly of influence on the quoted parameters. Measurements with a surface profiler confirmed a thickness in between 43 and 44 nm. The resulting values for the complex dielectric function of the gold were found to be between dielectric functions found by others,[5-7] although these literature values show some spread. The results of the fitting and the calculated decay lengths are presented in Table 4.I.

Table 4.I. Fit results for a gold layer of 44 nm and derived theoretical decay lengths.

λ (nm)	ε_r	ε_i	d (nm)	L_x (μm)
488.0	-1.63	4.20	42.9	0.1
514.5	-3.77	2.61	42.3	0.3
530.9	-4.66[a]	2.47[a]	...	0.5
568.2	-7.75	1.77	44.8	2
632.8	-12.33	1.21	43.6	7
647.1	-13.67	1.05	43.5	10
676.4	-16.01	0.94	43.6	14

[a]Literature values (Ref. 6).

4.3.2 Characterization of the SiO_2 layer

For microscopical plasmon decay length observations a substrate with an SiO_2 test pattern on top of the gold layer was made in the way described briefly in the sample preparation section (Sec. 4.2.3). The thickness of the pattern was measured using the automated features of the setup, which make it possible to measure complete reflectance curves of several microscopically small areas simultaneously within one laser beam.

First, using the computer, two small areas (*e.g.*, 25×25 μm) are defined in the microscopical image: one in an uncovered gold area and one in an SiO_2-covered area. The intensity in these areas is measured for both *p* and *s* polarization: by dividing (*p*/*s*) we can correct for polarization-independent, non-SPR intensity variations and normalize the

reflectance values. After the incident angle is incremented with 0.01 deg. the whole procedure is repeated. In this way, full reflectance curves for both areas are determined by measuring the average intensity in each area as a function of the angle of incidence.

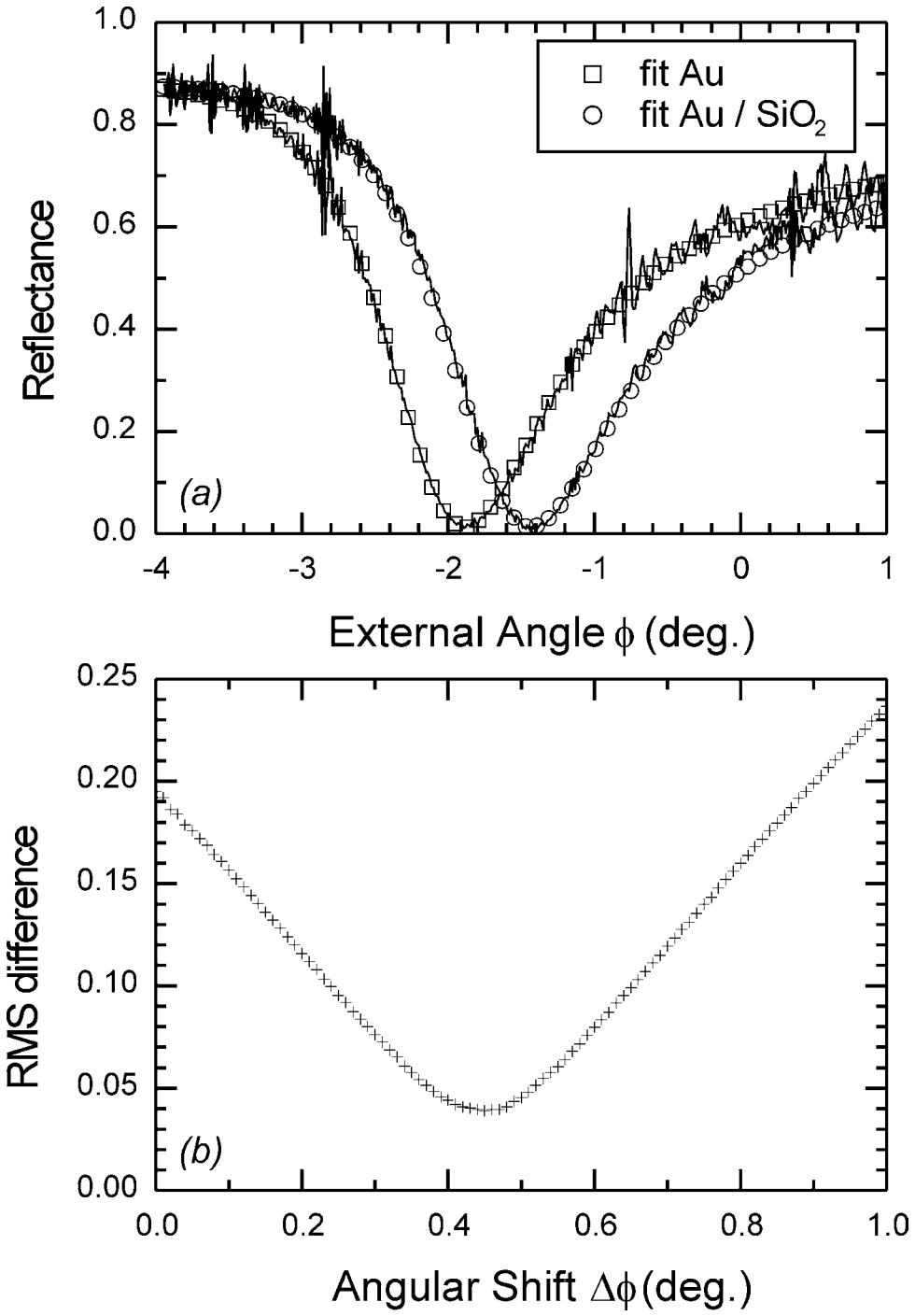

Fig. 4.5 ***(a)*** Microscopic reflectance scans at λ=632.8 nm for the bare gold layer and for the SiO_2-covered region, measured simultaneously within the same SPM image. ***(b)*** The root-mean-square value of the difference of both reflectance curves, as a function of their shift towards one another.

This fully automated process results in reflectance curves as displayed in Fig. 4.5*(a)*. The SiO_2 layer thickness can be calculated with the determined angular shift of the measured reflectance minima. Figure 4.5*(b)* shows the overall reflectance difference defined as the root-mean-square (rms) value of the difference of the reflectance curves when the two curves are shifted towards one another by $\Delta\phi$:

$$\text{rms difference}(\Delta\phi) = \sqrt{\frac{1}{n}\sum_{i=1}^{n}\left[R_{Au}(\phi_i) - R_{SiO_2}(\phi_i + \Delta\phi)\right]^2} \qquad (4.1)$$

The measured shift for the SiO_2 layer is $\Delta\phi$=0.45 deg. (λ=632.8 nm). Using Fresnel theory and assuming a refractive index of 1.46, a thickness of 2.5 nm was found. The accuracy in the measured shift is about 0.01 deg., corresponding to a thickness resolution better than 0.1 nm.

4.3.3 Decay length measurement

In Fig. 4.6 a 125 μm wide part of the test pattern as described in Sec. 4.2.3 is imaged using five different wavelengths. Because of the high magnification the effect of the plasmon decay length is visible for the longer wavelengths, in the horizontal direction. The surface plasmons propagate from left to right and the dark area in the middle is the bare gold at resonance. The contrasts in the images in Fig. 4.6 were made equal by analog and digital amplification, to use the full gray scale.

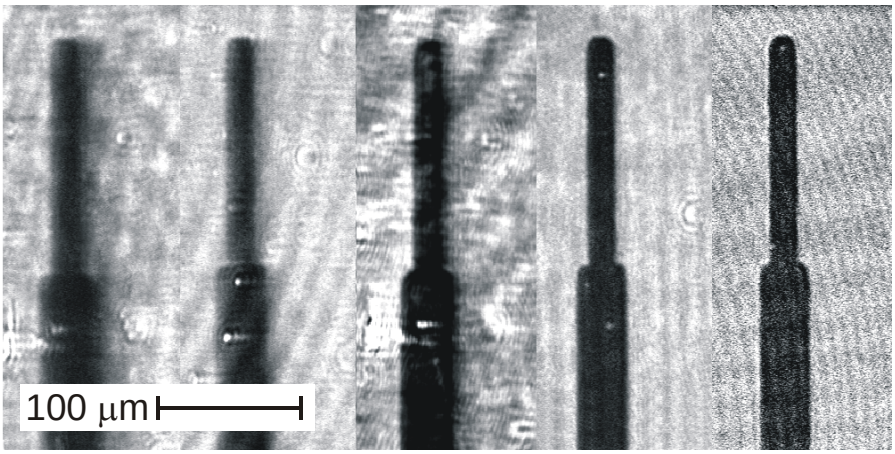

Fig. 4.6 A part of the SiO_2 test pattern on gold, imaged with five wavelengths: 676.4, 647.1, 632.8, 568.2, and 530.9 nm, respectively (from left to right). Correction using *p* and *s* polarized light was applied. The plasmon wave vector is pointing to the right, and the dark area is the bare gold at resonance. The contrast of the images is chosen such that the gray value range is used in an optimal way. A detailed analysis of the images is given in Fig. 4.7.

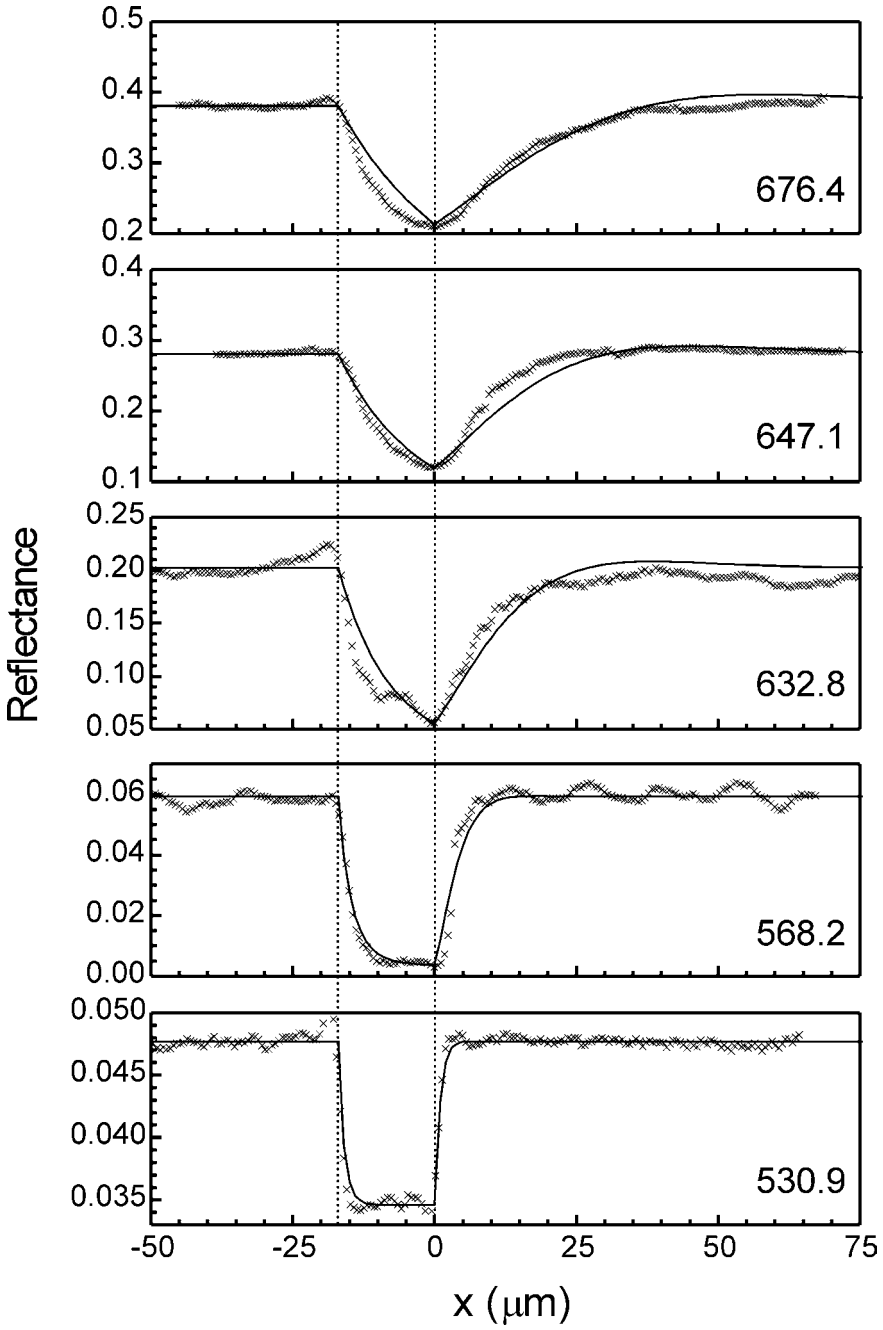

Fig. 4.7 The intensity profiles of the images in Fig. 4.6 with indicated wavelengths. The solid lines represent the intensity profiles calculated with the dielectric constants and layer thicknesses obtained from the SPR experiments and the model presented in Chapter 3.

In Fig. 4.7 the intensity profile in the horizontal direction is given, averaged over a number of image lines crossing the 18 μm wide upper part of the bare gold in Fig. 4.6. The solid lines in the same figure correspond with the results of the model presented in Chapter 3 using the parameters derived from the ATR fits and the dispersion relation.

Generally, the correspondence between model and experiments appears to be satisfactory. The distance from the index step at which the reflectance is changed to 1/*e* of its eventual change is also found to be proportional to the decay lengths calculated and given in Table 4.I. This points to the fact that we can predict the lateral resolution that can be obtained using a certain wavelength.

Because of the finite numerical aperture (NA 0.19) of the objective used, decay lengths shorter than that for the 530.9 nm wavelength cannot be observed in the microscopic image. It may be concluded that for this objective the 530.9 nm wavelength is the best choice for a high lateral resolution. Shorter wavelengths would diminish the contrast even more and would not contribute to the lateral resolution of the setup. The diffraction limited lateral resolution for this objective and wavelength is 2 μm, based on the Rayleigh criterion.

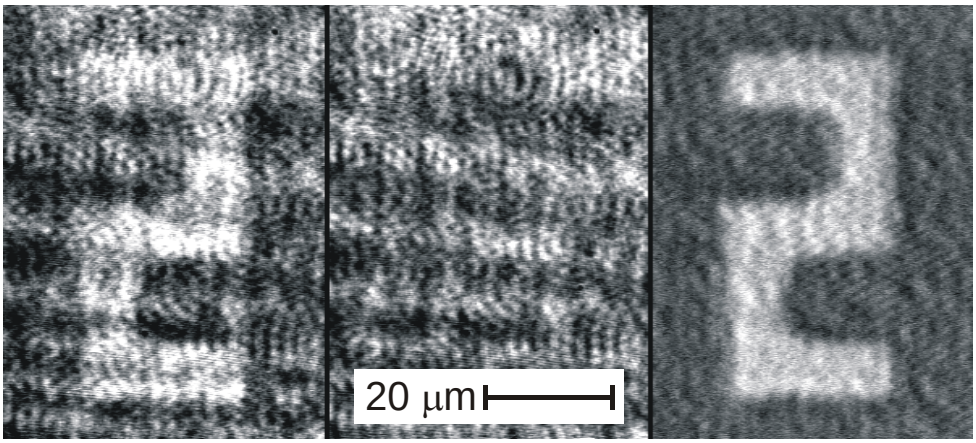

Fig. 4.8 Example of the suppression of the effect of lateral inhomogeneities in the light beam by the division of images acquired with *p* and *s* polarization. From left to right we see the *p* and *s* polarized image, and the ratio of the two.

4.3.4 Imaging the SiO_2 layer

In Fig. 4.8 the effect of using the ratio of the *p* polarized to the *s* polarized image to correct for beam inhomogeneities, is shown for an SPM image of a part of the SiO_2 test pattern. The same part is imaged with both AFM in the deflection mode[8] and SPM with λ=530.9 nm, to check the contours of the object and to test the lateral resolution of the SPM images (Fig. 4.9). The NA of the objective used was 0.49 (diffraction limited resolution: 1 μm). In the AFM image the edges of the test structure are very sharp and we can recognize the rounded corners that we already saw in the SPM images (this is also true for the part that was used for determination of the decay lengths). Although the effect of the lateral

intensity inhomogeneities is still visible in the SPM image, we estimate the lateral resolution of the image to be 2 μm. The difference in reflectance for the gold and the SiO_2 can be calculated and is about 0.01.

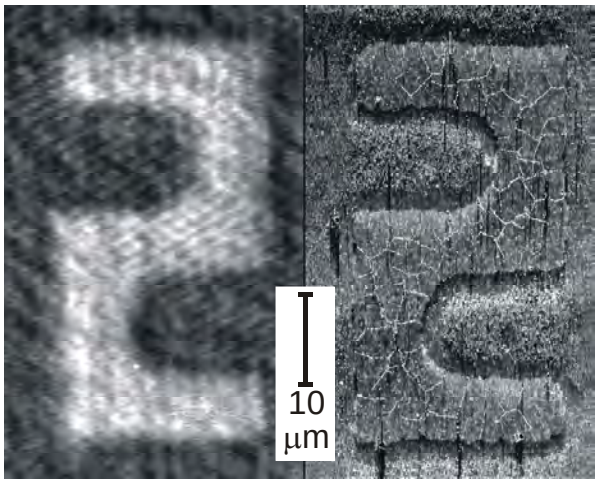

Fig. 4.9 AFM and SPM images of the same, small part of the test pattern. Comparing these images we estimate the resolution of the SPM image to be 2 μm (NA 0.49). Unresolved cracks in the SPM image are visible in the AFM image.

4.4 Conclusion

We have shown that it is possible to characterize SPR substrates accurately, and that this allows for making an optimal choice for the wavelength, regarding lateral resolution in SPM. Surface plasmon decay lengths were calculated from the determined dielectric function, and observed with the surface plasmon microscope. The intensity profile could be described with a phenomenological model. The trade-off relation between decay length and reflectance difference makes it necessary to apply several improved image acquisition techniques when short wavelengths are used. In this way diffraction-limited SPM images can be obtained while retaining the very high thickness resolution. A transparent SiO_2 test pattern of 2.5 nm thickness was characterized using AFM and a new method to obtain reflectance curves of microscopically defined areas automatically. Comparing the AFM and SPM images led to the conclusion that the lateral resolution of the SPM image is 2 μm. This resolution is limited by lateral inhomogeneities in the incoming laser beam that could not be corrected completely. Some of the inhomogeneities are created in the objective, and we expect that by choosing a specialized objective (*e.g.*, with a better coating) the resolution can be improved a little more (to the diffraction limit).

4.5 References

(1) Rothenhäusler, B.; Knoll, W. *Nature* **1988**, *332*, 615.
(2) Hickel, W.; Knoll, W. *Thin Solid Films* **1990**, *187*, 349.
(3) Pockrand, I. *Surf. Sci.* **1978**, *72*, 577.
(4) Rothenhäusler, B.; Knoll, W. *J. Opt. Soc. Am. B* **1988**, *5*, 1401.
(5) Schröder, U. *Surf. Sci.* **1981**, *102*, 118.
(6) Johnson, P. B.; Christie, R. W. *Phys. Rev. B* **1972**, *6*, 4370.
(7) Dujardin, M. M.; Thèye, M. L. *J. Phys. Chem. Solids* **1971**, *32*, 2033.
(8) Binnig, G.; Quate, C. F.; Gerber, Ch. *Phys. Rev. Lett.* **1986**, *56*, 930.

CHAPTER FIVE

SPM APPLIED TO LIPID LB MONOLAYERS

In this chapter an introduction to Langmuir-Blodgett (LB) films will be given, after which the application of SPM to the characterization of these films will be demonstrated. Apart from their biological relevance (as model systems for biological membranes) these films are a challenge to any form of microscopy since they are transparent and very thin (about 2 nm). In the sixth and last chapter a new form of atomic force microscopy (AFM) will be applied to these films.

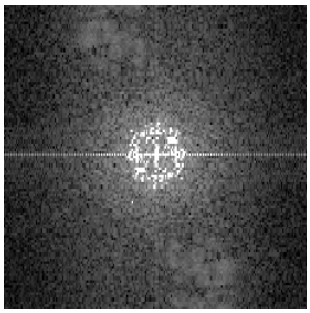

5.1 Biological membranes

In 1925 Gorter and Grendel came with their hypothesis that all living cells are surrounded by a lipid bilayer.[1] They concluded this from an experiment that was met with a lot of criticism. In 1966 it was finally discovered that in fact they had made two mistakes that miraculously canceled each other out and that their conclusion was right. The only thing that had to be added to their model was the fact that in the natural membrane a variety of proteins (receptors) are embedded. This currently accepted model is known as the fluid mosaic model (see Fig. 5.1)[2,3].

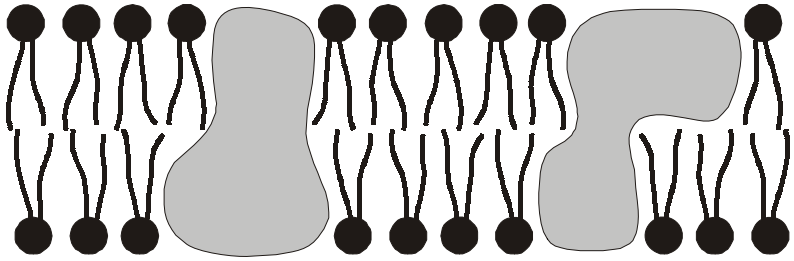

Fig. 5.1 Fluid mosaic membrane model: the natural membrane is a lipid bilayer, with embedded proteins.

Lipid bilayers consist of amphiphilic molecules which in their turn consist of a hydrophobic ('water-fearing') part, and a hydrophilic ('water-loving') headgroup. dimiristoylphosphatidylethanolamine (DMPE), is an example of a amphiphilic membrane component, with a hydrophilic headgroup and two hydrophobic alkylchains (see also Section 5.2.1 and Fig. 5.5).

Many essential functions of living cells are performed by events associated with their membranes. The amount of protein in biological membranes varies between 30 and 70% depending on the function of the cell. The basic functions of biological membranes can be divided in three groups:[4]

(i) *Organization*: energetically most favorable spatial arrangements of chemical reaction sites and cell components.

(ii) *Interaction*: transport of substances.

(iii) *Information*: cell recognition and adhesion, immune reactions.

Because of various enzymes and other functional proteins attached to or embedded in membranes, they are involved in many metabolic processes. The two important energy conversion processes, photosynthesis in chloroplasts and oxidative phosphorylation in mitochondria, are carried out in membranes.[5] To understand these and many other processes, which are essential for living organisms, it is necessary to obtain knowledge of

molecular structure and function of the membrane, preferably at a very high resolution.

5.1.1 Biomembrane models

The complexity of the biomembrane is such that frequently simpler systems are used as models for physical investigations. They are based on the spontaneous self-organization of the amphiphilic lipid molecules when brought in contact with an aqueous medium. The three most frequently used model systems are: *(i)* monolayers; *(ii)* black lipid membranes (BLM); *(iii)* vesicles or liposomes (see Fig. 5.2).

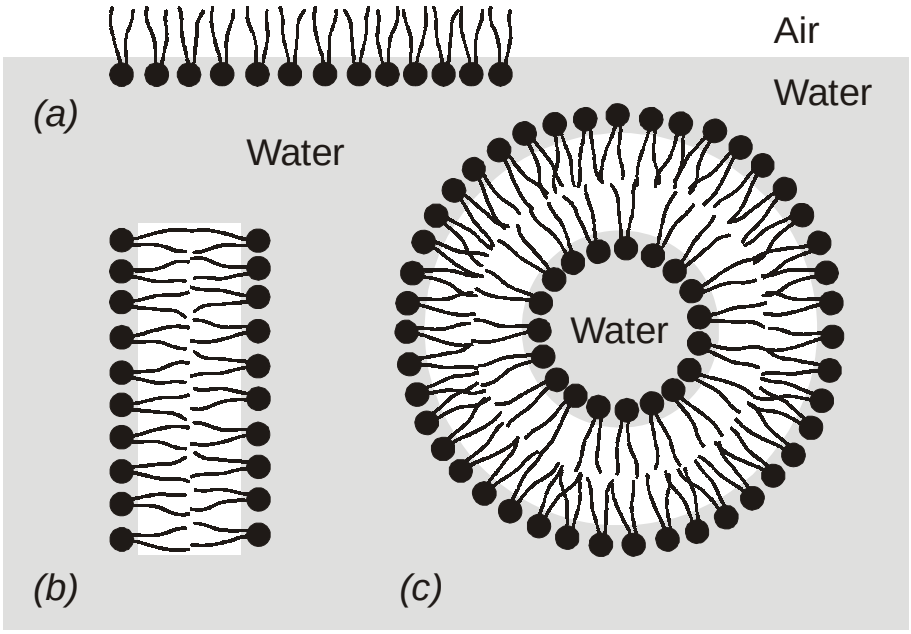

Fig. 5.2 Three of the most frequently used model systems: ***(a)*** monolayers at the air-water interface; ***(b)*** black lipid membranes (BLM); ***(c)*** vesicles or liposomes.

BLM and vesicles consist of lipid bilayers separating two aqueous compartments. They make the measurement of *e.g.*, membrane resistance, capacity and permeability possible. Liposomes are spherical lipid multi-layers.

An aspect of the model systems that has considerable relevance in the biological field, is their ability to undergo phase transitions (see Section 5.2.1). It is known that biomembranes tend to adapt to the ambient conditions to maintain themselves in a transitional state.[6] In particular, it is thought that separate domains of lipid in different phases exist in real biomembranes. Because of this biological relevance, as well as their intrinsic interest, much attention has been paid to the phase transitions of simple model membrane systems.

A monomolecular layer of lipid molecules spread at the air-water interface is a system in which the transitions have been exhaustively studied.[7] The hydrophilic parts of the molecules are then submerged in the water, while the hydrophobic parts remain outside and interact with each other to form a layer.

The monolayer at the air-water interface represents only one half of the naturally occurring bilayer, but allows the packing density of the spread lipid molecules to be varied by changing the available area per molecule. Therefore, monolayers can yield precise information on molecular packing and orientation, although they cannot provide information on membrane conductance, as is provided by BLM studies, or membrane permeability, as provided by liposome work.[5] Thus, the monolayer can give precise information on membrane constituents organized in a membrane-like environment, but is less able to provide direct information on membrane functionality.

An advantage of the lipid monolayer as a model is that it can be transferred to a solid substrate, using the Langmuir-Blodgett (LB) technique, allowing it to be studied using a whole range of techniques. The spreading of lipid monolayers, monolayer experiments and the Langmuir-Blodgett technique will be discussed in the next section.

5.2 Monomolecular layers

In this section monolayer spreading and deposition is treated. The measurement of isotherms is described, and the interpretation of isotherms is discussed.

5.2.1 Monolayer spreading

Monomolecular films on a water surface (named Langmuir films, after Irving Langmuir 1881-1957), can be prepared by spreading: when a lipid solution in a water-immiscible solvent such as chloroform is dropped onto a water surface, the solution spreads rapidly to cover the available area. After the solvent is evaporated, the lipid molecules are left behind at the air-water interface.[7]

The amphiphilic lipid molecules will naturally orient themselves such that the hydrophilic headgroups are immersed in the water surface and the hydrophobic tailgroups remain outside and interact with each other. When a large water surface area per molecule is available, the film molecules move independently on the surface. Such a film is called a ‘gaseous’ film, in two dimensions. The monolayer can be compressed by

decreasing the surface area with a moveable barrier (see Fig. 5.3). The barrier is in contact with the water and the lipid molecules cannot pass the barrier.

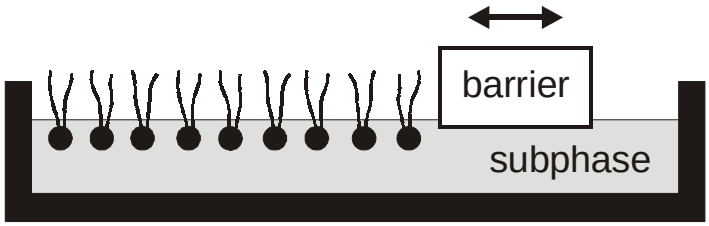

Fig. 5.3 Schematic drawing of a monolayer at an air-water interface. The monolayer can be compressed by moving the barrier to the left.

For a compressed monolayer, the van der Waals forces are very large, the film molecules are not allowed to move about freely, and thus the film resembles a 'solid' in a two-dimensional crystalline phase. When the van der Waals forces between the molecules are weaker at larger molecular areas, the result is a 'liquidlike' film.

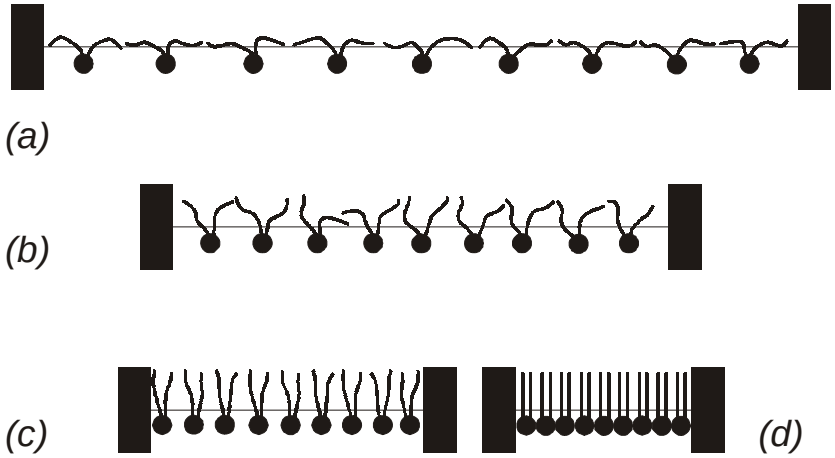

Fig. 5.4 Different phases of a monolayer: ***(a)*** gaseous phase; ***(b)*** Liquid-Expanded phase; ***(c)*** Liquid-Condensed phase; ***(d)*** Solid-Condensed phase.

Generally, a distinction is made between films in a liquid-expanded state (LE) and films in a liquid-condensed state (LC). It is not clear what the conformation of molecules in those phases looks like, but generally the conformations are envisaged as shown in Figure 5.4. The problem is that, as far as the conformation is concerned, it is not known where to draw the line between both phases. In the next section it will become clear why this distinction is made. Möbius gave a slightly different interpretation of the phase transitions.[8] He divided the molecule under

study in three sub-units, with each phase transition corresponding to one sub-unit being lifted from the water surface.

Molecules in the solid phase, have a dense packing of the headgroups or of the alkyl chains, depending on their relative sizes. Further decrease of the surface area results in the collapse of the monolayer by formation of undefined multilayers. The collapse areas for stearic acid and DMPE are determined by their alkyl chains.

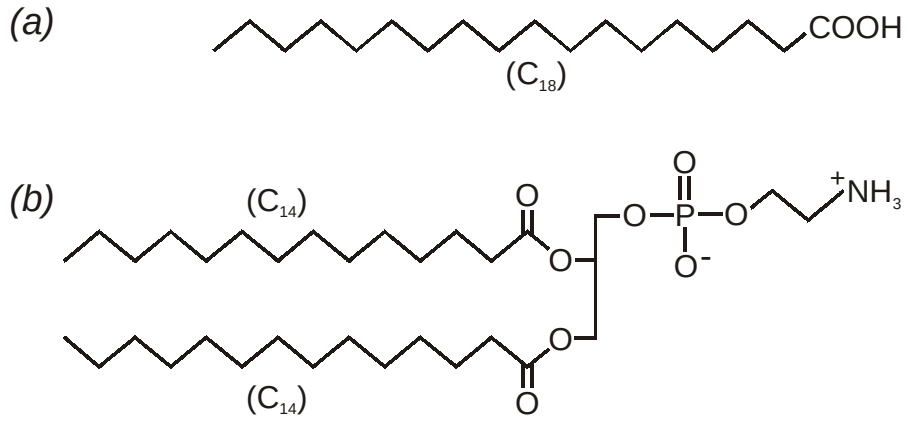

Fig. 5.5 Molecular structure of: ***(a)*** stearic acid; ***(b)*** dimyristoyl-phosphatidylethanolamine (DMPE).

It is obvious that the role of the interaction of the subphase, *i.e.* water, with the film-forming substance is very important. For example, the dipolar nature of the molecules (see Fig. 5.5) has the effect of aligning the dipoles at the air-water interface. If there are sufficient ions in the subphase, this electrostatic interaction will be more or less shielded, which will reduce the interaction between the dipoles.

The presence of a molecular film on the surface of the water has a pronounced effect on the physical properties of the air-water interface. In the next section, the influence of a monolayer on the surface pressure and its measurement will be discussed.

5.2.2 Surface pressure measurement

The water surface on one side of any imaginary line pulls perpendicular to this line with a force equal and opposite to that exerted by the surface on the other side of the line. The force acting perpendicularly to a line of unit length is called the surface tension γ, measured in N/m or mN/m. The surface pressure π of the monolayer is defined as the lowering of the surface tension due to the presence of the monolayer on the water surface:

$$\pi = \Delta\gamma \qquad (5.1)$$

It can be interpreted as the two-dimensional analog of the three dimensional pressure. The measurement of the surface pressure as a function of the available area per molecule can provide information concerning molecular dimensions and intermolecular interactions.

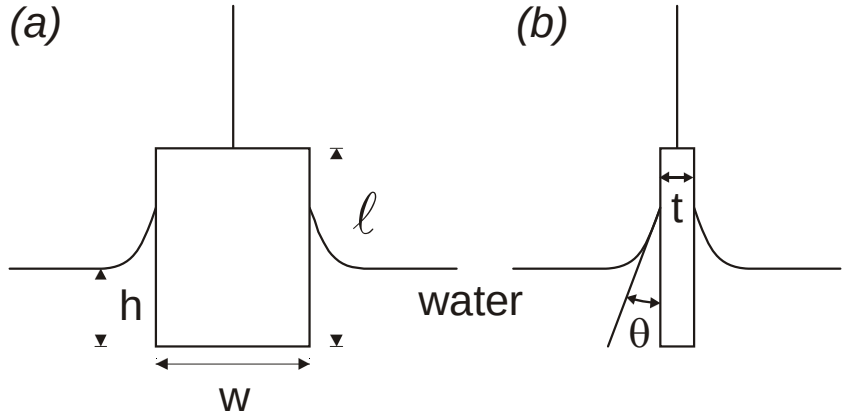

Fig. 5.6 Wilhelmy plate with dimensions indicated, immersed to a depth *h* in water, with a contact angle θ: ***(a)*** front view; ***(b)*** side view.

A method frequently used to determine the surface pressure resulting from monolayer compression is the Wilhelmy plate method (see Fig. 5.6). It is a highly accurate method for the measurement of the surface tension. Using the Wilhelmy method, a measurement is made by determining the force due to surface tension, on a plate which is suspended so that it is partially immersed in the water subphase. The forces acting on the plate consist of gravity and surface tension which pull downward (for a hydrophilic plate), and buoyancy due to displaced water which gives an upward force. For a rectangular plate of dimensions *l*, *w* and *t*, and material of density ρ_P, immersed to a depth *h* in a liquid of density ρ_L the net downward force is given by:

$$F = \rho_P glwt + 2\gamma\,(t + w)\cos\theta - \rho_L ghwt \qquad (5.2)$$

where γ 1is the surface tension, θ is the contact angle on the solid plate, and *g* is the gravitational constant. Materials that are generally used for the Wilhelmy plate are clean filter paper or platinum. When completely wetted, the contact angle will almost be zero ($\theta \approx 0°$).

5.2.3 Monolayer isotherms

By quasi-statically moving the barrier and simultaneously measuring the surface pressure, the surface pressure can be determined as a function of the area of water available to each molecule. Because the temperature is kept constant, this relation is known as the surface pressure

vs. area isotherm, usually abbreviated to 'isotherm', the two dimensional analog of the three dimensional *P*/*V* diagram. If the area per molecule is sufficiently large, ideal gas films obey the relationship:

$$\pi A = kT\,, \tag{5.3}$$

where *k* is the Boltzmann constant. This relationship is analogous to the three-dimensional gas law (*i.e.*, *PV*=*kT*). In general, ideal gas behavior is observed only when the distances between the molecules are very large and the surface pressure is very small (less than 0.1 mN/m).

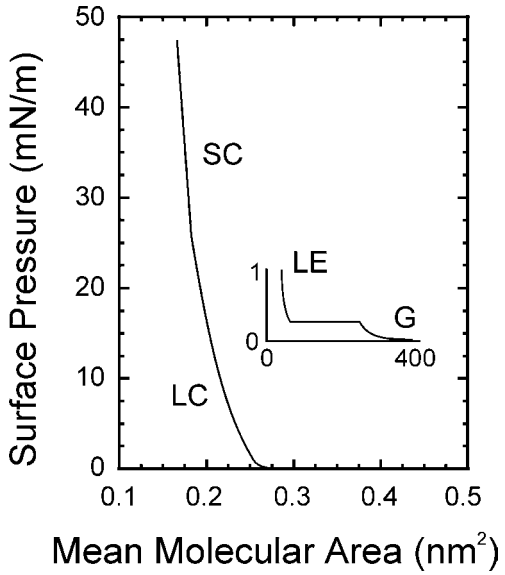

Fig. 5.7 The isotherm of stearic acid. The inset does not represent measured values, but serves as illustration for the behavior at very high available area.

In Figure 5.7 the isotherm for stearic acid is given (taken from Ref. 9). On examining this isotherm, a number of distinct regions become immediately apparent. If the surface area is reduced from an initial high value, with the monolayer in a gaseous state, there is a gradual onset of surface pressure until an approximately horizontal region is reached (inset Fig. 5.7). This is the gaseous-liquid expanded (LE) transition in the stearic acid isotherm. In the horizontal region the hydrophobic tailgroups, which were originally lying almost flat on the water surface, are subsequently being lifted from that surface. The inset in Figure 5.7 does not represent measured values, because the surface pressure in this region is so low that this portion of the isotherm is not resolved by measurements. Analogous to a 3D-gas, the compressibility is defined as:

$$\kappa = -\frac{1}{A}\left(\frac{\partial A}{\partial \pi}\right)_T . \tag{5.4}$$

The gaseous-liquid expanded transition of stearic acid is an example of a first order transition, which is characterized by a horizontal slope in the isotherm, with the compressibility approaching infinity.

There follows an abrupt transition to the liquid-condensed (LC) phase at an area per molecule of 0.28 nm^2. The different phases are observed as portions of the isotherm with different slopes. In the liquid condensed phase the slope of the isotherm, and thus the compressibility, is approximately constant.

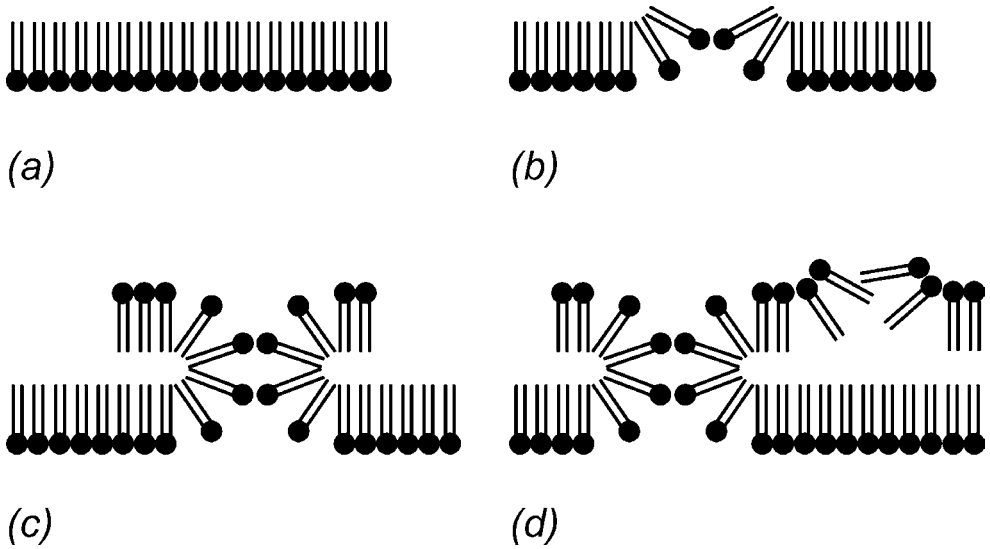

Fig. 5.8 The collapse mechanism by which undefined multilayers are formed.

At a surface area of just over 0.2 nm^2 per molecule there is an abrupt increase of slope. Clearly, this is due to a phase change as well and represents a transition to an ordered solid-like arrangement of the molecules, known as the solid condensed (SC) or solid phase. In this phase the molecules are close-packed, and an all-trans (straight) chain configuration can be achieved (see Fig. 5.4). If this second linear portion of the isotherm is extrapolated to zero surface pressure, the intercept gives the area per stearic acid molecule that would be expected for the hypothetical state of an uncompressed close-packed layer. This value of 0.22 nm^2 per molecule is close to that occupied by stearic acid molecules in single crystals, which confirms the interpretation of a compact film as a two-dimensional solid. The mean molecular area in close-packed configuration is equal to the cross-sectional area per CH_2 chain.[10] Further reduction of the surface area results in the collapse of the monolayer (see Fig. 5.8). Because molecular layers are riding on top of each other the compressibility then approaches infinity again.

For a DMPE monolayer a different isotherm is measured (see Fig. 5.9; taken from Ref. 11). For mean molecular areas around 0.5 nm^2 the

compressibility approaches infinity, indicating a first order phase transition from the LE to the LC phase. In first order phase transitions, phases coexist in separate domains, as will be discussed in Section 5.3.

The LC-SC transition is indicated by an abrupt increase in slope in the already steep portion of the isotherm. Note that the collapse area is approximately twice that of stearic acid because of the second CH_2 chain of the DMPE molecule. The characteristics of the isotherms however, do not depend only on the molecules. The subphase is also very important, in particular the pH and the ion strength of the subphase. The influence of the temperature is analogous to that for a 3D-gas, but for monolayers there can be more phase transitions.

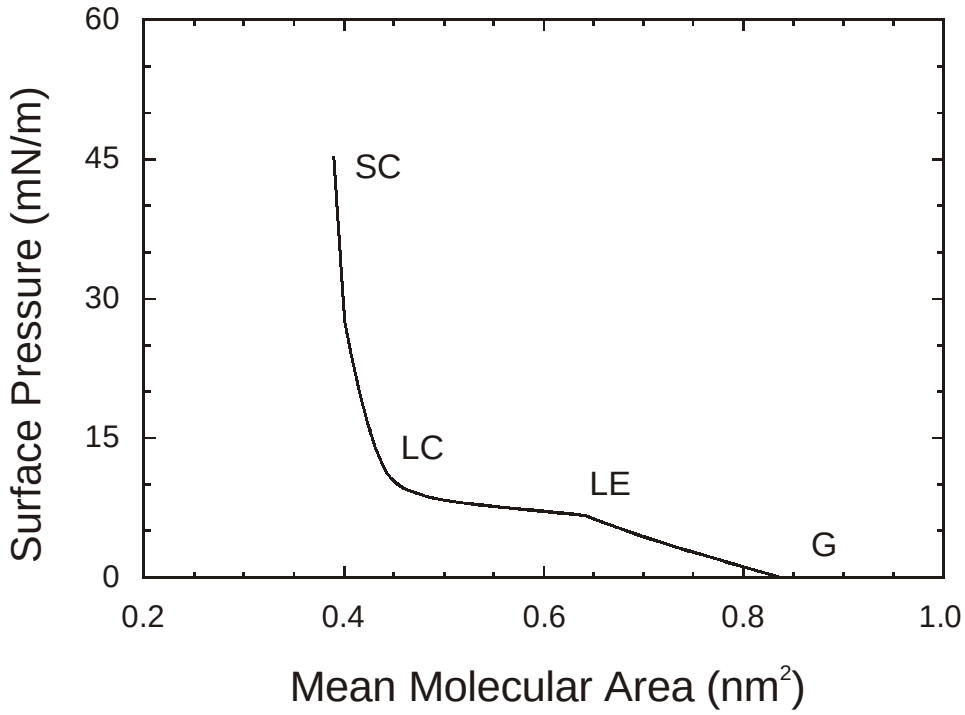

Fig. 5.9 The DMPE isotherm.

5.2.4 Langmuir-Blodgett deposition on a solid substrate

For some microscopy techniques it is necessary to transfer a monolayer from the water surface to a solid substrate. The technique to do this has become universally known as the Langmuir-Blodgett (LB) technique.[12] For LB deposition, a substrate is first lowered through the monolayer so that it dips into the subphase, and then withdrawn. If the substrate used is hydrophilic, then deposition will follow the sequence of events shown in Figure 5.10.

During the lowering of the slide, the water wets the slide's surface and the meniscus turns up, but there is no deposition at this stage. As the slide is withdrawn, the meniscus is wiped over the slide's surface and

leaves a monolayer behind. During this process the surface pressure is kept constant, using the surface pressure as a feedback signal for adjusting the barrier position. The value of surface pressure that gives best results depends on the nature of the monolayer but is usually more than 10 mN/m. In the deposited monolayer the hydrophilic groups are turned toward the hydrophilic surface of the slide. Initially there is liquid film between the monolayer and the slide's surface and bonding is completed after the water layer has drained away or evaporated.

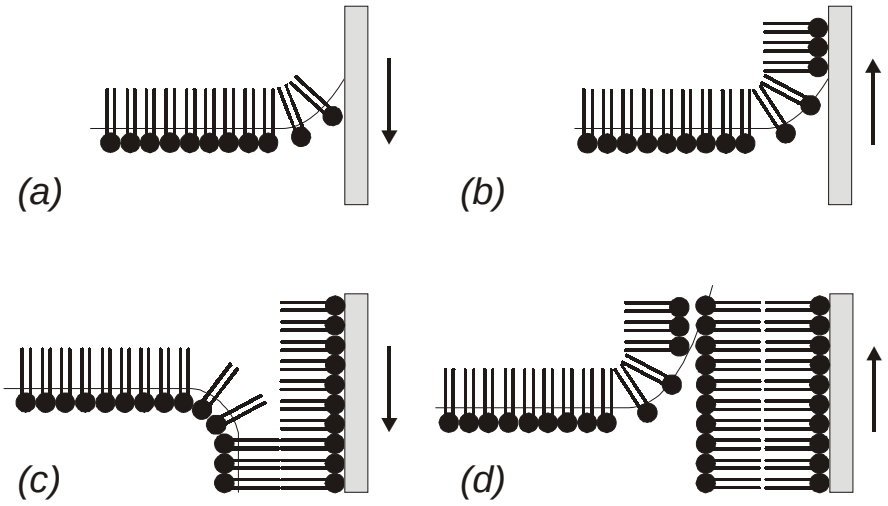

Fig. 5.10 Deposition of multilayers by the Langmuir-Blodgett technique: ***(a)*** first immersion; ***(b)*** first withdrawal; ***(c)*** second immersion; ***(d)*** second withdrawal.

The rate at which the slide can be withdrawn from the water while a homogeneous film is deposited, is typically 1 mm/s. This rate depends on the rate at which the water film drains from the monolayer-slide interface and on the viscosity of the monolayer. A highly viscous monolayer will be unable to maintain a homogeneous film in the neighborhood of a rapidly moving slide.

To deposit a second layer onto the slide, the slide is again lowered through the monolayer. This time the slide's surface is hydrophobic; the meniscus turns down and the second monolayer is deposited with its hydrophobic tailgroups in contact with the exposed tailgroups on the slide. At the second withdrawal the next monolayer is deposited like the first, onto the hydrophilic headgroups of the last monolayer. If the monolayer material shows poor adhesion to the substrate, then the second immersion in the water can simply lead to the monolayer peeling off the slide and respreading on the water surface. Repeated dipping will then lead to a single deposited monolayer on the slide.

Because during dipping the pressure is kept constant, the barrier will move to compensate for the deposited molecules. By measuring the change

in available surface on the water and the surface area of the substrate, the transfer ratio can be determined.

5.3 Domain formation in lipid monolayers

In a previous section it was mentioned that during a phase transition in a monolayer, different phases coexist, organized in separate domains. A problem encountered when describing domain formation is that the description is completely different for different compounds and conditions. In this section only the most essential and general aspects are discussed.

5.3.1 Domain nucleation and growth

In this section we will consider domain nucleation and growth in a film in an LE-LC phase transition. LC domains will be referred to as 'solid' and LE domains as 'fluid' or 'liquid'. In the LC domains the molecules attain a near close-packed configuration. In the LE domains the molecules have more freedom to move, with flexibility increasing along the chain with the distance from the anchoring hydrophilic group.

Consider a lipid monolayer composed of liquid and solid domains, and for simplicity assume that the pure liquid and pure solid phases are incompressible. For a given water surface area, the fractions of the area covered by fluid and solid phases are then fixed. A state of global equilibrium is achieved once the number and shape of the solid domains correspond to the minimum energy state of the film.

On first slowly compressing a monolayer, a certain number of solid domains appears by a nucleation process.[13,14] On further compression, these domains usually grow in size but not in number. If the monolayer is compressed rather quickly or if the impurity content is high, a large number of nuclei are formed. If compression speed is decreased the domain size is increased.[14,15] In Ref. 16 the onset of the phase transition was detected before solid domains were visible with fluorescence microscopy. Therefore, it was suggested that domain formation results from aggregation of unresolved particles of condensed lipid.

Domain shapes are reversible with respect to growth and decay, even if these shapes are complex:[14,17] the same kind of shapes are observed before and after compression and subsequent decompression. The changes are also reversible with respect to the temperature.[18]

The alignment of polar or charged molecules in the solid domains causes long-range electrostatic forces. Due to the electrostatic repulsion between the solid domains, they are separated by an approximately constant distance. For fusion of domains, a favorable relative orientation of colliding domains is necessary. This can be explained by the fact that the lattices of the crystalline domains must match. In that case the van der Waals forces between the touching lipid chains of both domains exceed the electrostatic repulsion.[19]

5.3.2 Domain shapes

The shape of domains depends on the monolayer compound and the experimental conditions, and is determined by a thermodynamic equilibrium. More precisely, there is a competition between the long-range electrostatic dipolar repulsion F_{el} and the line tension λ. The line tension represents the tendency to minimize boundary length. The shape of an individual solid domain is determined by the interplay of these forces:[13,18,20-22]

$$F = \lambda p + F_{el} \tag{5.5}$$

Here p is the perimeter of the solid domain. The electrostatic repulsion favors elongation and narrowing, while the line tension favors short boundaries and thus round domains.

Initially, the domains cover a small fraction of the area of the air-water interface, and are relatively far apart. Therefore, the electrostatic interaction is small, and circular shapes result. As the domains grow in area they come nearer to each other and tend to thin in one dimension because of the long-range dipolar forces. Experiments have confirmed the existence of the electrostatic interaction. Domains were microscopically observed while repelling each other over distances of tens of micrometers and could be moved by applying an electric field.[18]

In the absence of charged headgroups, the minimum energy domain shape is determined entirely by line tension and is circular for an isotropic solid. In the other extreme, when the charge is large and the line tension is weak, and if the domain does not break into pieces, the minimum energy shape is highly elongated. This effect can be observed when a small amount of cholesterol is added to a charged monolayer. This results in a strongly decreased line tension and the mentioned longer and thinner domains.[21]

Because the electrostatic repulsion influences the domain formation, domain shapes also depend on the ionic conditions of the water subphase. In Ref. 23 it was shown that an increase in the

concentration of monovalent ions increased the pressure corresponding to the LE-LC phase transition of the lipid dilauroylphosphatidic acid (DLPA). Increasing the concentration of divalent ions had the opposite effect. These effects were ascribed to an increase in surface charge density in the former case, and to screening of electrostatic forces in the latter. Thus, it was possible to vary the size and shape of the domains at the air-water interface with the ionic conditions.

Another important factor is whether the packing of the molecules is determined by the chains or by the headgroups. For phospholipids and fatty acids, where crystallization is basically determined by the chain arrangement, the solid domains exhibit rounded boundary lines. If the packing is determined by the headgroups, domains exhibit pointed perimeters (*e.g.* the polymerizable diacetylenic lipid Bronco).[14]

5.4 LB film characterization with SPM

Most of the facts discussed in the previous sections of this chapter were originally discovered using fluorescence microscopy.[14,24] However, there are many other monolayer characterization methods to determine domain shapes, layer thickness or lattice constants of crystalline domains, as mentioned in the first chapter.

Now we will show how surface plasmon microscopy (see also Chapter 1) can be used to image and characterize phase-separated lipid LB films.

5.4.1 Experimental section

The substrate preparation and setup that was used is described in the previous chapter. The 2.5 nm thick SiO_2 layer (without pattern) is in this case needed to make the substrate hydrophilic for deposition of the Langmuir-Blodgett lipid monolayer. LB films were obtained by spreading a 1 mg/ml solution of the lipid dimiristoylphosphatidylethanolamine (DMPE) in 3:1 (v/v) chloroform/methanol onto the subphase (deionized water, pH~7.5). The monolayer was transferred to the substrate at a surface pressure of 20 mN/m and a molecular area of 0.5 nm^2; the transfer ratio was about 1. The DMPE monolayer is under those conditions in an LE-LC phase transition (see Fig. 5.9). All experiments were carried out at room temperature.

5.4.2 Results and discussion

Using the image acquisition techniques that were described in Chapter four, the DMPE monolayer was imaged for a wavelength of 568.2 nm. Figure 5.11 shows the resulting images for *p* and *s* polarization, the ratio of the two and the result after Fourier filtering to remove some residual fringes. For this wavelength the optical thickness variations in the monolayer under investigation hardly give any contrast

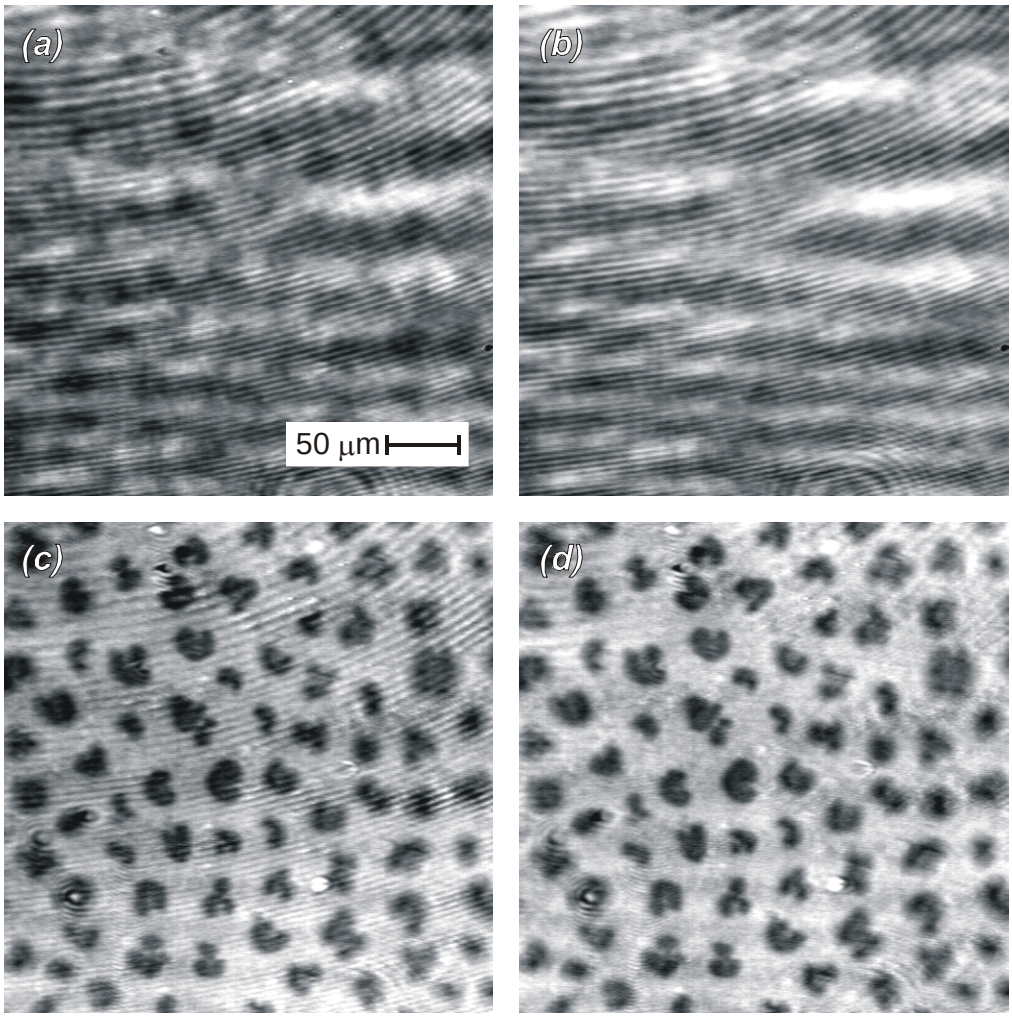

Fig. 5.11 SPM images of a phase-separated DMPE monolayer: ***(a)*** for *p* polarization; ***(b)*** for *s* polarization; ***(c)*** the ratio of the two; ***(d)*** the result after Fourier filtering to remove some residual fringes.

in the separate images. After division of the two however, a good contrast results and the lateral resolution is higher than it would have been for a longer wavelength (usually a wavelength of 632.8 nm is used). Due to the high dynamic range of the images, quantization levels do not become

visible after the expansion of the gray scale. The dark 'islands' in the image are the LC domains surrounded by the LE phase. Because the monolayer was imaged under an angle only the middle part is optimally focussed.

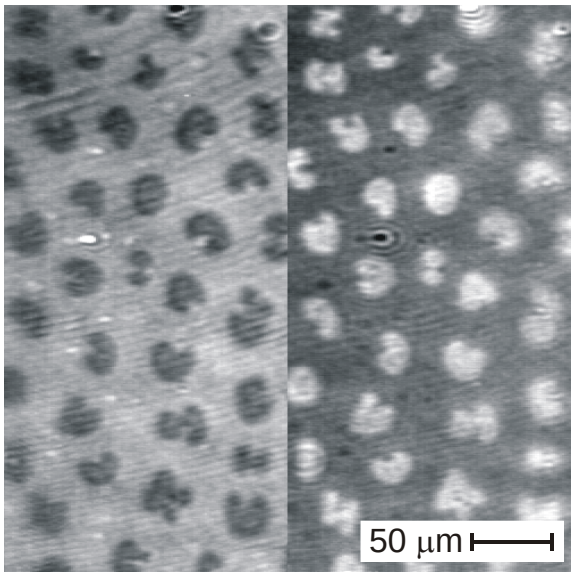

Fig. 5.12 SPM image of a DMPE monolayer in a transition from the LE to the LC phase. Contrast inversion was obtained by choosing a different angle of incidence. On the left and right side the LC and LE part are at resonance, respectively.

By choosing either the resonance angle for the LE phase or the one belonging to the LC part of the monolayer as angle of incidence, the contrast can be inverted (see Fig. 5.12). We estimate the lateral resolution that was obtained to be 3 μm (NA 0.19).

To evaluate the thicknesses of the different domains, microscopic ATR scans were made of three different areas: the bare gold-SiO_2, an LE domain, and an LC domain. The ATR curves for the covered areas were shifted relative to that of the bare area with 0.17° and 0.23°, respectively (Fig. 5.13). In Fig. 5.14 the possible thickness and refractive index combinations are given for both domains. Assuming a refractive index of 1.5 (Ref. 25) for both domains, the imaged thickness difference is less than 0.4 nm. When a higher refractive index is chosen for the condensed domain and a lower one for the expanded domain, the resulting thickness difference is even smaller. These values have been found by others as well, for similar systems.[26,27] If it were possible to determine refractive index and monolayer thickness separately, then the nature of the monolayer packing could be further studied. The reflectance difference in this image, based on the shift of the reflectance curves, is 0.5 %. This is

about the limit for practical SPM imaging, since the contrast should be sufficient to focus using the real-time image.

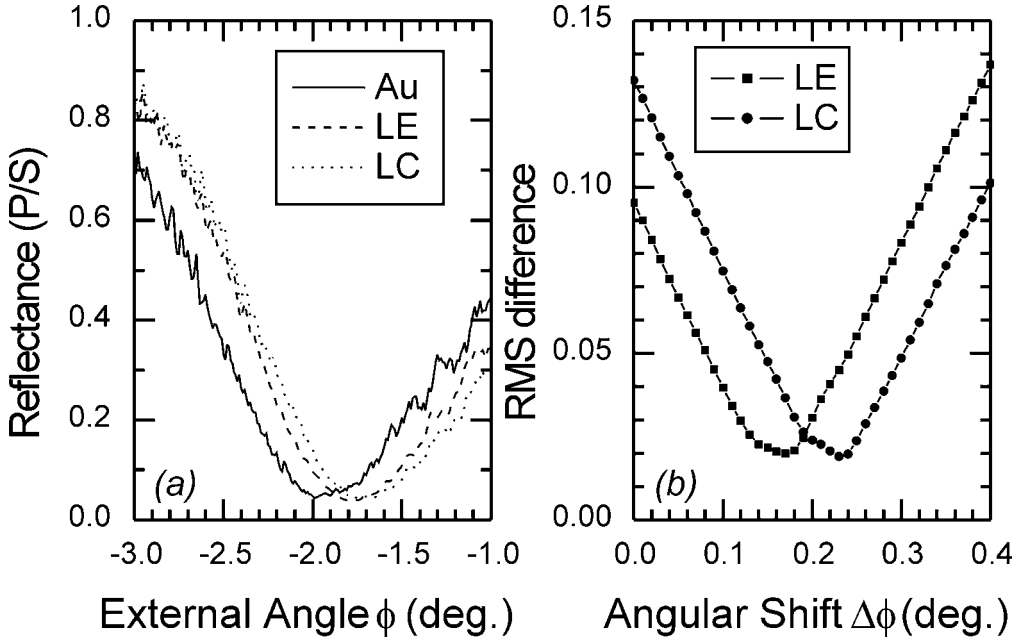

Fig. 5.13 ***(a)*** Microscopic reflectance scans for the DMPE layer, for a bare, LE, and LC region in an image. ***(b)*** The root-mean-square value of the difference of the LE and LC curves with the curve of the uncovered part when they are shifted towards this curve along the ϕ-axis.

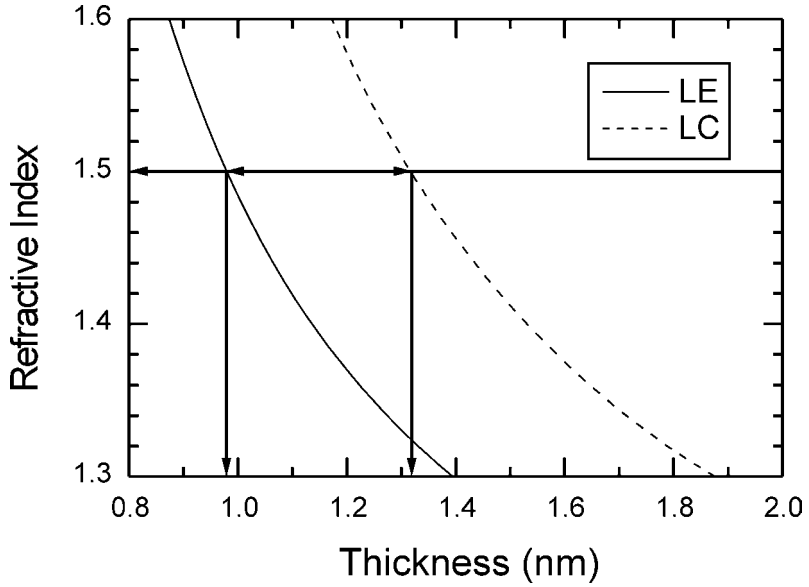

Fig. 5.14 Possible refractive index and thickness combinations as determined from the angular shifts for the LE and LC domains. The thickness difference of both domains is indicated for a refractive index of 1.5.

5.5 References

(1) Gorter, E.; Grendel, F. *J. exp. Med.* **1925**, *41*, 439.
(2) Singer, S. J. In *Membrane Structure and Function*; Rothfield, L. I., Ed.; Academic Press: New York, 1971.
(3) Singer, S. J.; Nicolson, G. L. *Science* **1972**, *175*, 720.
(4) Booij, H. L.; Daems, W. T., Eds., *Biomembranen 50 jaar na Gorter en Grendel;* Centrum voor landbouwpublicaties en landbouw documentatie: Wageningen, 1976.
(5) Benga, G., Ed., *Structure and properties of cell membranes, volume III;* CRC Press: Boca Raton, 1985.
(6) Earnshaw, J. C.; Winch, P. J., *Transitions in model membranes,* SPIE **1403,** 316-325 (1990).
(7) Birdi, K. S. *Lipid and biopolymer monolayers at liquid interfaces;* Plenum Press: New York, 1989.
(8) Vogel, V.; Möbius, D. *Thin Solid Films* **1985**, *132***,** 205.
(9) Menger, F. M.; Wood, M. G.; Richardson, S. D.; Zhou, Q. Z.; Elrington, A. R.; Sherrod, M. J. *J. Am. Chem. Soc.* **1988**, *110*, 6797.
(10) Helm, C. A.; Möhwald, H.; Kjær, K.; Als-Nielsen, J. *Europhys. Lett.* **1987**, *4*, 697.
(11) Heckl, W. M.; Lösche, M.; Scheer, H.; Möhwald, H. *Biochim. Biophys. Acta* **1985**, *810*, 73.
(12) *Langmuir-Blodgett Films;* Roberts, G. G., Ed.; Plenum Press: New York, 1990.
(13) McConnell, H. M.; Moy, V. T. *J. Phys. Chem.* **1988**, *92*, 4520.
(14) Möhwald, H. *Thin Solid Films* **1987**, *159*, 1.
(15) Lösche, M.; Rabe, J.; Fischer, A.; Rucha, B. U.; Knoll, W.; Möhwald, H. *Thin Solid Films* **1984**, *117*, 269.
(16) Vogel, V.; Möbius, D. *Thin Solid Films* **1985**, *132*, 205.
(17) Gaub, H. E.; Moy, V. T.; McConnell, H. M. *J. Phys. Chem.* **1986**, *90*, 1721.
(18) Keller, D. J.; Korb, J. P.; McConnell, H. M. *J. Phys. Chem.* **1987**, *91*, 6417.
(19) Flörsheimer, M.; Möhwald, H. *Thin Solid Films* **1988**, *159*, 115.
(20) Moy, V. T.; Keller, D. J.; Gaub, H. E.; McConnell, H. M. *J. Phys. Chem.* **1986**, *90*, 3198.
(21) McConnell, H. M.; Keller, D. J. *Proc. Natl. Acad. Sci. USA* **1987**, *84*, 4706.
(22) McConnell, H. M.; Keller, D. J.; Gaub, H. E. *J. Phys. Chem.* **1986**, *90*, 1717.
(23) Lösche, M.; Helm, C.; Mattes, H. D.; Möhwald, H. *Thin Solid Films* **1985**, *133*, 51.
(24) Heckl, W. M.; Miller, A.; Möhwald, H. *Thin Solid Films* **1987**, *159*, 125.
(25) Kooyman, R. P. H.; Krull, U. J. *Langmuir* **1991**, *7*, 1506.
(26) Lösche, M.; Rabe, J.; Fischer, A.; Rucha, B. U.; Knoll, W.; Möhwald, H. *Thin Solid Films* **1984**, 117, 269.
(27) Hickel, W.; Knoll, W. *J. Appl. Phys.* **1990**, 67**,** 3572.

CHAPTER SIX

ADHESION AFM APPLIED TO LIPID LB MONOLAYERS

Recently developed adhesion atomic force microscopy was used as a technique to map the spatial arrangement of chemical functional groups at a surface with a lateral resolution of 20 nm. The ratio of the adhesion forces for different functional groups can be compared with the values determined from the known surface energies. This concept was demonstrated by mapping the adhesive interaction of domains in a phase-separated lipid monolayer with the AFM tip. The ratio of the adhesion forces for both phases corresponds with the theoretical number for the CH_2 and CH_3 groups.

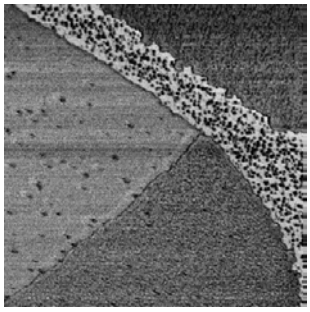

6.1 Introduction

The spatial arrangement of functional groups and their interactions are important in fields as diverse as biophysics: recognition in biological systems or immunosensors; engineering: lubrication in mechanical devices; molecular electronics: adhesion between polymers and metals; and chemistry: chemical modifications of polymer surfaces. For an improved understanding of these problems it is important to be able to study the arrangement of chemical functional groups and their interactions at the molecular level.

Direct measurements of forces between molecular assemblies have been performed with the surface forces apparatus (SFA)[1-4] between crossed cylinders (radius of curvature: $R \sim 1$ cm). For molecular force measurements on a laterally smaller scale atomic force microscopic (AFM)[5] methods have been used. To obtain a well-defined probe geometry, spherical probes have been attached to AFM cantilevers ($R \sim$ 10-100 μm). In these experiments forces between single complementary strands of DNA[6] and discrete intermolecular interactions of ligand-receptor pairs[7] have been studied. The adhesion forces between individual ligand-receptor pairs have also been measured with chemically modified AFM tips ($R \sim 100$ nm).[8]

It has been pointed out before that it should be possible to use the AFM to characterize the surface chemical composition as well as the topography.[9,10] Burnham *et al.*[9] found that the adhesive forces between tip and sample increased systematically with surface energy. To image material properties as well as topography on thin films adhesive interactions,[10-12] elastic properties,[13,14] and friction forces[13,15-18] have been mapped. Using the friction force, a discrimination between hydrophilic and hydrophobic groups that were covalently bound to sample and probe has been achieved with a lateral resolution of 200 nm.[16]

Instead of hypothesizing the relation between adhesion and friction at the molecular scale (for a study see Ref. 2), we chose to measure the adhesion force directly with a modified AFM.[19] The ratio of the adhesion forces for different functional groups can be predicted quantitatively from their surface energies and can be compared with the experimental value. Additional advantages of this approach are that the sample is not likely to be disturbed because the probe is not scanned laterally while in contact and even very small differences in surface energy are resolved. We will demonstrate this by imaging a phase-separated lipid monolayer nondestructively.

In conventional contact-mode AFM operation, the deflection of a cantilever-probe combination is measured while scanning in contact with the sample. Therefore, the topography is imaged, while the chemical nature of the functional groups at the surface remains unknown. In adhesion AFM,[12,19-21] a different approach is used. Force versus cantilever-displacement curves,[19,22] show the cantilever deflection as the tip-cantilever combination approaches the sample, makes contact, and is retracted again (Figure 6.1). The hysteresis in this curve is a measure for the adhesive probe-sample interaction and is related to the chemical nature of the functional groups at the sample and probe surface. With our setup (a modified stand-alone AFM[23]) we can measure and analyze up to 550 force-distance curves per second, which allows direct adhesion force imaging. Other methods to measure surface forces include force curves with force feedback[24] and the resonance method.[10,25]

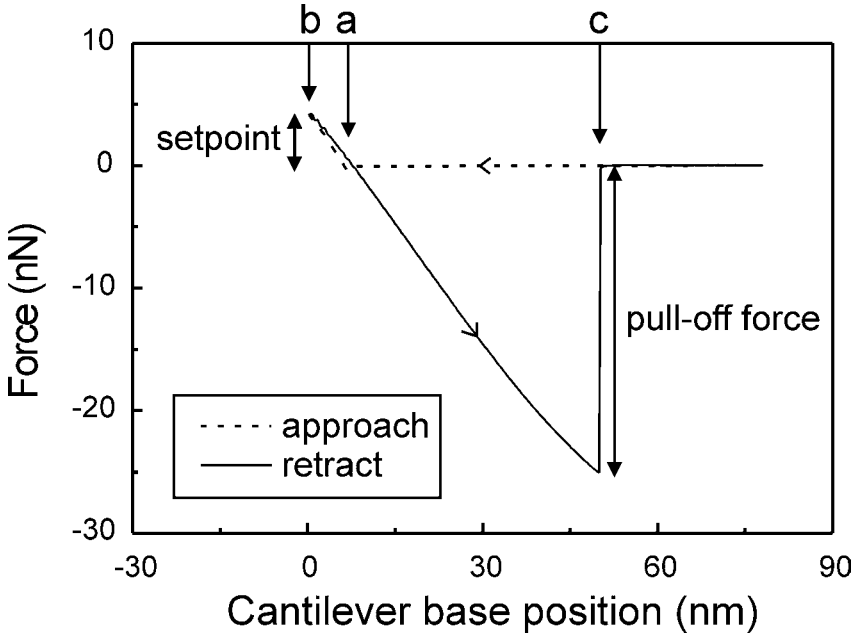

Fig. 6.1 A typical force-distance curve measured with the adhesion AFM setup.[19] The Si_3N_4 tip is moved in and out of contact by ramping a small piezo actuator. Moving the tip down, the cantilever will deflect after touching the sample (a) until a certain preset deflection is reached (b). The piezo movement up to this setpoint is a measure of the thickness of the sample because on the thicker parts of the sample this point will be reached earlier than on the thinner parts. After the setpoint has been reached, the tip is retracted to the upper limit determined by the ramping voltage. The hysteresis in the force curve results in the well-known adhesion dip. The pull-off force can be obtained when during the retrace the tip leaves the sample at some point (c). This determination is realized in hardware, allowing up to 550 force curves to be measured per second.

To demonstrate the concept, a dimyristoylphosphatidylethanolamine (DMPE) film was made by the Langmuir-Blodgett (LB) technique, at a surface pressure for which the film is in a liquid-expanded (LE) to liquid-condensed (LC) phase-transition.[26] It has been demonstrated numerous times that such a film, whether at the water-air interface or deposited on a solid substrate exhibits a domain structure corresponding to the coexisting LE and LC phases.[26] The DMPE molecule consists of a hydrophilic part that adheres to a hydrophilic substrate and two hydrophobic hydrocarbon chains. In the solid LC domains the layer is crystalline[27] and the probe tip will only interact with the hydrophobic CH_3 endgroup. In the amorphous LE phase, the molecules are less densely packed and thus a hydrophilic Si_3N_4 tip will have a stronger interaction with the 12 slightly less hydrophobic CH_2 groups along the hydrocarbon chain. Therefore, we expect the adhesion contrast to be caused by the CH_2 and CH_3 groups for the LE and LC phases, respectively. However, we want to stress that it should be possible to apply the same concept to other problems.

The adhesion force is connected with interfacial energy, which is a concept that can be applied to macroscopic as well as microscopic systems.[1] Macroscopically, the interfacial energy can be determined by contact angle measurements. For microscopic systems, and even for very small numbers of molecules, its numerical value is close to that of a planar macroscopic surface composed of the same molecules.[28]

To compare *absolute* adhesion forces with theory a very well-defined probe geometry is needed. This can be obtained by the attachment of spherical probes to an AFM cantilever. However, because of their size these probes are not suitable for high-resolution imaging, and therefore we chose a different approach. The relative humidity and the geometry of a normal AFM tip remain the same for the different areas within one image and within the measuring time (typically 10 min). Therefore, we focus on the *ratio* of the adhesion forces for the respective domains, a number that can easily be derived from basic thermodynamics.[1]

Our central result is that a simple thermodynamic model can be used to predict the ratio of the adhesion forces for different functional groups. The adhesion force can be written as

$$F \propto RW_{132} \tag{6.1}$$

where R is the radius of curvature of the end of the Si_3N_4 tip and W_{132} is the energy change on separating unit area of two media 1 and 2 in medium 3.

$$W_{132} = \gamma_{13} + \gamma_{23} - \gamma_{12} \tag{6.2}$$

where γ_{ab} is the interfacial energy of media *a* and *b*. In our case we have medium 1, DMPE (sample); medium 2, Si_3N_4 (tip); medium 3, air. Therefore, we can estimate $\gamma_{13} = \gamma_1$; $\gamma_{23} = \gamma_2$; and $\gamma_{12} = \gamma_1 + \gamma_2 - 2\sqrt{\gamma_1\gamma_2}$ using the combining relations.[1] Thus,

$$F \propto R\sqrt{\gamma_1\gamma_2} \tag{6.3}$$

as has been found previously.[3,9] Note that for the Johnson, Kendall, and Roberts (JKR)[29] theory as well as for the Derjaguin, Muller, and Toporov (DMT)[30] theory the adhesion force increases linearly with *R* and the interfacial energy, with proportionality constants of 3π and 4π, respectively.

6.2 Experimental section

DMPE Langmuir-Blodgett monolayers were prepared on different substrates to enable the use of adhesion AFM as well as optical surface plasmon microscopy.[31] Substrates for surface plasmon microscopy were made by evaporation of 45 nm gold (1 nm/s at 10^{-6} mbar) on top of a microscope cover slip. After the evaporation, 3 nm SiO_2 was sputtered on top of the gold (0.1 nm/s at 10^{-2} mbar of Ar) to make the substrate hydrophilic. Atomically smooth mica substrates were freshly cleaved and used for adhesion AFM measurements.

LB films were obtained by spreading a 1 mg/mL solution of the lipid DMPE (obtained from Sigma, used without further purification) in 3:1 (v/v) chloroform/methanol onto the subphase (water from Millipore system, resistivity > 18.2 MΩ/cm, pH adjusted to 7.5). The monolayer was transferred to the substrate at a surface pressure of 12 mN/m and a molecular area of 0.50 nm^2. Compression speed, 0.01 nm^2/min per molecule; dipping speed, 3 mm/min; transfer ratio ~1. A commercial LB trough was used (KSV 5000; KSV Instruments Ltd., Helsinki, Finland) in a laminar flow cabinet.

Both the surface plasmon microscope[32] and AFM[19,23] are home-built and were described earlier. The topography and the peak value of the adhesion dip as well as its width and area are determined on-line from the force-distance curves by electronic hardware. A ramp generator coupled to the piezo actuator moving the tip up and down is triggered by a pixel clock. When a certain preset deflection is reached, the piezo voltage is stored in a sample/hold circuit (the topography signal) and the ramping voltage is reversed. A peak detector is used to measure the peak

of the adhesion dip (the pull-off force) during the retrace. This procedure is repeated for every pixel in the image.

The cantilevers have a pyramidal Si_3N_4 tip attached to a V-shaped beam with a force constant of 0.58 N/m. The tips were ozone cleaned before use. For experiments with a controlled relative humidity the AFM setup with the sample was put in a plexiglass chamber purged with nitrogen gas of known humidity. By mixing streams of wet (obtained by bubbling the gas through distilled water) and dry nitrogen gas at an appropriate flow ratio the desired relative humidity was obtained and measured by a digital hygrometer.

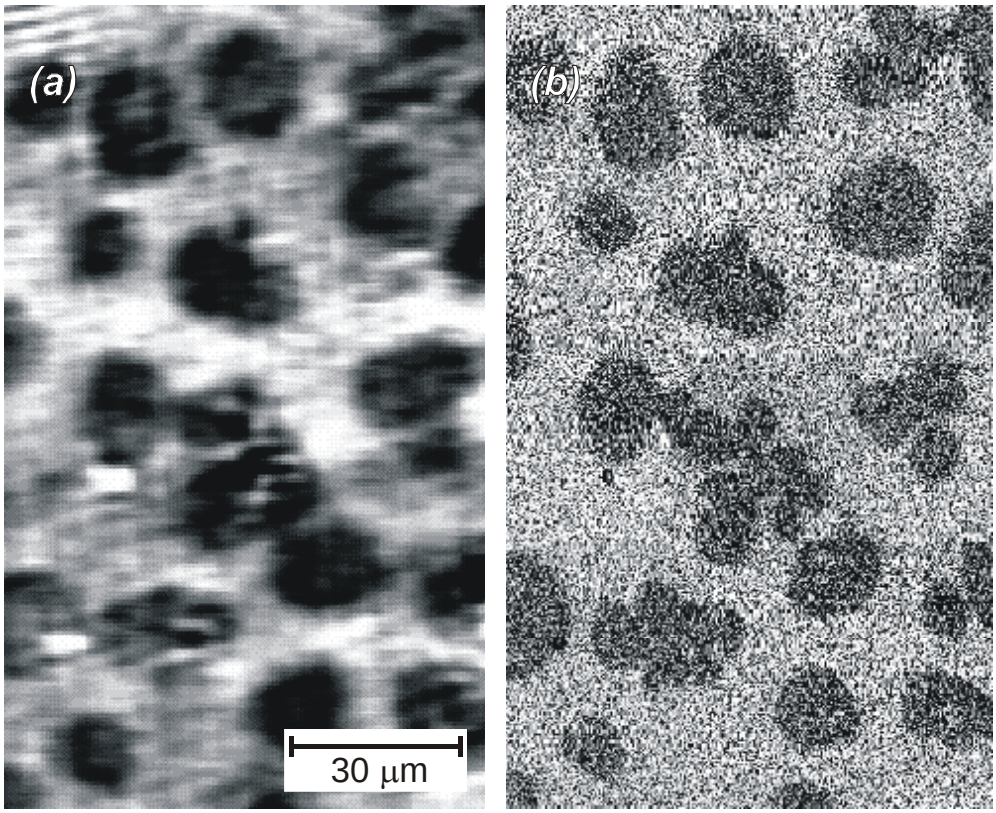

Fig. 6.2 ***(a)*** Surface plasmon microscopy image, and ***(b)*** adhesion AFM image of the same DMPE domains. The surface plasmon microscope used was described earlier.[32] In the optical image, dark regions correspond to thicker (LC) domains, in the adhesion AFM image these regions have lower adhesion forces. Quantitative surface plasmon microscopy measurements of the layer thickness were performed by defining a number of small areas in the microscopic image for which the reflectance is measured automatically as a function of the angle of incidence.[32] By determining the shift of the surface plasmon resonance minima the layer thicknesses for the different areas were determined using Fresnel theory.

6.3 Results and discussion

Apart from providing an illustration of the method used, Figure 6.1 displays a typical result for a force curve on a DMPE monolayer. From the figure we can conclude that any possible deformation of the sample is reversible because little hysteresis is observed in the loading part of the curve. A finite elastic deformation, however, has no effect on the adhesion force according to JKR theory.[29] The reproducibility that was observed (data not shown) also points to the non-destructiveness of the method. This is in accordance with earlier experimental work that has shown that both the crystalline and amorphous states of DMPE form hard, fairly rigid structures.[3]

Before and after adhesion imaging, a phase-separated DMPE monolayer was imaged with optical surface plasmon microscopy.[31,32] In the optical image in Figure 6.2*(a)*, the familiar pattern[33] for a phase-separated monolayer is observed, where the dark patches correspond to the LC regions. The contrast corresponds to a difference in optical thickness of ~0.4 nm, determined from a difference in surface plasmon resonance angle of 0.06°. This value is not uncommon for these systems,[34] with the crystalline domains thicker than the amorphous domains. Comparing Figure 6.2*(b)*, the adhesion AFM result of the same region, with Figure 6.2*(a)* we observe a one-to-one correspondence between both images. This is compelling evidence that adhesion AFM detects a contrast between the LE and LC phases.[35]

The measured adhesion forces were typically 20-30 nN (roughly an order of magnitude smaller than for the bare SiO_2 substrate), and the measured adhesion force ratio $F_{LC}/F_{LE} \sim 0.8 \pm 0.1$ (averaged over a large number of points in both regions). With $\gamma_{LC} \approx \gamma_{CH3} = 23$ mJ/m^2 and $\gamma_{LE} \approx \gamma_{CH2} = 31$ mJ/m^2,[36] we find

$$\frac{F_{LC}}{F_{LE}} = \frac{R\sqrt{\gamma_{LC}\gamma_2}}{R\sqrt{\gamma_{LE}\gamma_2}} = \sqrt{\frac{\gamma_{LC}}{\gamma_{LE}}} = 0.86 \qquad (6.4)$$

on theoretical grounds. The correspondence between these two numbers points to the difference in hydrophobicity as the contrast mechanism in adhesion AFM.

Having demonstrated that adhesion contrast can be obtained for the different phases in the domains, we used molecularly smooth mica substrates for further adhesion AFM investigations with a higher resolution on better defined samples. First, the adhesion of a clean mica substrate was measured as a function of the relative humidity (Figure 6.3). The image at constant relative humidity was essentially featureless,

while the absolute adhesion forces were always higher (80-160 nN) than those measured on monolayer-covered substrates, indicating the formation of a water film.[37]

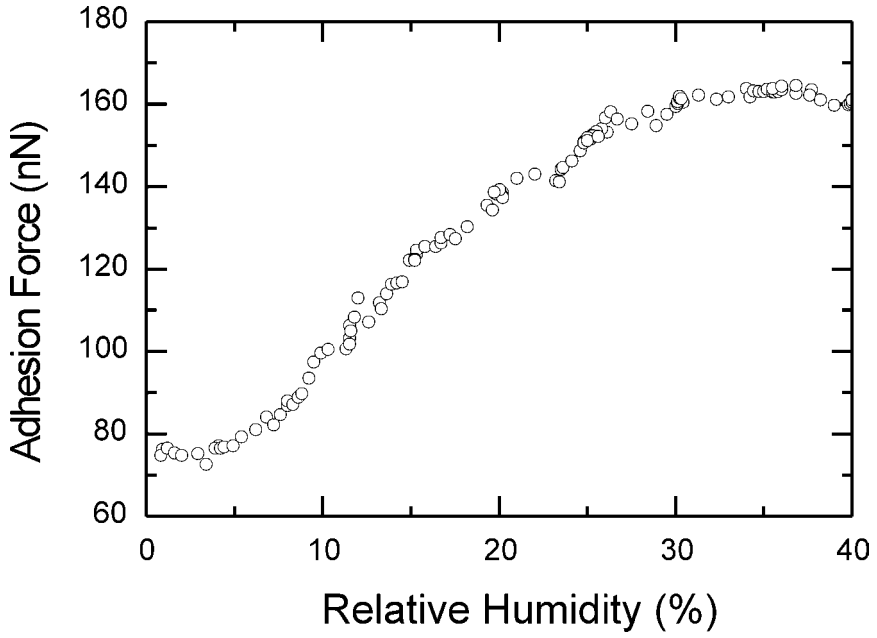

Fig. 6.3 Adhesion force on mica as a function of the relative humidity. Each point in this curve represents the average of 250 pull-off force measurements. The increase of the adhesion as a function of the relative humidity indicates the formation of a water layer on the mica with increasing thickness,[37] causing increasing capillary forces.

The consistently much lower adhesion forces for monolayer-covered substrates as compared to the bare substrate confirm the absence of a liquid layer on top of the monolayer. This is expected for such hydrophobic surfaces and has indeed been found previously.[4,38] Moreover, the presence of large (>50 nm) pinholes can safely be excluded (see Figure 6.4). However, some variations of the adhesion forces on DMPE with the relative humidity were seen. These can be explained by the presence of water on the hydrophilic AFM tip increasing the effective radius of the tip. It is important to note that this only affects the absolute adhesion forces and not the values of the ratios.

For different mica substrates, monolayers, AFM tips, and relative humidity the average value for F_{LC}/F_{LE} was 0.84 with a variance of 0.06. This number is remarkably constant and close to the expected theoretical value of 0.86. These results suggest that the model correctly predicts the ratio of the adhesion forces for the different functional groups. Therefore, the image contrast can be interpreted as the contrast in interfacial energy associated with the imaged functional groups. A further support of this

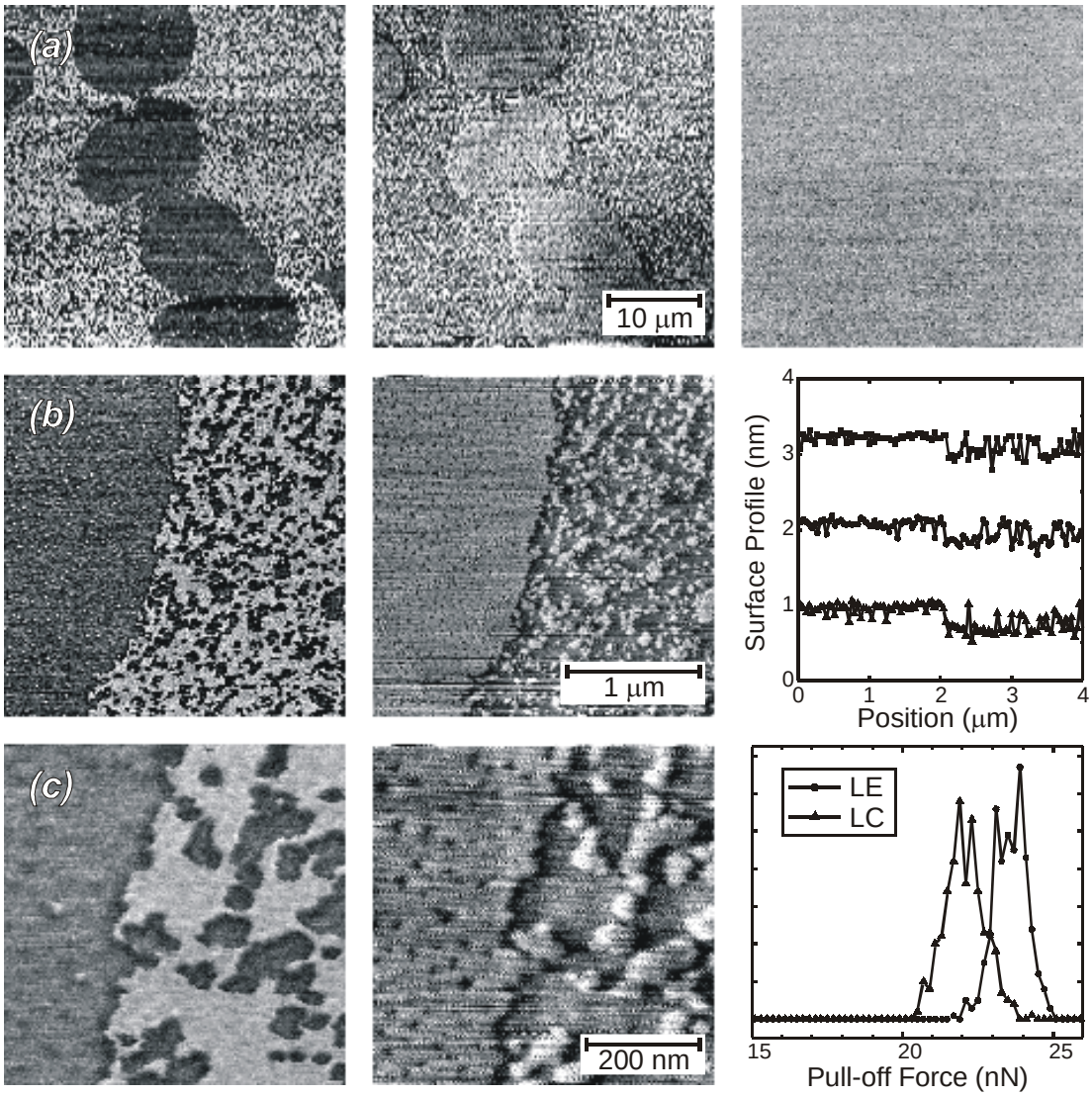

Fig. 6.4 Adhesion AFM images showing domains in the DMPE monolayer on mica. The central part was magnified for the three successive images (a-c). The left images show the adhesion, where dark areas correspond with low adhesion (LC phase). The images in the middle show the height differences, as derived from the force curves (high-pass filtered; the adhesion images were not filtered). On the right we see ***(a)*** the adhesion image for the bare mica, ***(b)*** the thickness profiles (three lines taken from an unfiltered image and shifted for clarity), and ***(c)*** the histograms for 400 adhesion measurements in the LC and LE phase. Note that for every point in these images a separate force curve was measured and analyzed (150×150 curves per image). For the topography image this means that the tip did not make a continuous profiling movement along the surface but that 0.6 nm variations in an approach of about 500 nm were measured.

view is illustrated in Figure 6.4*(c)*, where a histogram of the measured forces for both phases is displayed. The average values for the two phases are convincingly different. Besides, we note that generally the width of such a distribution might contain valuable information on heterogeneities hitherto unnoticed.

A high lateral resolution of 20 nm (estimated from the resolution of step edges in Figure 6.4) was obtained with the monolayers on the molecularly smooth mica substrates. Simultaneously measured topography images indicated a thickness difference between the domains of 0.6 nm (Figure 6.4). The difference between the surface plasmon microscopy and AFM values can be explained by the presence of pores in the solid domains and grains in the fluid domains, which appear to have the same properties as the fluid and solid domains, respectively, and are not resolved in the optical images. This phenomenon has been observed with AFM on solid substrates before, in topography,[14,39] elasticity,[14] and friction measurements.[17] Although these film defects have been said to be caused by the LB deposition process or interaction with the substrate,[39] it is tempting to identify these 'nanodomains' with those that have been postulated earlier based on indirect observations by fluorescence microscopy[40] and theoretical work.[41] These nanodomains could play an important role in domain formation.

Preliminary experiments on another domain-forming lipid, DPPC, give similar results; we therefore have good confidence that the method presented here provides a general tool to image domains with different surface energies. The same method should be applicable to many other functional groups[42] with a relatively low surface energy to inhibit the formation of a water film. For functional groups with relatively high surface energies measurements should be made in a liquid medium, to exclude capillary forces.

6.4 References

(1) Israelachvili, J. N. *Intermolecular and Surface Forces*, 2nd ed.; Academic Press: London, 1992.

(2) Yoshizawa, H.; Chen, Y. L.; Israelachvili, J. N. *J. Phys. Chem.* **1993**, *97*, 4128.

(3) Chen, Y. L.; Helm, C. A.; Israelachvili, J. N. *J. Phys. Chem.* **1991**, *95*, 10736.

(4) Chen, Y. L.; Gee, M. L.; Helm, C. A.; Israelachvili, J. N.; McGuiggan, P. M. *J. Phys. Chem.* **1989**, *93*, 7057.

(5) Binnig, G.; Quate, C. F.; Gerber, Ch. *Phys. Rev. Lett.* **1986**, *56*, 930. Rugar, D.; Hansma, P. K. *Phys. Today* **1990**, *43*, 23.

(6) U Lee, G.; Chrisey, L. A.; Colton, R. J. *Science* **1994**, *266*, 771.

(7) U Lee, G.; Kidwell, D. A.; Colton, R. J. *Langmuir* **1994**, *10*, 354.

(8) Florin, E.-L.; Moy, V. T.; Gaub, H. E. *Science* **1994**, *264*, 415.

(9) Burnham, N. A.; Dominguez, D. D.; Mowery, R. L.; Colton, R. J. *Phys. Rev. Lett.* **1990**, *64*, 1931.

(10) Martin, Y.; Williams, C. C.; Wickramasinghe, H. K. *J. Appl. Phys.* **1987**, *61*, 4723. Olsson, L.; Tengvall, P.; Wigren, R.; Erlandsson, R. *Ultramicroscopy* **1992**, *42-44*, 73.

(11) Torii, A.; Sasaki, M.; Hane, K.; Okuma, S. *Sens. and Actuators, A* **1994**, *44*, 153. Torii, A.; Sasaki, M.; Hane, K.; Okuma, S. *Sens. and Actuators, A* **1994**, *40*, 71.

(12) Mizes, H. A.; Loh, K. G.; Miller, R. J. D.; Ahuja, S. K.; Grabowski, E. F. *Appl. Phys. Lett.* **1991**, *59*, 2901.

(13) Overney, R. M.; Meyer, E.; Frommer, J.; Güntherodt, H.-J.; Fujihira, M.; Takano, H.; Gotoh, Y. *Langmuir* **1994**, *10*, 1281.

(14) Chi, L. F.; Anders, M.; Fuchs, H.; Johnston, R. R.; Ringsdorf, H. *Science* **1993**, *259*, 213.

(15) Overney, R. M.; Meyer, E.; Frommer, J.; Brodbeck, D.; Lüthi, R.; Howald, L.; Güntherodt, H.-J.; Fujihira, M.; Takano, H.; Gotoh, Y. *Nature* **1992**, *359*, 133. Meyer, E.; Overney, R. M.; Lüthi, R.; Brodbeck, D.; Howald, L.; Frommer, J.; Güntherodt, H.-J.; Wolter, O.; Fujihira, M.; Takano, H.; Gotoh, Y. *Thin Solid Films* **1992**, *220*, 132.

(16) Frisbie, C. D.; Rozsnyai, L. F.; Noy, A.; Wrighton, M. S.; Lieber, C. M. *Science* **1994**, *265*, 2071.

(17) Yang, X. M.; Xiao, D.; Xiao, S. J.; Wei, Y. *Appl. Phys. A* **1994**, *59*, 139.

(18) Yang, X. M.; Xiao, D.; Xiao, S. J.; Lu, Z. H.; Wei, Y. *Phys. Lett. A* **1994**, *193*, 195.

(19) van der Werf, K. O.; Putman, C. A. J.; de Grooth, B. G.; Greve, J. *Appl. Phys. Lett.* **1994**, *65*, 1195.

(20) Baselt, D. R.; Baldeschwieler, J. D. *J. Appl. Phys.* **1994**, *76*, 33.

(21) Radmacher, M.; Cleveland, J. P.; Fritz, M.; Hansma, H. G.; Hansma, P. K. *Biophys. J.* **1994**, *66*, 2159.

(22) Weisenhorn, A. L.; Hansma, P. K.; Albrecht, T. R.; Quate, C. F. *Appl. Phys. Lett.* **1989**, *54*, 2651. Blackman, G. S.; Mate, C. M.; Philpott, M. R. *Phys. Rev. Lett.* **1990**, *65*, 2270. Burnham, N. A.; Colton, R. J. *J. Vac. Sci. Technol., A* **1989**, *7*, 2906.

(23) van der Werf, K. O.; Putman, C. A. J.; de Grooth, B. G.; Segerink, F. B.; Schipper, E. H.; van Hulst, N. F.; Greve, J. *Rev. Sci. Instrum.* **1993**, *64*, 2892.

(24) Joyce, S. A.; Houston, J. E. *Rev. Sci. Instrum.* **1991**, *62*, 710.

(25) Ducker, W. A.; Cook, R. F. *Appl. Phys. Lett.* **1990**, *56*, 2408.
(26) Möhwald, H.; Kenn, R. M.; Degenhardt, D.; Kjær, K.; Als-Nielsen, J. *Physica A* **1990**, *168*, 127. For a review see Möhwald, H. *Rep. Prog. Phys.* **1993**, *56*, 653.
(27) Birdi, K. S. *Lipid and Biopolymer Monolayers at Liquid Interfaces*; Plenum Press: New York, 1988.
(28) Sinanoğlu, O. *J. Chem. Phys.* **1981**, *75*, 463.
(29) Johnson, K. L.; Kendall, K.; Roberts, A. D. *Proc. R. Soc. London, Ser. A* **1971**, *324*, 301.
(30) Derjaguin, B. V.; Muller, V. M.; Toporov, Yu. *J. Colloid Interface Sci.* **1975**, *53*, 314.
(31) Rothenhäusler, B.; Knoll, W. *Nature* **1988**, *332*, 615.
(32) Berger, C. E. H.; Kooyman, R. P. H.; Greve, J. *Rev. Sci. Instrum.* **1994**, *65*, 2829.
(33) Flörsheimer, M.; Möhwald, H. *Thin Solid Films* **1990**, *189*, 379.
(34) Lösche, M.; Rabe, J.; Fischer, A.; Rucha, B. U.; Knoll, W.; Möhwald, H. *Thin Solid Films* **1984**, *117*, 269. Hickel, W.; Knoll, W. *J. Appl. Phys.* **1990**, *67*, 3572.
(35) Simultaneously measured topography images showed that the adhesion forces also correlated with the substrate roughness on the sub-micrometer scale, causing the modulation of the adhesion seen as a grain structure in Figure 2*(b)*; on top of small bumps of the substrate the adhesion is lower due to a reduced contact area between tip and sample, while for holes the reverse is true.[11,12,20] Due to the substrate roughness the domains were not resolved in the AFM topography signal.
(36) Zisman, W. A. *Ind. Eng. Chem.* **1963**, *55*, 19. Fowkes, F. M. *Ind. Eng. Chem.* **1964**, *56*, 40. Zisman, W. A.; Fox, J. *J. Colloid Sci.* **1952**, *7*, 428.
(37) Thundat, T.; Zheng, X-Y.; Chen, G. Y.; Sharp, S. L.; Warmack, R. J.; Schowalter, L. J. *Appl. Phys. Lett.* **1993**, *63*, 2150.
(38) Meyer, E.; Howald, L.; Overney, R. M.; Brodbeck, D.; Lüthi, R.; Haefke, H.; Frommer, J.; Güntherodt, H.-J. *Ultramicroscopy* **1992**, *42-44*, 274. Blackman, G. S.; Mate, C. M.; Philpott, M. R. *Vacuum* **1990**, *41*, 1283. Alley, R. L.; Komvopoulos, K.; Howe, R. T. *J. Appl. Phys.* **1994**, *76*, 5731.
(39) Mikrut, J. M.; Dutta, P.; Ketterson, J. B.; MacDonald, R. C. *Phys. Rev. B* **1993**, *48*, 14479. Viswanathan, R.; Schwartz, D. K.; Garnaes, J.; Zasadzinski, J. A. N. *Langmuir* **1992**, *8*, 1603.
(40) Flörsheimer, M.; Möhwald, H. *Thin Solid Films* **1988**, *159*, 115.
(41) Israelachvili, J. N. *Langmuir* **1994**, *10*, 3774.
(42) A graphic representation of the surface energy spectrum of functional groups can be found in Adamson, A. W. *Physical Chemistry of Surfaces;* Wiley: New York, 1967.

CONCLUSIONS

In Chapter 2, surface plasmon resonance was used for immuno-sensing. Using a differential technique, immune reactions at the sensor surface could be followed by monitoring the shift of the surface plasmon excitation angle in time. The accuracy in the determination of the SPR excitation angle was very high, and additional information could be obtained by simultaneously measuring the reflectance and its second derivative with respect to the angle of incidence. In this way, position, depth and width of the reflectance minimum can be measured in real-time. As surface roughness is known to increase the width, this could yield some information on the dynamics of protein monolayer adsorption. Because the measurement is fast and the modulated beam can easily be scanned over the sensor surface, this method is suitable for multichannel measurements as well, as was demonstrated.

Laterally resolved sensor measurements were also carried out in an imaging system, where the angle of incidence of a wide, collimated laser beam was kept fixed, while imaging the reflecting light onto a video camera. This has the advantage of being able to actually observe the defined sensing areas on the sensor surface during the measurement, or even defining them after the measurement. Although we defined 16 sensing areas, in fact every CCD element acts as a separate detector that is operated in parallel, giving information on the sensing area that it receives the reflected light from. Therefore, the number of sensing areas might be much larger, as long as their size exceeds the propagation length of the SPs (typically μm's). The signal to noise ratio decreases with the sensing area size, but the amount of light coupled in can be increased by several orders of magnitude.

To get an idea of the obtainable lateral resolution with SP imaging, and how to improve it, the propagation of SPs near an index step was studied in Chapter 3. A phenomenological model was developed and its results were compared to measurements for a number of wavelengths. All parameters in the model were derived from the layer structure and boundary conditions, leaving no parameters to be fitted. A good agreement between model and experimental values was found.

In Chapter 4 and 5 we have demonstrated the qualities of surface plasmon microscopy and the possibility to measure local reflectance scans. Lipid phase-separated LB monolayers were successfully prepared and

characterized. Using a number of techniques to improve the acquisition of the images, the maximum lateral resolution as determined by diffraction was nearly attained. However, Brewster angle microscopy should ultimately be able to reach a similar resolution, and has the important advantage of the capability to study the monolayer at the air-water interface.

When a much higher lateral resolution is needed, purely optical means do not suffice, and atomic force microscopy can be used. This was demonstrated in Chapter 6, where together with the topography the chemical properties of the monolayer surface were used to image it, measuring the adhesive interaction between tip and sample. With this new adhesion force atomic force microscope the contrast can be high, because the adhesion depends only on the outer atoms of the surface, and not on the thickness of the layer under study. In this case, the contrast was seen to match that expected of CH_2 and CH_3 groups (16% difference in adhesion). The lateral resolution that was obtained was about 20 nm. It is expected that this form of microscopy can be used for the imaging and recognition of many other functional groups. It is especially well suited for monolayers, since these samples can be molecularly smooth by deposition on mica substrates, ensuring a constant interaction area between tip and sample.

Since surface plasmon microscopy measures ‘through’ the monolayer, and measures the layer thickness, while AFM only measures the outer surface of the monolayer, it would be interesting to combine both techniques (see Chapter 1). This is very well possible because the SPM measurement is carried out at the ‘substrate-side’ of the sample, while the AFM measurement is done on the outside of the sample. An SPM setup with the sample in the horizontal plane was designed especially for this purpose. It will be described in the appendix, since it was only recently completed, and combined measurements have not yet been done.

APPENDIX

In this appendix we describe a new SPM setup that was designed and built just before the completion of this thesis. First the aims of the new setup will be mentioned, then we will describe how the instrument was realized in hardware and software.

A.1 Design aims

The SPM setup was designed and built with the following aims:

(i) The sample interface should be in the horizontal plane.
(ii) It should be possible to make angular scans.
(iii) The same part of the sample should be imaged during an angular scan.
(iv) It should be possible to use an AFM on the same sample simultaneously, also for measurements in water.
(v) It should be possible to use different wavelengths.

A.2 Implementation

To have the sample interface in the horizontal plane, the optics are in the plane of incidence *i.e.* the vertical plane. They are mounted on two arms that can rotate around the same axis (see Fig. A.1*(c)*). These arms are driven by a stepping motor at the back side of the setup (see Fig. A.1*(b)*). The exact angle of incidence is determined at the axis by a high precision angle encoder. A half sphere was used as a prism to keep the imaged area at a fixed position while rotating the arms. Because the SPM uses internally reflecting light, the space above the sample on the prism is free. A platform was designed to allow an AFM to be placed over the sample, and do SPM and AFM measurements simultaneously. These measurements can even be done in an aqueous environment (*e.g.* to study protein / surface interactions). For most measurements a small HeNe-laser will be used as a light source, for measurements at other wavelengths a polarization preserving fiber can be used in combination with a bigger

laser. A CCD video camera and a video digitizer were used to acquire and store SPM images.

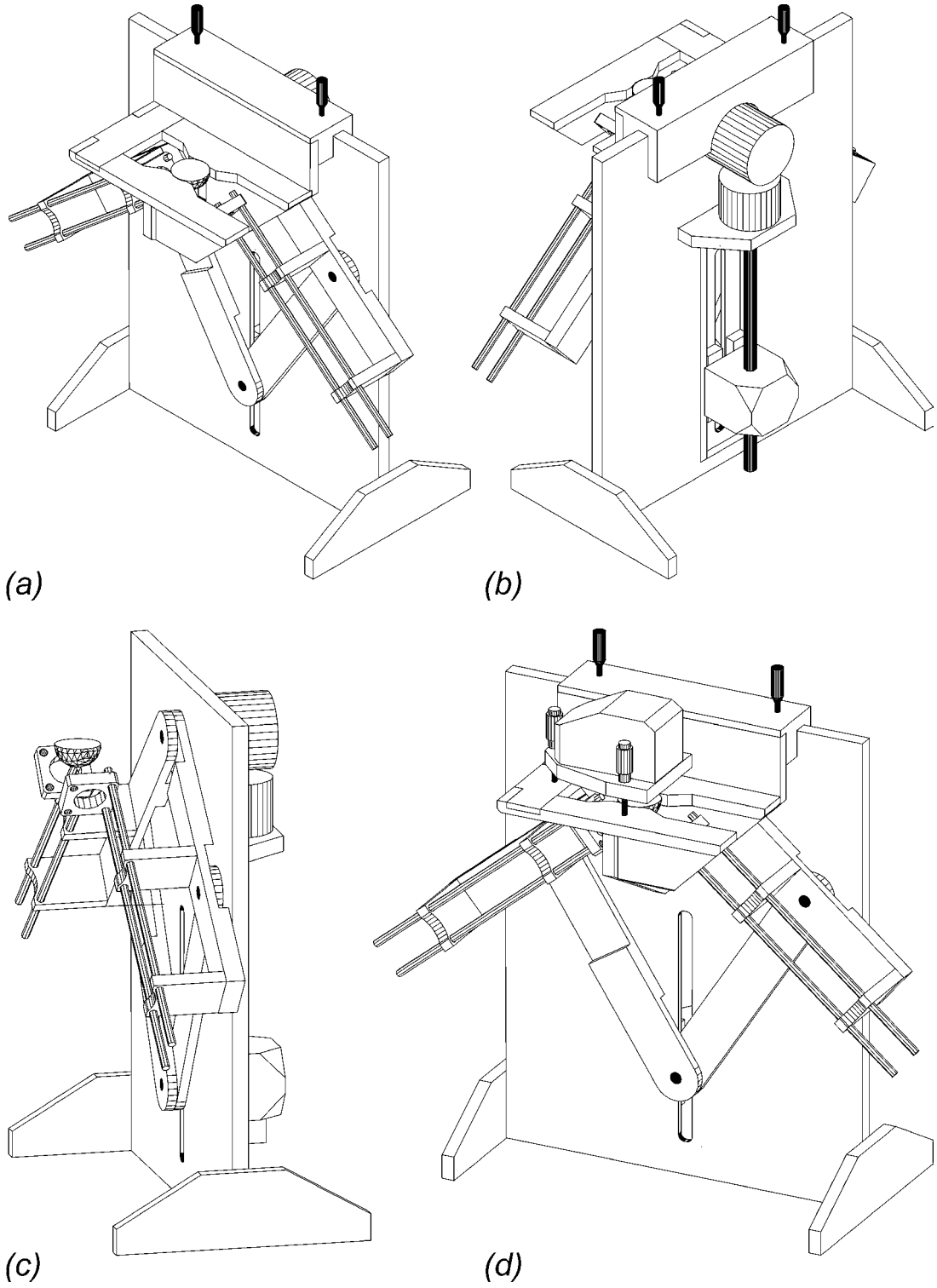

Fig. A.1 ***(a)*** front view of the setup; ***(b)*** backside view; ***(c)*** front view without the AFM platform; ***(d)*** front view with AFM over the prism.

A.2.1 Software

Software was developed such that all features of the setup can be controlled using an interactive computer program. The computer screen shows the live SPM video image with the menus and mouse cursor overlapping (see Fig. A.2). Via these menus the following functions can be performed:

(i) *video control*: images are continuously acquired but can also be frozen, saved to harddisk, *etc*.

(ii) *polarization switching*: the polarization of an external light source can be switched using a computer-controlled Pockels cell.

(iii) *angle control*: the angle of incidence is continuously measured with the angle encoder connected to the left upper arm. The stepping motor can be made to increment or decrement the angle or adjust it to a certain value.

(iv) *cursor definition*: a number of areas within the image can be defined for measuring their average intensity as a function of time or angle of incidence (*e.g.* for multisensor measurements).

(v) *scanning*: for measurements of the average intensity of the defined cursors as a function of time or angle of incidence

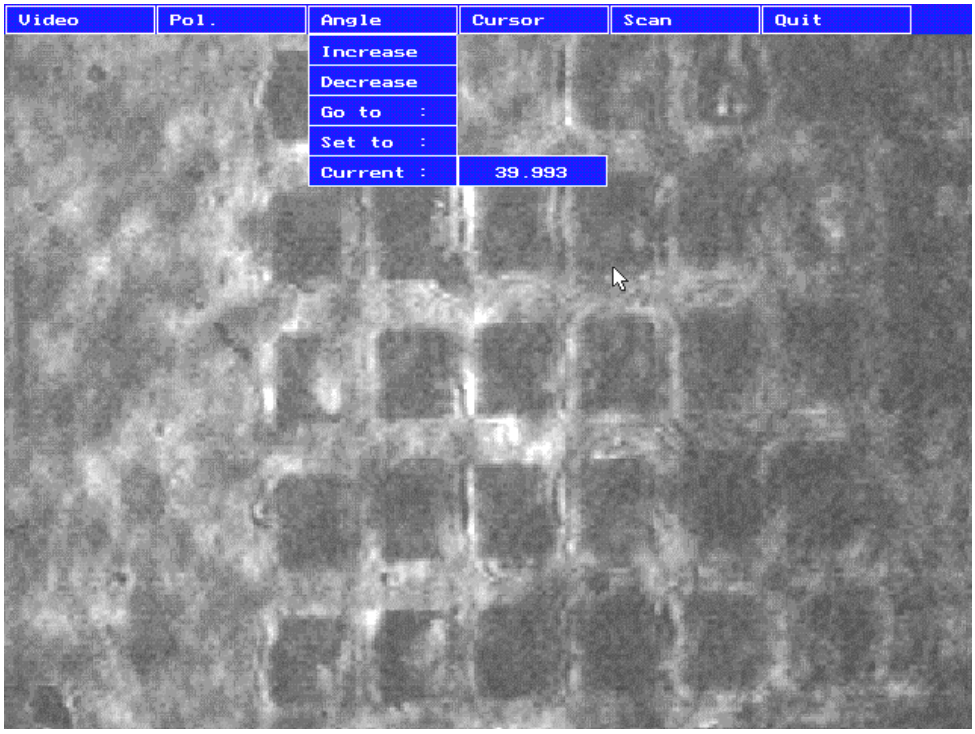

Fig. A.2 User interface for the software controlled operation of the setup.

A.2.2 Hardware

Stepping motor: RS440-458 (Mulder-Hardenberg, Haarlem).
detent torque: 30 mNm. holding torque: 500 mNm.
step angle: 1.8 deg. step angle accuracy: 5%.
rated voltage: 12 V. rated current: 0.6 A.
The parallel connection was used, and a corresponding driver was built.

ADC/DAC card: RTI 800 (Analog Devices, Norwood, MA, USA).
For conversions of analog and digital data, and digital communication.

Video digitizer: video blaster CT6000 (Creative Labs, Milpitas, CA, USA).
Digitizes the video signal in 8 bits per pixel. Uses the computer screen or any chosen part of it for displaying the live video images.

Angle encoder: ROC 417 (Heidenhain, Veenendaal).
Instead of using the commercially available read-out equipment for the encoder, the serial output signal with parity bit is read by the computer (using the ADC/DAC card for digital communication, and home-made software). The angle is encoded in 17 bits (resolution: 2.7 mdeg.) in gray code.

Spindle: diameter: M12, pitch: 1 (Jeveka, Amsterdam).

Rails with bearings: RSD3275 (Aalbers, Dedemsvaart).
This system is used to guide the part that connects the arms with the spindle.

A.3 Angular accuracy

A simple formula can be derived for the angular movement as a function of the rotation of the vertical spindle:

$$\cos\alpha = \frac{b^2 - a^2}{2ab} \qquad \text{(A.1)}$$

where b is the distance along the spindle in between the hinge points in the middle, and a is the distance between the hinge points on the arms on which the optics are mounted (see Fig. A.3 *(a)*). The lower arms are a factor $\sqrt{2}$ longer than the upper ones with length a, and thus if $b=a$ then $\alpha=90°$.

As can be seen in the calculated curve in Fig. A.3 *(b)* this construction makes it possible to rotate the arms in an almost linear way by rotating the spindle with the stepping motor. Since a movement of a hinge point of only 10 μm corresponds to a change of the angle of about 10 mdeg., the accuracy of the hinges should be very high.

Experimentally, the measured angle was always found to be within 10 mdeg. of the calculated angle. Since the angle of incidence is measured directly at the incoupling (upper left) arm with an accuracy of 3 mdeg., this does not limit the accuracy of the determined angle.

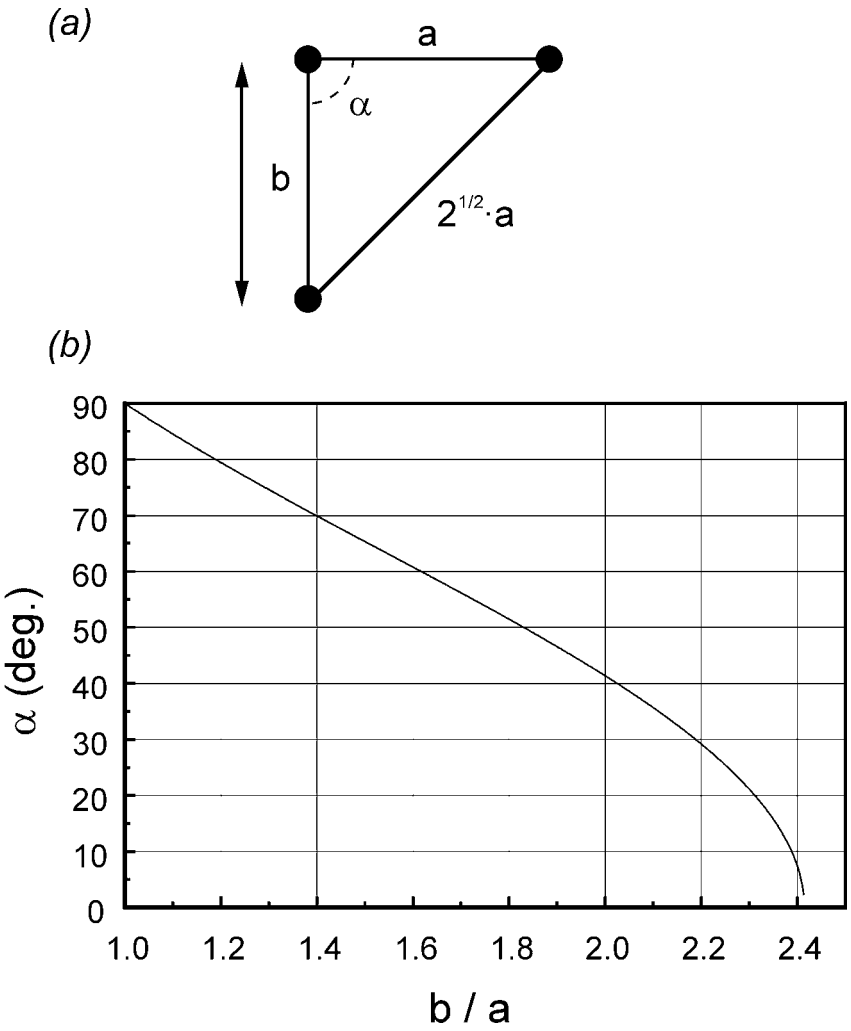

Fig. A.3 Calculation of the rotation of the arms as function of the shift of the lower hinge point. ***(a)*** schematic of the arms; ***(b)*** calculation results, differing less than 10 mdeg. from the experimental results.

SUMMARY

Surface plasmon resonance (SPR) is the phenomenon of resonantly excited collective electron oscillations at a metal surface. This can be achieved by using the evanescent field of light reflecting in a prism to excite SPR in a thin metal layer on top of that prism. If resonance conditions are fulfilled a minimum of light is reflected. The conditions for the reflecting light for which resonance occurs depend very much on the presence of optical structures in the evanescent field. Therefore, SPR can be used to image lateral heterogeneities in those structures and monitor changes in time.

A general introduction into reflectometric methods for the study of surfaces and thin layers is given in the first chapter. Fresnel's theory can be used to describe these methods.

In the second chapter SPR is used to detect immune reactions at surfaces. In this case the optical structure within the evanescent field changes in time through the formation of immune complexes. Two types of SPR sensors are described. The first one uses a differential detection technique, and is demonstrated with single and multi-channel measurements. The second one operating with a fixed angle of incidence, is used to monitor a two-dimensional array of sensor surfaces.

A model describing the propagation of surface plasmons near an indexstep is described in the third chapter. Using this model one can estimate the lateral resolution obtainable with surface plasmon microscopy (SPM), where the reflecting light is imaged with a microscope objective.

The fourth chapter describes an SPM setup and a number of methods used to enhance the lateral resolution.

An introduction into the Langmuir-Blodgett (LB) method for the preparation of monolayers is given in the fifth chapter. The SPM is used to image domains in phase-separated lipid monolayers.

In the sixth chapter a different method is used for the imaging of phase-separated monolayers. Adhesion atomic force microscopy (adhesion AFM) is used to measure the adhesive interaction between the layer and the very sharp AFM tip for every point in the resulting image. This image shows the lateral distribution within the layer of chemical groups that are exposed to the tip.

SAMENVATTING

Oppervlakte plasmon resonantie (SPR) is het verschijnsel van collectieve elektron oscillaties die aan een metaaloppervlak resonant worden geëxciteerd. Dit kan worden bereikt door gebruik van het evanescente veld van licht reflecterend in een prisma, voor de excitatie van SPR in een dunne metaallaag op dat prisma. Bij resonantie reflecteert er een minimale hoeveelheid licht. De voorwaarden voor resonantie hangen sterk af van de aanwezigheid van optische structuren in het evanescente veld. Hierdoor kan SPR gebruikt worden voor het afbeelden van deze structuren en het waarnemen van veranderingen in de tijd.

Een algemene inleiding in reflectometrische methoden voor de studie van dunne lagen wordt in het eerste hoofdstuk gegeven. Voor de beschrijving van deze methoden kan Fresnel's theorie worden gebruikt.

In het tweede hoofdstuk wordt SPR gebruikt voor het detecteren van immuunreacties aan oppervlakken. De optische structuur in het evanescente veld verandert in de tijd, door de vorming van immuuncomplexen. Twee typen SPR sensors worden beschreven. De eerste maakt gebruik van een differentiële detectie techniek, en wordt gedemonstreerd met één en multi-kanaals metingen. De tweede leest een twee-dimensionale reeks sensoroppervlakken uit, met een vaste hoek van inval.

Een model dat de propagatie van surface plasmons bij een indexstap beschrijft, wordt behandeld in het derde hoofdstuk. Gebruikmakend van dit model kan de haalbare laterale resolutie worden ingeschat van oppervlakte plasmon microscopie (SPM), een techniek waarbij het reflecterende licht met een microscoopobjectief wordt afgebeeld.

In het vierde hoofdstuk wordt een SPM opstelling en een aantal methoden om de optimale resolutie te verkrijgen beschreven.

Een inleiding in de Langmuir-Blodgett (LB) methode voor de preparatie van monolagen wordt in het vijfde hoofdstuk gegeven. De SPM wordt gebruikt voor het afbeelden van domeinen in fasegescheiden lipide monolagen.

In het zesde hoofdstuk wordt een andere methode gebruikt voor het afbeelden van deze lagen. Adhesion atomic force microscopy (adhesie AFM) kan gebruikt worden om de adhesie interactie tussen de laag en de scherpe AFM tip te meten voor ieder punt in het resulterende plaatje. Dit plaatje laat de laterale verdeling in de laag zien van chemische groepen die worden blootgesteld aan de tip.

NAWOORD

Tien jaar in Twente waarvan vijf in de vakgroep TOP (voorheen Biofysiche Techniek) zijn snel voorbij gegaan. Jan en Rob hebben me de gelegenheid gegeven de laatste vier jaar zelfstandig onderzoek te verrichten, als opvolger van Helene. Daarbij heb ik regelmatig de hulp ingeroepen van o.a. technische vakmensen als Johnny Sanderink, Aufried Lenferink, Hans de Boer en John Caspers.

Ook kon ik altijd een beroep doen op collega promovendi wier opstellingen ik naspeurde op voor mij bruikbare onderdelen of ideeën. Aan de contacten met collega's tijdens borrels, sport enz. bewaar ik ook goede herinneringen. Tijdens borrels werd er gelukkig altijd goed op toegezien dat het gesprek niet over natuurkunde ging. Borrels zijn er namelijk voor bier, daardoor geïnspireerde 'filosofische' gedachten en om je beklag te doen! Hans K., Ton en vele anderen waren daarbij onmisbaar.

Voor de goede sfeer waren ook de mensen van de 'oude garde' promovendi verantwoordelijk, ik wil hier in ieder geval René, Tom en Constant noemen. Ook Yvonne, Dave, Silly en Willem mogen zeker niet onvermeld blijven, ze weten donders goed waarom.

Buiten de vakgroep waren er vooral de (ex-) huisgenoten: Andries, Kenneth, Jeroen v/d W., Jeroen K., Mark en Artemy (de 'Rus in de keuken'); vrienden waarmee ik de meest onwaarschijnlijke dingen beleefd heb.

Het zal de aandachtige lezer waarschijnlijk duidelijk zijn: ik wil alle hier impliciet of expliciet genoemde mensen heel hartelijk bedanken voor hun aandeel in de totstandkoming van dit proefschrift, maar vooral ook voor alles dat daar niets mee te maken had! Op dat vlak waren het bovenal mijn ouders die het maar niet konden laten mij op alle mogelijke manieren te steunen.

DE AUTEUR

Charles Berger werd op 7 maart 1968 geboren in Utrecht. In 1986 behaalde hij zijn VWO-diploma aan het Revius Lyceum in Doorn. Hij studeerde van 1986 tot 1992 Technische Natuurkunde aan de Universiteit Twente, waar hij bij de vakgroep Biofysische Techniek afstudeerde. Het onderwerp van zijn afstudeeropdracht werd dat van een daarop aansluitend promotieproject, en zo liep het leger voorgoed de kans mis om hem als dienstplichtig militair in te lijven. Als onderzoeker in opleiding, in dienst van de stichting Fundamenteel Onderzoek der Materie (FOM), was hij van 1992 tot 1996 bezig met het onderzoek waarvan u de resultaten in dit boekje beschreven ziet.